THESIS
2
2007

This is to certify that the
dissertation entitled

A HIGH-POWER LASER ABLATION ION SOURCE FOR
PENNING TRAP STUDIES OF RARE ISOTOPES

presented by

Deborah A. Davies

has been accepted towards fulfillment
of the requirements for the

Doctoral degree in Chemistry

Major Professor's Signature

4 May 2006

Date

MSU is an Affirmative Action/Equal Opportunity Institution

LIBRARY
Michigan State
University

PLACE IN RETURN BOX to remove this checkout from your record.
TO AVOID FINES return on or before date due.
MAY BE RECALLED with earlier due date if requested.

DATE DUE	DATE DUE	DATE DUE

2/05 p:/CIRC/DateDue.indd-p.1

A HIGH-POWER LASER ABLATION ION SOURCE FOR PENNING TRAP STUDIES OF RARE ISOTOPES

By

Deborah Ann Davies

A DISSERTATION

Submitted to
Michigan State University
in partial fulfillment of the requirements
for the degree of

DOCTOR OF PHILOSOPHY

Department of Chemistry

2006

ABSTRACT

A HIGH-POWER LASER ABLATION ION SOURCE FOR PENNING TRAP STUDIES OF RARE ISOTOPES

By

Deborah Ann Davies

A high-power laser ablation ion source has been developed, characterized and implemented as part of the Low Energy Beam and Ion Trap (LEBIT) experiment at the National Superconducting Cyclotron Laboratory. LEBIT was developed to make precision measurements of rare isotopes, including mass measurements with a Penning trap. The system relies on thermalizing nuclear reaction products in a helium-filled cell and then extracting them from the gas through ion-manipulation and differential pumping. Atomic ions and clusters are needed to calibrate various aspects of the entire system such as transport efficiency and the main magnetic field, in addition to understanding properties of the helium-filled gas cell. High-power laser ablation has proven to be a successful method for producing a wide range of ions under various conditions, including atmospheric pressure. Laser ablation studies of C, Al, Ag, Au, Cu, Fe, and Zn were carried out in two separate chambers, one under vacuum conditions and one under buffer gas conditions, with the second harmonic, 532 nm, from a Q-switched Nd:YAG laser. A series of calculations were done to model the ablation process and various ablation parameters of the system, and the ion trajectories of the ablated ions were modeled with the computer program SIMION. Many studies were carried out under vacuum using an ion-drift system and mass analysis in a residual gas analyzer (RGA). The ablation target and laser optics were moved to the gas cell and several ablation studies were performed, including measurements of the extraction time and the ion mobility for ions traveling through the gas cell.

for Andrew

ACKNOWLEDGMENTS

There are multiple people I would like to acknowledge for their contributions making this dissertation possible. First, thank you to my advisor Dave Morrissey for your guidance, support, and allowing me to work independently, while always being available to help. I am also grateful for your patience.

The NSCL has been a fantastic place to work, particularly with such an excellent staff. Thank you especially to Jack Ottarson and Renan Fontus for your design work, help getting everything assembled, and continued interest and assistance. The faculty and staff of the NSCL are inspiring, constantly pursuing excellence.

Thank you also to my second reader Paul Mantica, particularly for your encouragement and listening ear during my start in grad school. Also, thanks to my committee members Gary Blanchard and Lynmarie Posey for sharing laser wisdom, so I wouldn't have to "reinvent the wheel."

I would also like to thank my undergraduate thesis advisor, Niva Tro, for the research experience, the encouragement to attend graduate school, and the advice along the way.

Thank you to my research group and fellow students. Elaine and Chandana, I've appreciated your friendship, in addition to your willingness to listen to multiple practice talks and for your help along the way. Thanks to former group member Pat Lofy for all your help with getting started and answering my endless questions. Georg Bollen and the LEBIT group deserve a lot of thanks as well. Thanks especially to Stefan, Ryan and Pete for patiently answering my questions and helping with calculations. I would especially like to acknowledge my fellow graduate students for their friendship. Thanks Michelle for the ballet and Orchesis memories and Heather for our conversations and fun outings. Thanks also to Jeremy, Sean, Bryan, and Jon.

Thanks to my friends both here in Michigan and far away and my family for

your encouragement and support. Thanks especially to my parents for your love and always being there through everything. To my husband, Andrew, I would not have made it through without your love and endless patience and encouragement. Finally, thanks to God for giving me the strength to run this race.

Contents

List of Figures

List of Tables

Chapter 1

Introduction

The goal of the present work was to develop, characterize, and implement a laser ablation system to produce ions for calibrations and other studies in the gas cell at the beginning of the Low-Energy Beam and Ion Trap (LEBIT) system. LEBIT was designed to make precision measurements, including mass measurements and laser spectroscopic studies, of exotic nuclei produced at the National Superconducting Cyclotron Laboratory (NSCL). The NSCL produces a broad range of short-lived exotic nuclei by projectile fragmentation [1], a process that is not well matched to precision measurements in ion traps. The first component of LEBIT is a gas cell to thermalize the energetic, fast, exotic fragments, which are transported to a Penning trap, the key apparatus in LEBIT, for precision mass measurements. This introduction provides an overview of the LEBIT project, including a description of precision mass measurements and a few experimental details. A description of the background and motivation for the laser ablation project will be given, followed by a brief discussion of the laser ablation ion source. This dissertation discusses the laser ablation experiment, its results, and their significance.

1.1 Precision Mass Measurements

The mass of a nucleus $m(Z, N)$ is one of its fundamental nuclear properties, and is defined as the sum of the masses of its constituent protons and the masses of its constituent neutrons, minus their binding energies B:

$$m(Z, N) = Zm_p + Nm_n - B/c^2, \tag{1.1}$$

where m_p is the mass of the proton, m_n is the mass of the neutron, Z is the proton number, N is the neutron number, and c is the speed of light. The theories that predict the masses of nuclei far from stability generally diverge [2], which can be seen in Figure 1.1. For isotopes close to stability, the atomic masses are known within a typical accuracy of several keV out of a total of approximately 1 GeV per mass unit. For nuclei that are unstable to β decay, however, the accuracy for the known masses is typically on the order of $\delta m/m = 10^{-4}$ to 10^{-6} [3]. Penning traps provide a high-precision method of determining nuclear masses, producing mass accuracies as high as $\delta m/m = 10^{-11}$ or better [2–5]. LEBIT has implemented a Penning trap to make precision mass measurements of the radioactive isotopes produced at the NSCL with a precision on the order of 10^{-8} [6], and will be discussed further in Chapter 5. The precision mass measurements are dependent on accurately knowing the magnetic field strength, which is possible with calibration ion sources such as the laser ablation ion source discussed in the present work.

1.2 The NSCL

At the NSCL, rare isotopes are created via fragmentation reactions with primary (stable) beams in the range of oxygen to xenon, and thus, a large range of isotopes are available for study as shown in Figure 1.2. Tandem cyclotrons (the K500 and K1200) are coupled to accelerate ions created in an Electron Cyclotron Resonance (ECR)

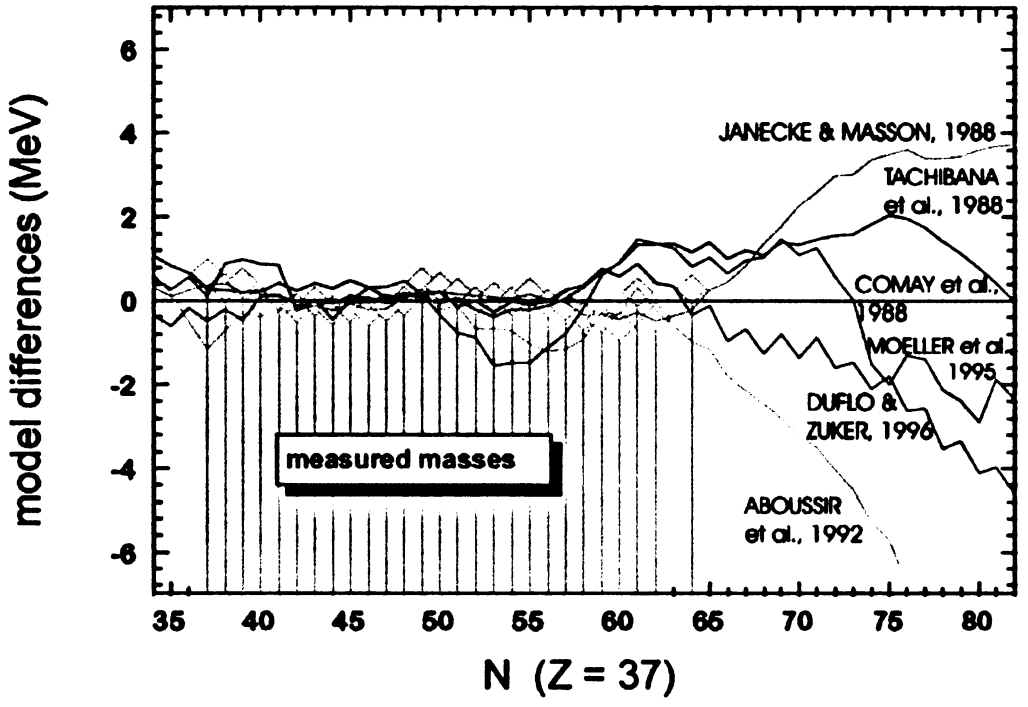

Figure 1.1: The mass divergence of rubidium isotopes, from [7].

source. The approximately 150 MeV/nucleon fully accelerated beam impinges on a thin target of material such as beryllium, creating unstable isotopes via fragmentation reactions. The A1900 fragment separator [8] then selects the desired isotopes using a magnetic rigidity/energy loss technique. The selected high-energy isotope beam is then routed to the experimental vaults at an energy of approximately 100 MeV/A. One such vault is the N4 Vault, where the gas stopping station resides. A diagram of the tandem cyclotrons and the A1900 is given in Figure 1.3. The fast ions traveling at approximately one-third the speed of light must be slowed down to thermal velocities for precision measurements.

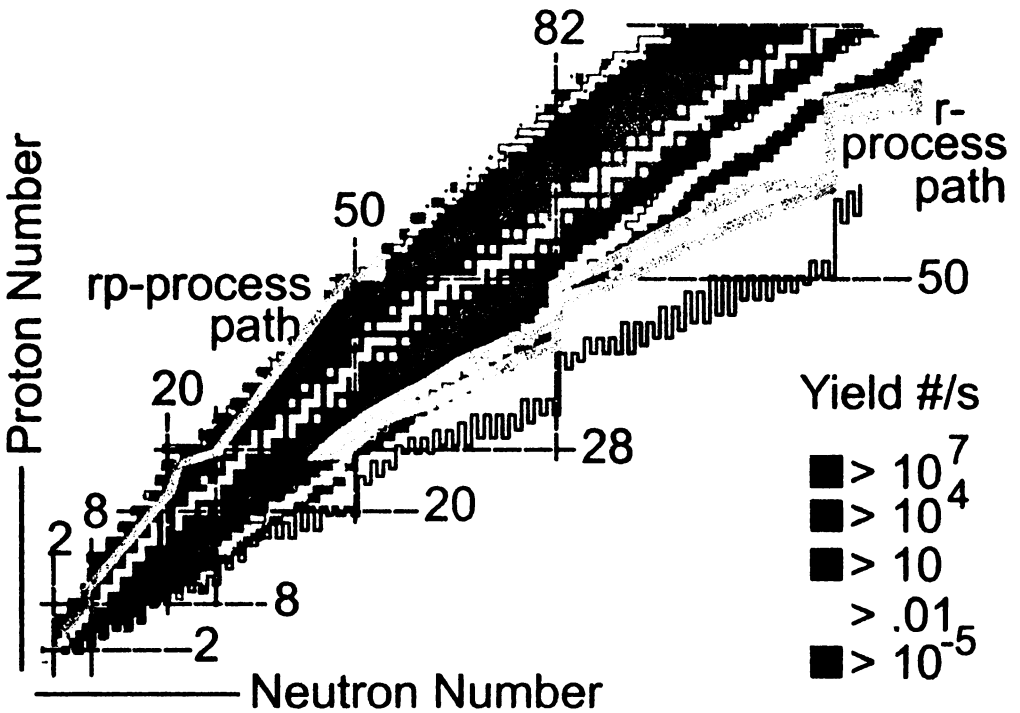

Figure 1.2: The production yield of exotic nuclei at the NSCL. The white boxes represent the stable nuclei and the paths of the astrophysical r and rp processes are shown.

1.2.1 The Gas Stopping Station and LEBIT Overview

As part of experiments with the LEBIT system, the high-energy beam is first sent to the gas stopping station [9–12]. The ions are thermalized in a buffer gas and then the buffer gas has to be stripped away. The gas stopping station includes various energy degraders prior to the entrance window of the helium-filled gas cell and an overview of the gas stopping station is shown in Figure 1.4. The ions lose the vast majority of their energy in the degraders and are thermalized in the helium gas. They begin to drift towards an exit nozzle due to an applied voltage that creates an electric field. At the nozzle, the flow of high-pressure gas propels the ion from the high pressure region into a low pressure region containing a radio-frequency quadrupole (RFQ) ion guide system. The helium is removed by large vacuum pumps while the ions are transported by the RFQ through a differentially pumped series of chambers. The ions are then re-accelerated to 5 keV and sent through a beam line in the shielding wall to a buncher

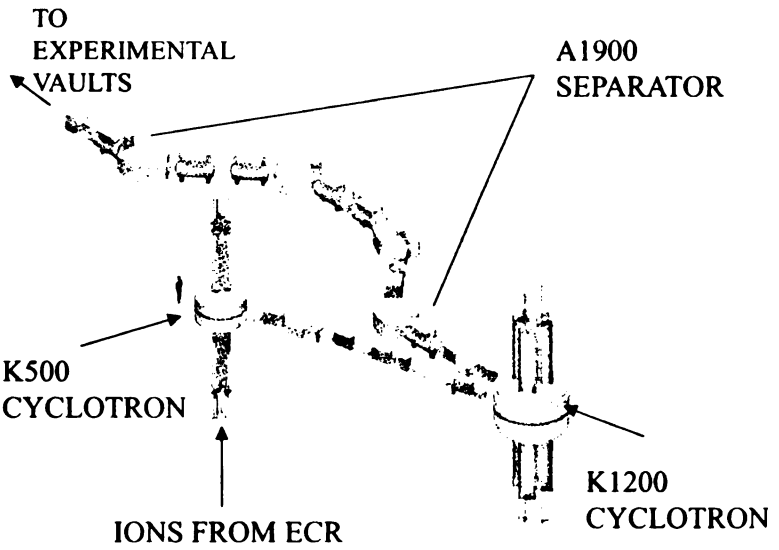

Figure 1.3: Schematic diagram of the major components along the path of the cyclotron beam from the K500 and K1200 cyclotrons through the A1900 fragment separator.

device in LEBIT. The beam can then be used in the LEBIT facility for high-precision mass measurements in the Penning trap [13, 14]. A schematic overview of LEBIT is given in Figure 1.5 including beam lines for other experiments with the thermalized beams.

1.3 The Gas Cell Laser Ablation System Overview

1.3.1 Motivation

It would be extremely useful to be able to produce a wide variety of stable ions to test the entire LEBIT system. Laser ablation can create such ions, which can then be used as test beams, for calibrations, and for studying properties of the gas cell. An additional goal is to gain further understanding of the laser ablation process in high-pressure gases. The newly developed laser ablation system described herein provides a method of producing ions at different locations in the gas cell. LEBIT uses other ion sources closer to the Penning trap, but the laser ablation system provides a source of ions with a large mass-range in the gas cell that travel along the entire

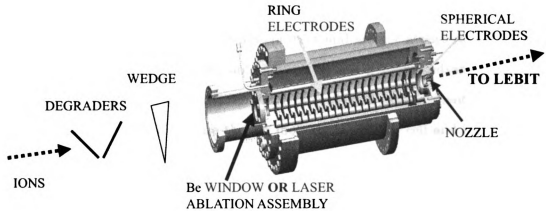

Figure 1.4: An overview of the gas stopping station. The energetic ions from the A1900 are slowed with various degraders and are then thermalized in the gas cell. The laser ablation system, the topic of the present work, can also be introduced into the gas cell.

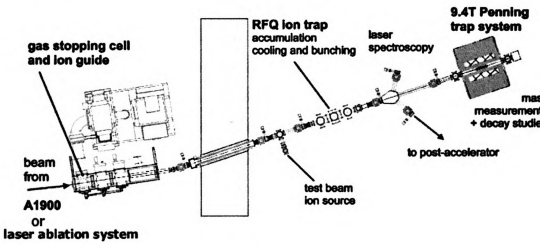

Figure 1.5: An overview of LEBIT, starting with the gas cell and ending with the Penning trap.

LEBIT line. Other sources of ions in the gas cell are a rubidium source [15, 16] and a discharge source, which are fairly straightforward sources to implement. The thermal rubidium source has the disadvantage that it is only located at one position, emits only relatively unreactive ions (unlike the energetic ions from the A1900), and the vacuum system must be opened to install the system. On the other hand, the discharge device does not require the vacuum system to be opened, but the ions obtained from this ion source are not always known, nor always reproducible since this depends on

the ionization of vacuum contaminants. Since the vacuum contaminants change over time, the ions produced are not always constant and are not always easy to identify with the Penning trap. The laser ablation system has a further advantage that the laser pulse provides a useful start-signal for time-of-flight measurements, which were used in this research to measure the ion mobility in the gas cell and ion extraction from the gas cell.

1.3.2 Laser Ablation Definition and Brief History

Laser ablation is defined as the laser-matter interaction that results in both the removal of at least one-tenth of the target material monolayer per laser pulse in the irradiated area, and modification of the target material on the mesoscopic level. The fluence (laser intensity per unit area) required for laser ablation is approximately 1 J/cm^2 [17]. First mentioned by Breech and Cross in 1962, laser ablation has an extensive history, originating at approximately the same time as the laser itself [18]. Since then, the field has transitioned from describing the damage resulting from the laser-target interaction to focusing on improving the understanding of the complex processes associated with the creation of plasma, which results from the interaction between the energetic photons and the ablated target material. A large number of applications of ablation have been developed, including pulsed-laser deposition (PLD) [19]. The field has expanded to the extent that thousands of publications exist on the subject and a review is well beyond the scope of the present work. It is interesting to note some of the widespread and multidisciplinary applications of laser ablation: nanosurgery [20], the development of optical storage devices [21], art restoration [22], laser cleaning [23], semiconductor improvement [24], and the fabrication and modification of nanomaterials [25]. One specific example demonstrates the utility of laser ablation for the fabrication of new materials: the 1996 Nobel Prize in Chemistry was awarded to Curl, Kroto and Smalley for their work involving the laser ablation of graphite in a supersonic jet of a gas mixture to synthesize a new

allotropic class of carbon– the fullerenes [26]. Laser ablation can also be used as an ion source [27–30], which is the subject of the present work.

The mechanisms and techniques of laser ablation vary greatly and span a large range of laser fluences. On the lower end of the fluence spectrum is the process of desorption, which is similar to laser ablation, but involves material removal without modifying the bulk of the target [31]. For example, Matrix-Assisted Laser Desorption and Ionization (MALDI) is a low-fluence ablation with approximate fluences of 20 mJ/cm^2 [32]. In MALDI, a fragile substance such as a protein is embedded within a solvent or matrix. The laser pulse vaporizes the sample, ideally removing only the matrix, and the protein is left ionized and intact in the gas phase. Information such as the mass or structure of the protein can then be obtained by mass analysis of the ion. An example of intermediate fluence is pulsed laser deposition (PLD), which involves the evaporation of a sample onto a thin film for applications such as semiconductor fabrication [19]. On the other hand, higher power ablation applications include the removal of debris orbiting earth using a high-power laser, with average pulsed laser powers of 100 kW [33].

1.3.3 Laser Ablation Systems at Other Facilities

Laser ablation ion sources have been implemented at two other radioactive beam facilities [5,34]. Various aspects of these facilities and the laser ablation systems differ from the one implemented in this research. The ISOLTRAP facility at CERN in Geneva, Switzerland, makes precision measurements on low-energy radioactive beams produced using the Isotope Separation Online (ISOL) method [35], in which a beam of light ions is incident on a thick target. The beam produced is a low-energy beam of approximately 60 keV [4], and since the beam is already at a low energy, no gas stopping station is needed. A laser ablation system has been utilized at ISOLTRAP, differing from the NSCL system in both its geometry and the operating conditions such as the background vacuum conditions and higher voltage acceleration electrodes [5]. The

laser ablation of C_{60} is used to provide mass references for low-energy mass measurements at ISOLTRAP [36]. Carbon is useful as a mass reference since its mass is exactly known; the atomic mass unit is defined by the mass of carbon. The ISOLTRAP laser ablation system is directly prior to a Penning trap and situated perpendicular to the beam axis. The ions are injected into the Penning trap with high energy due to the high voltage applied to the target, 2.7 kV. Other ablation targets include gold, gadolinium, and allotropes of carbon including Sigradur^{TM} (glassy carbon) [37].

A different laser ablation system has been utilized at SHIPTRAP at GSI in Darmstadt, Germany, which uses radioactive beams produced via fragmentation with beam energies on the order of 5 MeV/nucleon [38]. SHIPTRAP's laser ablation ion source is used to calibrate the TOF-MS system using the 532 nm second harmonic from a Nd:YAG laser to ablate C_{60} [34].

Similar to other laser ablation systems, the LEBIT laser ablation system was initially designed to produce atomic ions to calibrate various aspects of the entire system including transport efficiency and the main magnetic field of the Penning trap. However, the laser ablation system has to work in high pressure gas to produce the clusters and ions, unlike the other facilities. Laser ablation in a buffer gas differs greatly from ablation under vacuum conditions; this behavior will be discussed further later in this dissertation.

1.3.4 Introduction to the Laser Ablation System

As mentioned, high-power laser ablation has proven to be a successful method for producing ions that span the periodic table and is a method implemented under various conditions, including different background pressures. Laser ablation is a straightforward, "brute force" process for creating ions, yet the process is not completely understood. Therefore, in this research, the ablation process was studied under conditions including high vacuum (HV) and the presence of a helium buffer gas. The laser ablation target and some laser optics were mounted on a removable assembly on

a conflat flange so that the target and optics could be transferred between chambers. A commercial high-power Q-switched Nd:YAG laser was implemented. The 532 nm second harmonic from this laser was used for ablation studies of C, Al, Au, Ag, Cu, Fe, and Zn targets. Many tests were carried out under vacuum using an ion-drift system and mass analysis in a quadrupole mass filter. The target and laser optics were moved to the gas cell, where additional ablation studies were also performed. The normal operating condition of the gas cell involves the transport of radioactive isotopes produced at the NSCL. The ablation system provides a separate method of performing additional studies in the gas cell. The results of this research illustrate the utility, reproducibility, and validity of the system.

Objectives

The main tasks of this work can be separated into various parts. First, the laser ablation system was designed and constructed. Next, the laser ablation process was studied under vacuum conditions, the parameters affecting the process were stabilized and optimized, and the ion trajectories were simulated in the SIMION program [39]. Once the laser ablation process was understood under vacuum conditions, the laser ablation system was moved to the gas cell to create ions for LEBIT. The buffer gas in the gas cell introduced complex behavior, not present in the HV system. Finally, the data from these tests were analyzed and compared to similar work in the literature, and conclusions about the future use of the system were made.

1.4 Organization of Dissertation

This dissertation is organized as follows: Chapter 2 introduces the theory of laser ablation including mechanisms and calculations. Chapter 3 discusses some ion transport simulations done in SIMION for the laser ablation system. The HV ablation system is discussed in Chapter 4, along with experimental details, calculations and results.

In Chapter 5, the laser ablation in the gas cell is described. Finally, a summary of the results is given, followed by appendices discussing additional aspects of the ablation system.

Chapter 2

Laser Ablation Theory and Calculations

Laser ablation involves complicated, collective interactions of atoms, clusters and bulk material under extreme electromagnetic irradiation, and is therefore difficult to model. A single theory explaining all of the processes involved in laser ablation does not exist. Rather, there are numerous models that describe certain aspects of the process and change depending on the details of the system. The main areas covered in the literature are the evaporation mechanism of the target, the mechanism of light absorption by the plasma, and the expansion of the generated plasma [17, 40]. Theoretical models can approximate various properties of the system such as the temperature of the target during ablation and the laser intensity required for ablation. An overview of the models that describe the ablation process pertaining to the laser ablation system in this research, and calculations that were done to describe this system, are presented in this section.

2.1 Processes Involved in Laser Ablation

A simplified view of laser ablation under vacuum involves a laser pulse striking a target, followed by ejection of material, which can then either be detected or used for applications including thin film deposition. The processes involved in laser ablation in a buffer gas can be divided into three stages [41, 42], shown in Figure 2.1. The first stage involves the target material evaporation by the laser pulse incident on the target, followed by the second stage involving plasma formation due to the laser interaction with the evaporated material and isothermal expansion of the plasma. The first two stages are initiated with the laser pulse, and continue for the duration of the pulse. These two stages are also thought to be independent of background conditions [41]. The third stage involves the adiabatic expansion of the plasma into the background gas. The conversion of thermal energy into kinetic energy occurs during the adiabatic expansion, rapidly cooling the plasma [43]. The third stage begins after the end of the laser pulse. However, this is not quite an accurate picture of the mechanism; the processes are often concerted and interactive. For example, the buffer gas collision frequency is approximately 6×10^9 s^{-1} assuming a pressure of 760 Torr and temperature of 298 K, which results in 24 collisions during a 4 ns pulse.

Neglecting background vacuum conditions, the laser pulse first interacts with the target matrix, and particles are ejected from the surface of the matrix [31]. Various mechanisms can be used to describe the material ejection, including a thermal model involving heat conduction into the target followed by vaporization, an electronic model involving electronic excitation expelling electrons, as well as a hydrodynamic view, resulting in the ejection of droplets, and an exfoliational model, resulting in the formation of flakes of needle-shaped microstructures [44]. As mentioned, the mechanisms are neither completely distinguishable nor independent, and in addition, these mechanisms are only applicable to specific laser pulse and ablation conditions (e.g. vacuum vs. gas).

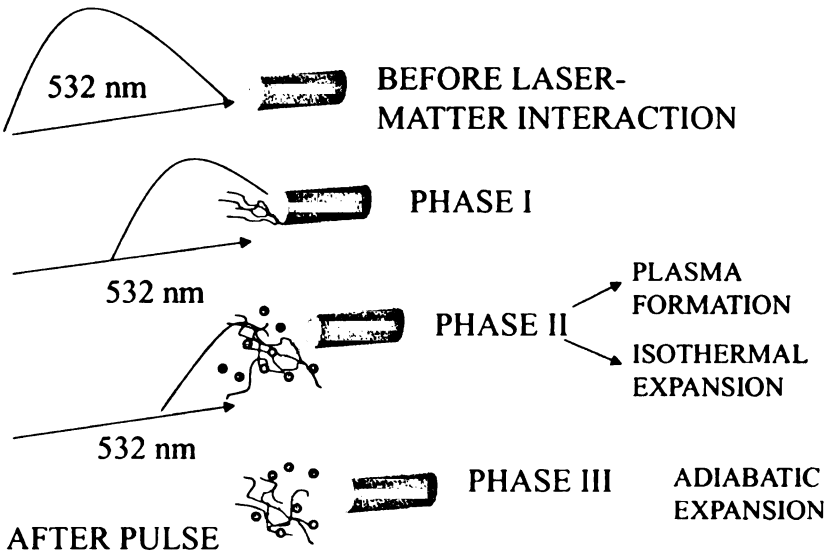

Figure 2.1: A simplified view of the mechanism of laser ablation. The first two stages occur during the 4 ns laser pulse, and are independent of the background gas conditions. The adiabatic expansion stage, the third stage, starts at the completion of the laser pulse, and interacts with the background gas, if present.

The laser pulse can interact with the ejected particles forming a plume or plasma. For example, material is ejected with velocities on the order of 10^6 cm/s and can move tens of thousands of atomic radii during the pulse. A long laser pulse such as a nanosecond pulse interacts with an isothermally expanding plasma. As mentioned, after the completion of the pulse, the plasma expands adiabatically [44,45]. The plasma or plume characteristics will change depending on various parameters including laser wavelength, background pressure, pulse width, and laser power density (J/cm^2 per pulse) [46]. Plasma shielding can also occur, preventing the light from reaching the surface and further ablation of the target.

The presence of a background gas complicates the process further causing such processes as plume deceleration, thermalization, plume-splitting, and shock-wave formation [26, 41, 43, 47, 48]. For instance, the ablated species can become thermalized due to collisions with ambient gas molecules. The interactive processes create a multi-dimensional problem. The following sections will provide an overview of some of these models, particularly applicable to the laser ablation system in this experiment. This

chapter is divided into three main sections describing the evaporation mechanism, the photon absorption mechanism of the plasma, and the properties of the expanding plasma.

2.2 Evaporation Mechanism

The mechanism of target evaporation depends on the properties of both the target and the laser pulse. The laser fluence and pulse length are very influential on the evaporation. The laser fluence can be divided into low (below $\sim$ 0.8 J/cm^2), intermediate (approximately 0.8-20 J/cm^2), and high fluence (greater than approximately 20 J/cm^2) regimes. The evaporation mechanism in the low fluence regime can be described by the ejection of non-thermal particles [49]. At the other extreme, for high fluences, the critical temperature of the target is reached and explosive phase changes occur [50]. In this study, the fluences ranged from approximately 1 to 18 J/cm^2 and an applicable evaporation mechanism is the thermal conduction mechanism, which involves thermal conduction into the solid, followed by thermal evaporation [51].

The laser pulse length also contributes to the mechanism of evaporation. A comparison of the craters created during laser ablation for three pulse length scales is shown in Figure 2.2 [31]. There is more interaction between the laser and the matter as the pulse length increases, as expected. For femtosecond pulse lengths, a two-temperature model is used to describe ablation. In this case, the pulse is short enough that there is essentially no thermal conduction in the target during the pulse [17]. Since the Nd:YAG laser used in this research has pulse lengths in the nanosecond range, the two-temperature model will not be further discussed, but for more details, see [40]. For ns-length pulses, the pulse is long enough for thermal conduction in the target to occur [17]. Thus, the thermal model is appropriate to describe ablation in the nanosecond regime for intermediate fluences [17,40,51,52]. The laser energy first heats the target to its melting point, followed by continued heating to the vapor-

ization temperature, causing evaporation from the liquid surface. However, the time scale to heat the target to its vaporization temperature is very short, occurring before the end of the nanosecond pulse. The main source of energy loss is heat conduction into the solid target. In the thermal model, the key component is the temperature profile in the material and its temporal development [52]. In order to obtain the temperature distribution in a target material as a function of time, the one-dimensional (depth) heat conduction equation can be utilized, which has contributing terms from the properties of the target, in addition to properties of the incoming laser beam [53]:

$$\rho c \frac{\partial T}{\partial t} = \frac{\partial}{\partial z}\left(\kappa \frac{\partial T}{\partial z}\right) + (1 - R)\alpha I(t)\exp(-\alpha z). \tag{2.1}$$

The target properties are described by the material density ρ, the specific heat of the target c, the thermal conductivity coefficient κ, the material reflectivity R, and the absorption coefficient α. The laser intensity as a function of time $I(t)$ is also included. Other variables include the temperature T, the time t, and the depth within the material z. The wavelength-dependent variables are R, α and $I(t)$. This is a general equation, which can be used to determine the overall behavior of the system and can be solved for the temperature field if boundary conditions are set. For the targets involved in this research, Equation 2.1 was solved, following the method described in [52]. The literature values for the targets used in the present work are tabulated in Appendix A. The system can be thought of as a semi-infinite medium since L_{th}, or the diffusion length described below, is much smaller than the target thickness. This is an appropriate assumption considering that the targets in this research have a minimum thickness of 2 mm and the diffusion lengths are on the order of 0.1 μm, as seen in Table 2.1. Following [52], the one-dimensional heat-conduction equation

Figure 2.2: A comparison of the laser-induced craters for three different pulse lengths: (A) 200 fs (B) 80 ps and (C) 3.3 ns, from [31]. As the pulse length increases, there is more interaction between the material and the laser pulse. In addition, there is matter in both liquid and vapor form for ns ablation.

becomes

$$T(z,t) = \frac{\alpha F}{4\rho c}\int_0^t d\tau P(\tau)\left[\text{erfc}\left(\alpha L(t-\tau)+\frac{z}{2L(t-\tau)}\right)\cdot\exp\left(\alpha^2L^2(t-\tau)+\alpha z\right)\right] + \frac{\alpha F}{4\rho c}\int_0^t d\tau P(\tau)\left[\text{erfc}\left(\alpha L(t-\tau)-\frac{z}{2L(t-\tau)}\right)\cdot\exp\left(\alpha^2L^2(t-\tau)-\alpha z\right)\right], \tag{2.2}$$

where erfc(x) is the complimentary error function, F is the laser fluence, and τ is the laser pulsewidth. The temporal laser profile, $P(\tau)$, is approximated by a Gaussian distribution [52]:

$$P(\tau) \approx \frac{1}{j\sqrt{2\pi}}\exp[-\tau^2/2j^2], \tag{2.3}$$

where j is the pulse length. The thermal diffusion length, L_{th}, is the depth in which heat is conducted. The thermal diffusion length as a function of time is the depth that heat is conducted in a certain amount of time, expressed by

$$L(t) = \sqrt{\frac{\kappa(t)}{\rho c}}. \tag{2.4}$$

2.2.1 Thermal Conduction Calculation Results

The heat conduction into the target material as a function of time and target depth was studied for the present ablation system (neglecting the background vacuum con-

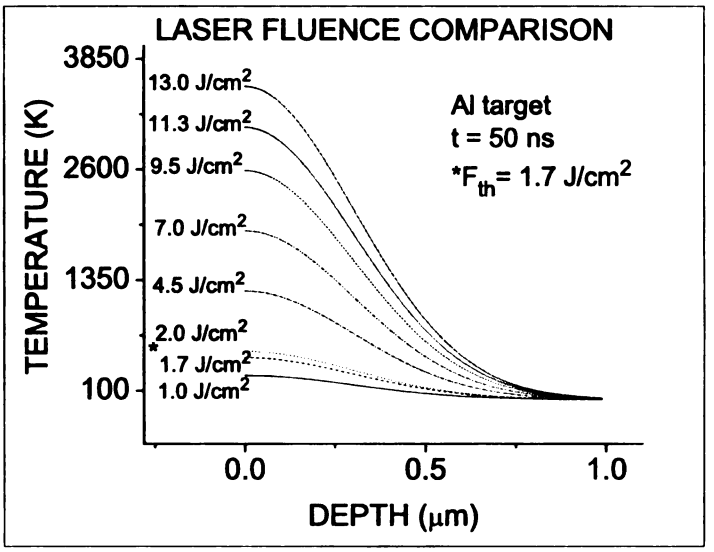

Figure 2.3: The calculated temperature profile in an aluminum target as a function of laser fluence. The calculated threshold fluence for aluminum is 1.7 J/cm^2.

ditions). The effect of the laser fluence, the time after the initiation of the laser pulse and the target material on the heat conduction were investigated.

Heat Conduction as a Function of Laser Fluence

The effect of changing the laser fluence on the temperature profile, while keeping all other variables fixed for an aluminum target 50 ns after the initial laser-target interaction is shown in Figure 2.3. Note that the temperature profile for the calculated threshold fluence for ablation (discussed in Section 2.2.2) for aluminum, 1.7 J/cm^2, is also shown. The maximum surface temperature increases with increasing laser fluence.

Heat Conduction as a Function of Time

The temperature profile in an aluminum target as a function of time after the initiation of the laser pulse is shown in Figure 2.4 for a laser fluence of 13 J/cm^2. The time values in this figure are after the initial laser-matter interaction and in addition, are prior to the start of the next pulse. The profiles of short time scales, on the order of

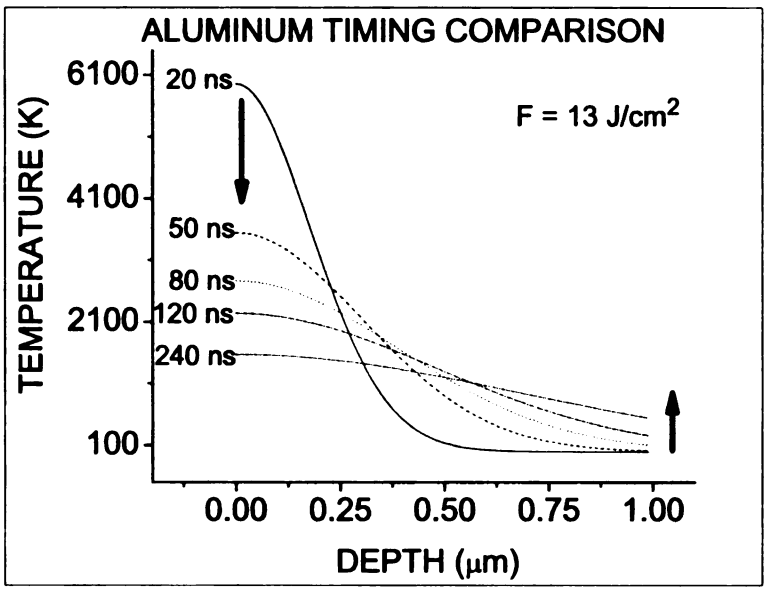

Figure 2.4: The calculated temperature profile in an aluminum target at different time lengths after the initial laser-matter interaction. The laser fluence was kept constant at 13 J/cm^2. The arrows illustrate that as the time after the initial laser-matter interaction increases, the temperature at the surface decreases and more heat is conducted into the material depth. The profiles flatten over time as the heat conduction approaches an equilibrium state.

the pulse length, 4 ns, or slightly longer (10 ns) are not shown since these temperature profiles diverge to infinity at the target surface. An estimate of the approximate surface temperature at the initial laser-matter interaction (i.e. $t = 0$) will be discussed in Section 2.2.3. As the time after the pulse initiation increases, the temperature profile becomes more flat and the energy gets conducted into the target, approaching an equilibrium state, similar to the results of similar calculations in the literature [52]. The effects of the laser fluence and time after the initial laser-matter interaction for an aluminum target are summarized in Figure 2.5. As expected, as the laser fluence increases, the maximum surface temperature increases and as the time increases after the leading edge of the pulse ablates the target, the maximum surface temperature decreases.

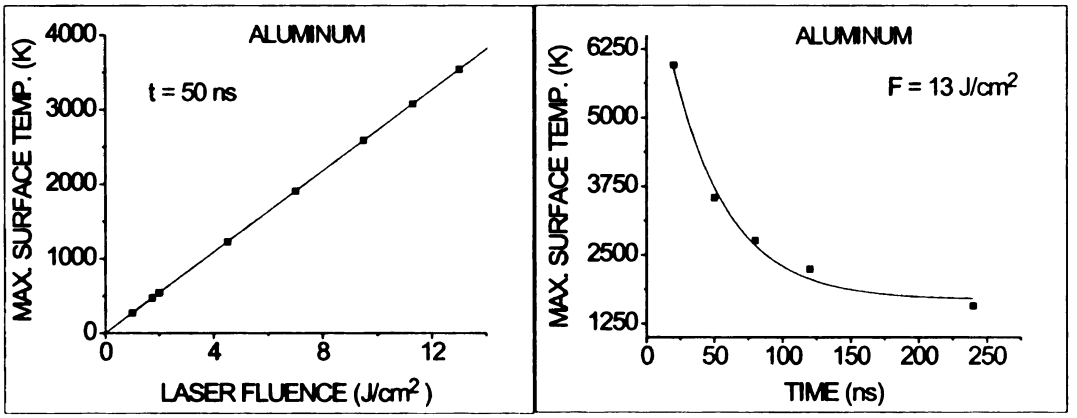

Figure 2.5: The calculated maximum surface temperature during the ablation of an aluminum target as a function of laser fluence and time (ns) after the initial laser-matter interaction.

Heat Conduction as a Function of Target Material

The temperature profiles for all of the targets used in this work are shown in Figure 2.6. The fluence was set to 13 J/cm^2 and the time after the initiation of the pulse was 50 ns. Note that this calculation includes only one laser pulse. The carbon temperature profile starts at a much higher temperature than the other metals, most likely due to its relatively high melting point and low thermal conductivity. The temperature profiles for the metal targets are shown in Figure 2.7.

The temperatures shown in Figure 2.7 after 50 ns are well above the melting and boiling points of these metals, as can be seen in Figure 2.8. The laser energy is instantaneously converted into thermal energy, heating the target surface to a temperature past both its melting and vaporization temperatures, since the deposited energy greatly exceeds the heat of vaporization for the small irradiated volume [54]. For example, for a depth of 0.01 μm in an aluminum target and a fluence of 13 J/cm^2, the approximate energy deposited is 1.3×10^5 kJ/mol. (As a side note, for copper, the boiling point is above the maximum temperature after 50 ns, but the initial surface temperature (discussed below) was well above the vaporization point). The boiling point of any metal will be obtained in less than 1 ns for a laser intensity of 10^9 W/cm^2

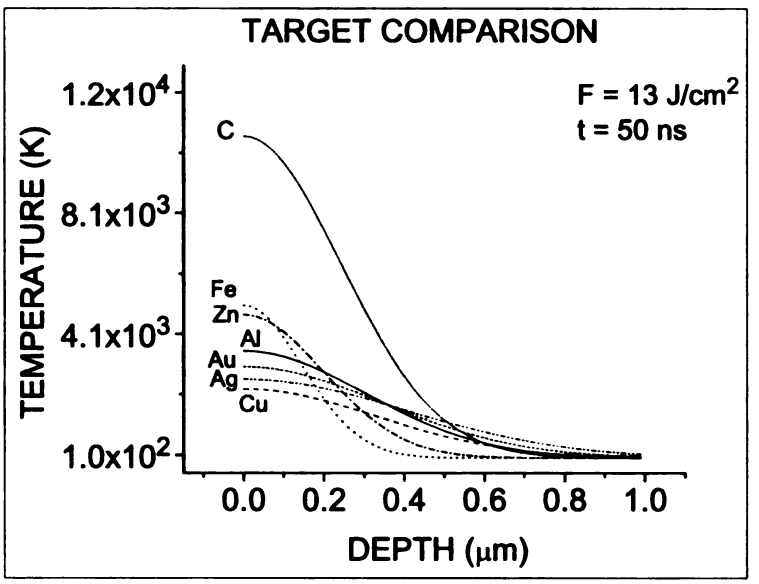

Figure 2.6: The calculated thermal conduction into the solid illustrated by the temperature profile as a function of target depth for the targets used in the present work. The laser ablation was 13 J/cm^2 and the profiles are 50 ns in time after the start of the pulse.

(4 J/cm^2 with the laser system in the present work) [55]. The main source of energy loss is due to the heat conduction into the target depth [17].

The main target property contributing to the temperature profile is the thermal conductivity. Both the maximum surface temperature as a function of κ and the target depth (when the temperature is 500 K) as a function of κ at 500 K are shown in Figure 2.9. As κ decreases, the maximum temperature at the surface of the target increases, and the conduction depth increases, similar to the results seen by others [55].

The thermal conduction model is useful as a general view of the laser-matter interaction, yet fails to describe all of the processes involved, particularly due to the moving solid-liquid interface and the constant loss of material, in addition to the changing optical properties of the target. Also, the thermal conduction model does not completely describe the material removal under extreme conditions. However, this model is useful to see how the temperature profile changes over time in a fairly shallow depth of the targets used in this research.

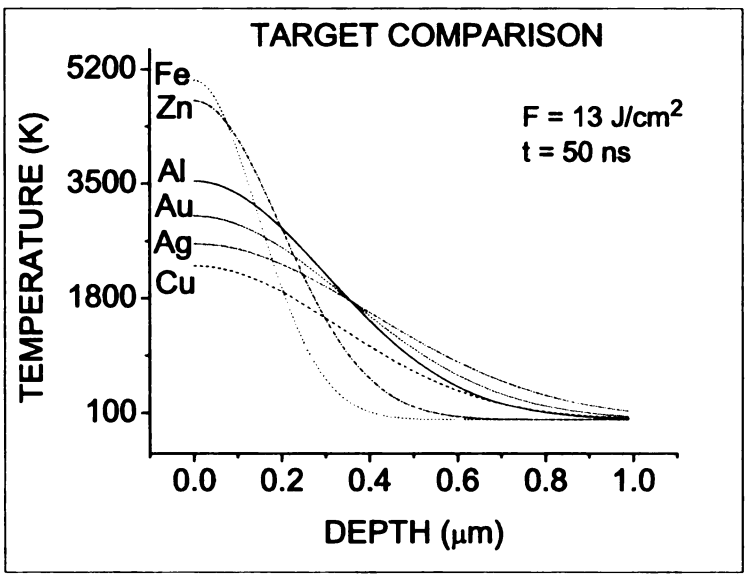

Figure 2.7: The calculated thermal conduction into the solid illustrated by the temperature profile as a function of target depth for a variety of metal targets. The laser ablation was 13 J/cm^2 and the profiles are 50 ns in time after the start of the pulse.

2.2.2 Threshold Fluence for Ablation

The thermal model can also be used to estimate other properties of the system such as the threshold fluence for ablation, or the approximate energy required to melt the surface layer to some depth L_{th}. For nanosecond ablation, the threshold fluence, F_{th} can be approximated by the expression: [17]

$$F_{th} \approx \frac{\rho c \Delta T_m L_{th}}{A}, \tag{2.5}$$

where ρ is the target density, c is the specific heat, ΔT_m is the difference between the target melting temperature and the initial target temperature, and A is the absorbance of the material at a given wavelength (532 nm in this work). The thermal length in the material, L_{th}, was introduced in Equation 2.4 and a similar form can

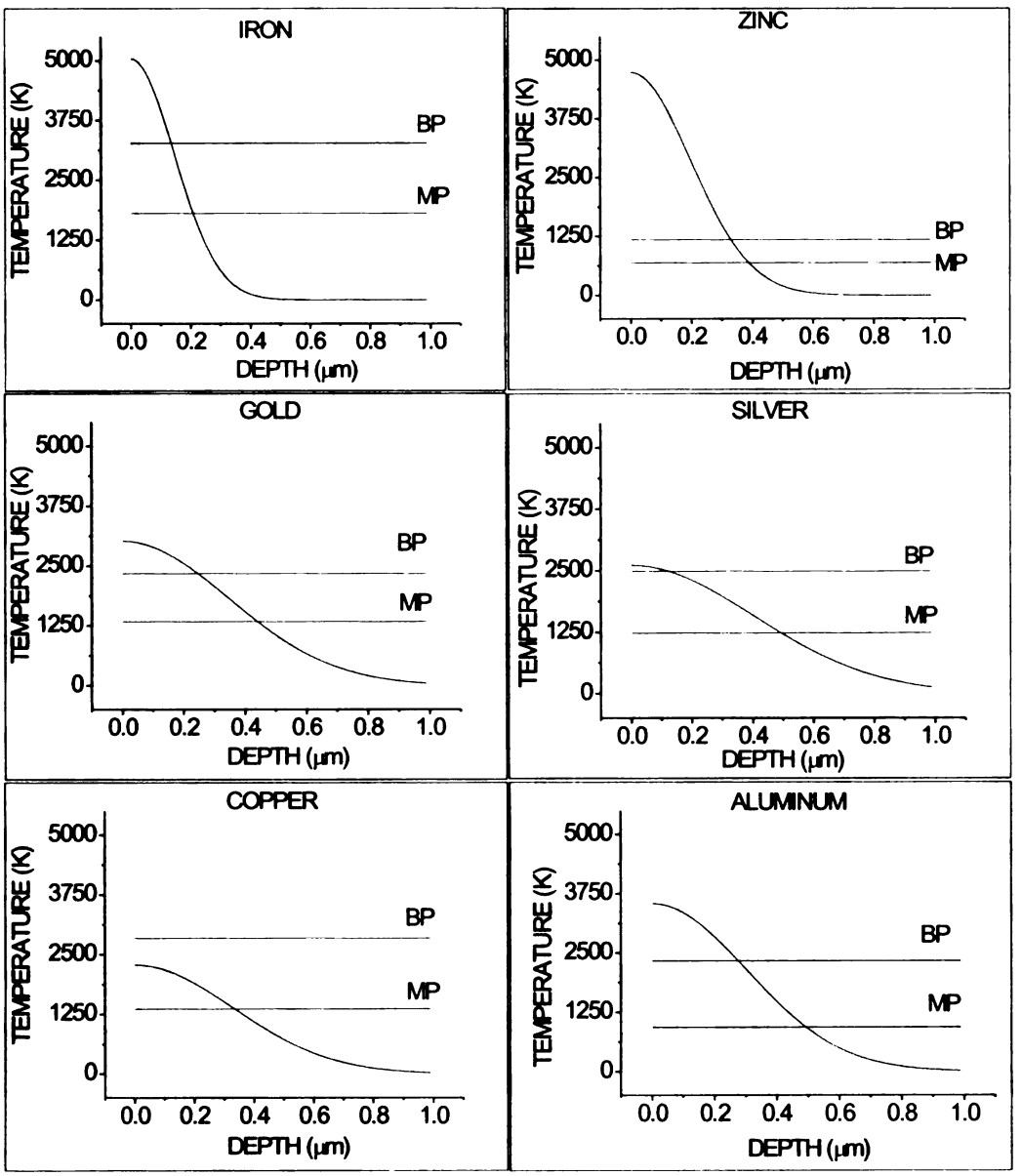

Figure 2.8: A comparison of the thermal conduction shown in Figure 2.7 and the melting and boiling temperatures for each metal target.

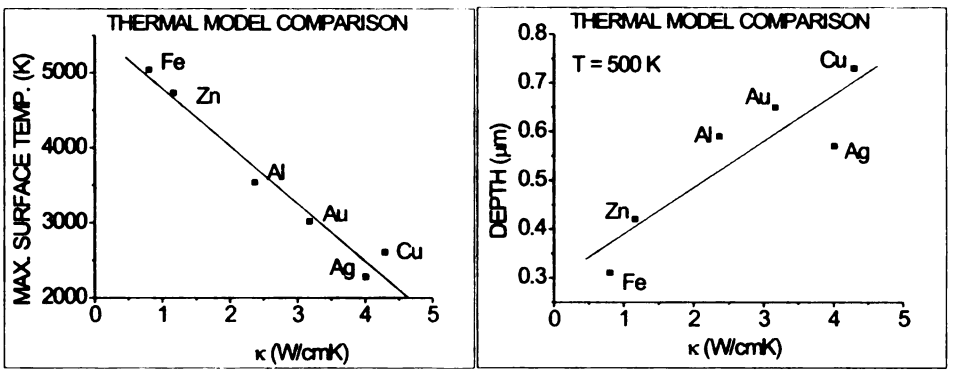

Figure 2.9: The thermal conduction into the target is dependent on κ, the thermal conductivity of the target. A more conductive metal (large κ) has a lower surface temperature since more of the heat is conducted into the target.

be used to determine the thermal diffusion length during the laser pulse [56]:

$$L_{th} = \sqrt{2D\tau_p}, \tag{2.6}$$

where τ_p is the laser pulse length and D is the heat diffusion coefficient:

$$D = \frac{\kappa}{\rho c}, \tag{2.7}$$

where κ is the thermal conductivity. As indicated above, a nanosecond length pulse is long enough for a thermal wave to propagate in the target to a layer of thickness L_{th}, which stores the absorbed energy. The values of L_{th} are given in Table 2.1, and are similar to literature values [52]. The calculated threshold fluences are also given in Table 2.1, which are similar to the typical values found for metal targets, 1-2 J/cm^2 [17]. The threshold fluence for silver is fairly high, due to its relatively large reflectivity at 532 nm, which causes A, the absorbance, to be small, in addition to relatively large values for D and L_{th}. These calculated threshold fluences will be compared to the experimental values in Section 4.3.

Table 2.1: Calculated fluence threshold for ablation of metal targets used in this research.

Target	D (cm^2/s)	L_{th} (μm)	F_{th} (J/cm^2)
Al	0.979	0.088	1.739
Fe	0.227	0.043	0.526
Cu	1.162	0.096	0.924
Zn	0.419	0.058	0.580
Ag	1.738	0.118	3.197
Au	1.270	0.101	1.107

2.2.3 Surface Temperature Approximation

When the laser beam interacts with the target, a large temperature gradient is formed in the target, as discussed earlier. An approximate value for the temperature change at the target surface at the start of the laser-matter interaction can be written as [57]:

$$(T - T_0) \approx \frac{(1 - R)F}{L_{th}\rho C_p}, \tag{2.8}$$

where R is the reflectivity, F is the laser fluence, ρ is the density of the target, L_{th} is the heat diffusion length as a function of pulse length (Equation 2.6), and C_p is the molar heat capacity at constant pressure. The change in surface temperature calculated with Equation 2.8 are shown in Table 2.2. As expected, at lower fluences, the temperature change is lower, and not as much thermal conduction occurs. In addition, the surface temperature at F_{th} (assuming the initial temperature is 298 K) corresponds to the melting points of each metal, as expected from Equation 2.5. At a higher laser fluence of 13 J/cm^2, the resulting temperature change is much larger, as is expected from the thermal model calculations discussed earlier. Note that this is an approximation of the instantaneous surface temperature only.

Table 2.2: Calculated temperature change at the surface of each metal target during ablation. The temperature change is shown for both the calculated threshold fluences (from Table 2.1), and at 13 J/cm^2, for comparison.

Target	$T - T_0$ (K) at F_{th}	$T - T_0$ (K) at 13 J/cm^2
Al	638	4768
Fe	1513	37384
Cu	1061	14928
Zn	398	13621
Ag	939	3842
Au	1042	12236

2.3 Photon Absorption Mechanism

During a nanosecond laser pulse, the laser interacts with the dense evaporated material, creating an isothermally expanding hot, ionized plasma. The creation of the plasma is primarily due to two photon absorption processes that occur: inverse bremsstrahlung (IB) and photoionization (PI) [52,58,59]. Inverse bremsstrahlung is the process of photon absorption by free electrons, generated during the chaotic laser-matter interaction. These free electrons gain kinetic energy, and induce further ionization of the surrounding material, resulting in an avalanche process [55, 58]. Photoionization by either a single photon or multiple photons (multiphoton ionization, MPI) is the ionization of a species due to an energetic photon. The absorption coefficients for these processes, α_{ib} and α_{pi}, are wavelength-dependent:

$$\alpha_{ib}(cm^{-1}) \propto \lambda^3 \tag{2.9}$$

$$\alpha_{pi}(cm^{-1}) \propto \lambda^{-3} \tag{2.10}$$

For IB, the probability is directly proportional to the wavelength cubed, and for MPI, it is inversely proportional to the same power. Therefore, IB is more dominant at longer wavelengths, as in infrared (IR) laser ablation, while MPI as is dominant at shorter wavelengths, as in ultraviolet (UV) and visible laser ablation applications. The

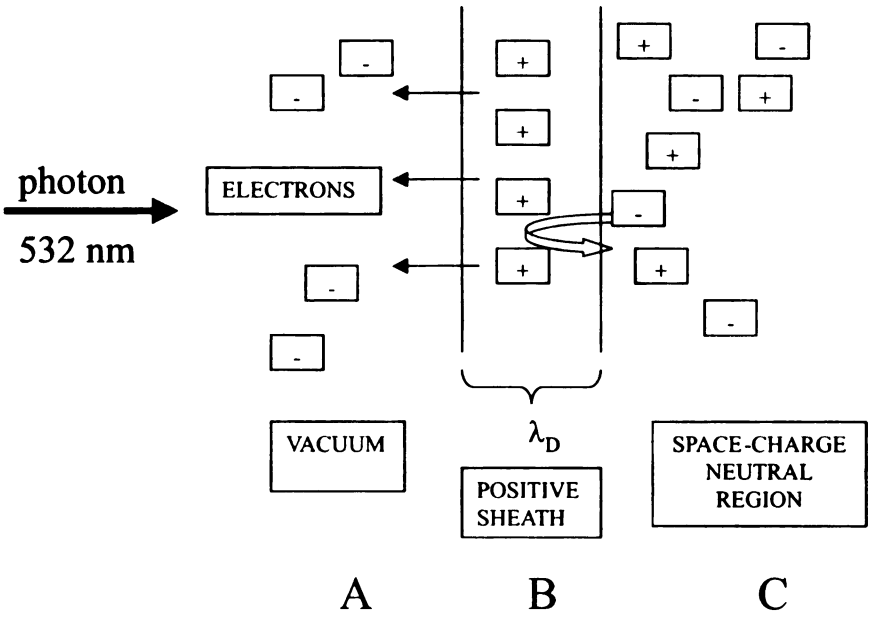

Figure 2.10: The regions of a plasma, adapted from [64]. Region B is the boundary between the vacuum, Region A, and the plasma interior, Region C. The length of the positive sheath, Region B, is the Debye length, λ_D.

relative contributions of these processes during ablation can also change. In addition, the concentration of ions in the plasma affects the degree of IB. As the concentration of ions increases, IB becomes more dominant. These processes raise the temperature of the plume (the material that has left the surface), and in addition, cause both the concentration of ions and the electron density to increase, which in turn increases the density of the plasma.

2.3.1 Plasma Screening

At higher fluences, the density of the plasma increases due to IB and MPI/PI, and the plasma begins to shield the target from further ablation, a phenomenon commonly described in the literature [17, 40, 48, 52, 59–63]. Plasma shielding has been seen in both ablation in a buffer gas [52] and in vacuum [60].

The Debye length, λ_D, gives the characteristic screening length of a plasma, and is shown schematically in Figure 2.10, with incident laser radiation from the left. In

Table 2.3: Debye length of the metal targets

Target	T (K) at 13 J/cm^2	$\lambda_D(\mu m)$
Al	5041	4.9
Fe	37657	13.4
Cu	15201	8.5
Zn	13894	8.1
Ag	4115	4.4
Au	12509	7.7

plasmas, a region occurs which is space-charge neutral. The Debye length is the length of the sheath, Region B, which is the boundary between the interior of the plasma, Region C, and the vacuum, Region A. Region B is depleted of electrons, which are able to move rapidly to the vacuum. The collective loss of the fast electrons creates a strong potential [47]. The potential repels further plasma-created electrons in Region C from leaving, which is indicated by the curved arrow [64]. Region B shields the plasma from external fields, preventing further laser-target interaction. The Debye length, λ_D, can be estimated by the expression: [47]

$$\lambda_D = \left(\frac{kT_e}{4\pi n_e e^2}\right)^{1/2}, \tag{2.11}$$

where T_e is the electron temperature of the plasma in K, n_e is the electron density in cm^{-3}, k is Boltzmann's constant, and e is the charge of an electron. For the plasma created under the different conditions in this research, the approximate Debye lengths (in μm) are given in Table 2.3, assuming initial plasma temperatures based on earlier calculations (Section 2.2.3) and an approximate electron density of $\sim 10^{12}$/cm^3, obtained from the literature [62] for a laser ablation created plasma under similar conditions to the present work.

When the Debye length or the screening length is large, the target is shielded from further ablation. As the laser fluence increases, a saturation point is reached, where the leading edge of the laser pulse creates and interacts with the plasma, which shields the target from further ablation from the "tail" of the laser pulse. Evidence

for such plasma shielding was seen in this research, and will be further discussed in Section 4.3.4.

2.4 Plasma Expansion

The process of ablation releases a large amount of material from the surface, with which the laser further interacts, creating a plasma, which isothermally expands until the end of the laser pulse, as previously described. The plasma then adiabatically expands into either the vacuum or the background gas, when present. The energy of the plasma dissipates due to thermal radiation or by being converted into hydrodynamic motion. The plasma expands and cools completely before the start of the next pulse [63]. This section will focus on the expanding plume after the completion of the laser pulse.

2.4.1 Plasma Properties

The laser-created plasma not only shields the target from further ablation, but it is also expanding and evolving. The plasma, also referred to as the laser ablation plume, adds a great deal of complexity to the ablation mechanism and has been studied extensively, but is not very well understood. The present section will discuss a few parameters applicable to this research, including properties of the plume and its characteristic behavior.

2.4.2 Velocity

During an adiabatic plume expansion under vacuum conditions, the thermal energy is converted into kinetic energy. Under the adiabatic approximation, the vaporization of the target, plasma formation, and expansion can all be considered separate processes [17], making it possible to calculate various parameters of the system including the

Table 2.4: The initial calculated velocity of the plume created during the ablation of the targets used in this research. The laser fluence was 13 J/cm^2.

Target	v_0 (cm/s)
C	$1.76 \cdot 10^6$
Al	$1.11 \cdot 10^6$
Fe	$2.11 \cdot 10^6$
Cu	$1.27 \cdot 10^6$
Zn	$1.20 \cdot 10^6$
Ag	$5.06 \cdot 10^5$
Au	$6.50 \cdot 10^5$

velocity. The plume expands into the vacuum with a free expansion [48]. The velocity, v, of this expansion can be approximated by [47]:

$$v = \left(\frac{2}{\gamma - 1}\right)\left(\frac{\gamma kT}{m}\right)^{1/2}, \tag{2.12}$$

where γ is the ratio of specific heats of the material in the plume, and ranges from 1.2 to 1.3 [65], k is Boltzmann's constant, T is the temperature of the target during ablation, and m is the mass of the ablated species. Equation 2.12 was used to approximate the initial velocity of the ablated species under vacuum conditions, with $\gamma \sim 1.25$ [47], resulting in velocities in the range of $v \approx 1.6 \times 10^6$ cm/s, shown in Table 2.4 for a laser fluence of 13 J/cm^2. The values are similar to the initial velocities predicted by others [41,47] and will be particularly useful for comparing to the results of the gas cell laser ablation, which will be presented in Chapter 5.

2.4.3 Plume Length

The length of the plume under different conditions is important for determining the type of target holder and target to use for ablation, which will be discussed in Sections 4.1.5 and 5.2.1. Two models were used to calculate the plume length: an adiabatic model and a Monte Carlo model (SRIM). The length of the plume is a function of a number of parameters including the laser energy, background gas pressure, and the

Table 2.5: Parameters, both calculated and known, for plume length calculation of the laser ablation of an aluminum target in background He gas.

Parameter	value
γ	1.66
ν_0	$1.57 \cdot 10^6$ cm/s
τ_p	$4 \cdot 10^{-9}$ s
ω	0.006 cm^2
θ	30^o

plume geometry. In the adiabatic expansion model [66], the particles in the ablation plume and the background gas push against each other until an equilibrium is established. Based on this picture, the plume length, L, upon equilibrium is approximated as

$$L = A[(\gamma - 1)E]^{1/3\gamma} P_o^{-1/3\gamma} V_i^{(\gamma-1)/3\gamma}, \tag{2.13}$$

where

$$V_i = \nu_0 \tau_p \omega \tag{2.14}$$

and

$$A = \left(1 + \frac{1}{\tan\theta}\right)\left(\frac{3\tan\theta}{\pi + 2\pi\tan\theta}\right)^{1/3}. \tag{2.15}$$

The parameter V_i, given in Equation 2.14, is the initial volume of the plume, where ν_0 is the initial plume velocity, τ_p is the laser pulse width, and ω is the beam spot area at the aluminum target. The parameter A, given in Equation 2.15 is a geometrical factor for a conical expansion geometry of the plume. The value for θ was estimated to be 30 degrees, based on work in the literature for an aluminum target [67]. Other parameters include the laser energy incident on the ablation target E, the initial background gas pressure P_o, and the specific heat ratio for the background gas γ (helium for the present work). For the laser ablation system in this research, the parameters are summarized in Table 2.5.

The results of calculations of the plume length are shown in Figures 2.11 and 2.12.

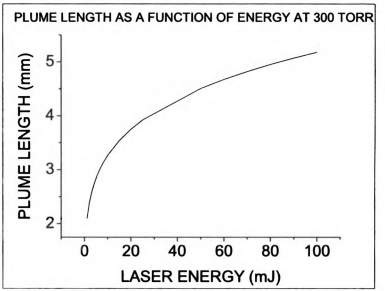

Figure 2.11: The adiabatic calculation of the plume length as a function of laser energy for an aluminum target in 300 Torr helium gas.

In order to determine the plume length as a function of laser energy incident on the target (Fig. 2.11), the pressure was kept constant at 300 Torr. As the laser energy increases, the plume length also increases due to the increased amount of ejected material (plasma shielding is not included in this calculation). For the calculations of the plume length as a function of the background helium pressure (Fig. 2.12), the laser energy was kept constant at 6.45 mJ. As the pressure increases, the plume length decreases due to increased interactions with the background gas. Plasma shielding, which was neglected in the model, will decrease these plume lengths.

The Monte Carlo program SRIM (Stopping and Range of Ions in Matter) [68] was also used to model the plume length for an aluminum ablation target, as shown in Figures 2.13 and 2.14. The plume length is essentially the stopping range of ions in matter, which is helium gas in this case. The kinetic energy of the ions in SRIM was based on the calculated values for the initial velocity in Table 2.4. The SRIM calculations also show the increase in plume length as a function of initial kinetic energy, and a decrease in length as a function of increasing pressure. The Monte

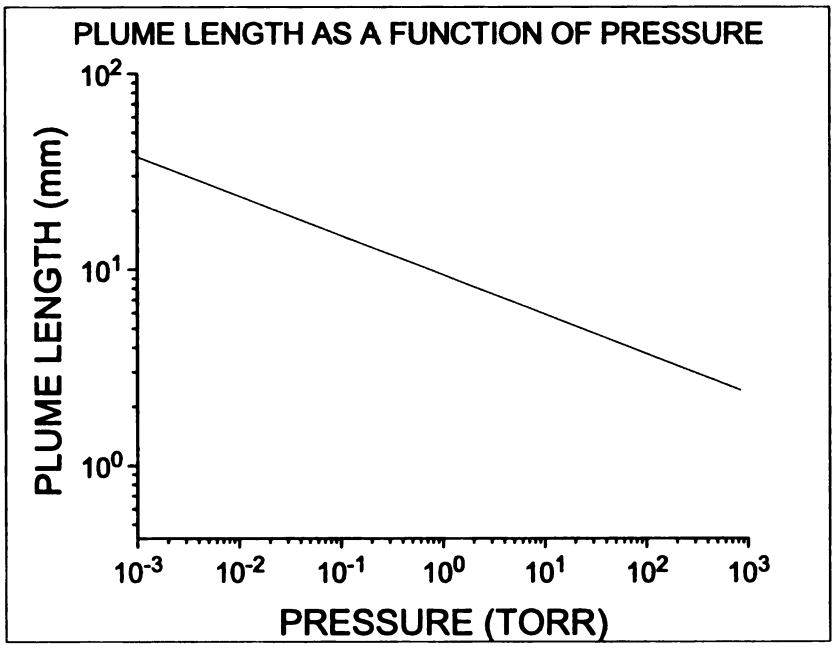

Figure 2.12: The adiabatic calculation of the plume length as a function of background pressure for an aluminum target. The laser energy is 6.45 mJ.

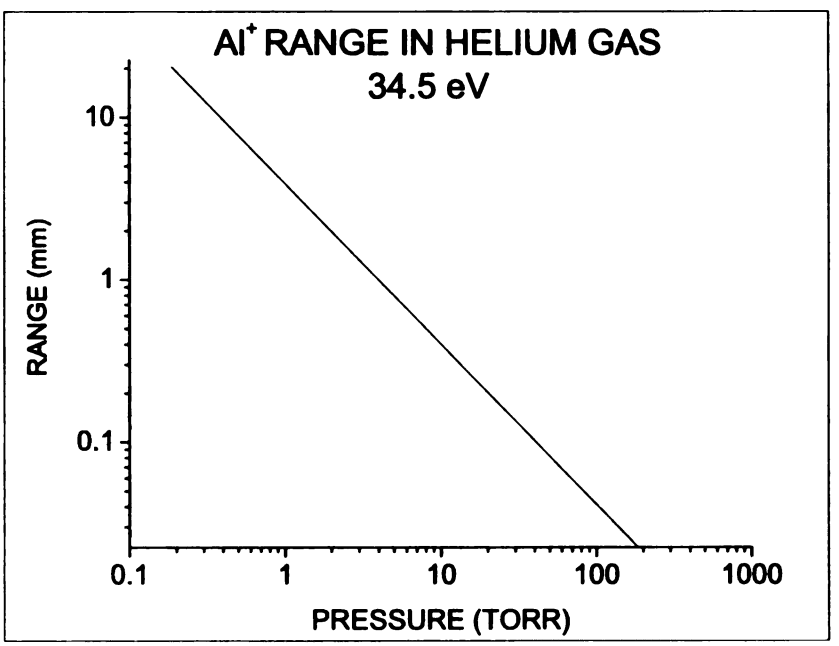

Figure 2.13: SRIM calculation of the plume length as a function of background pressure for an aluminum target. The kinetic energy of the ions is 34.5 eV.

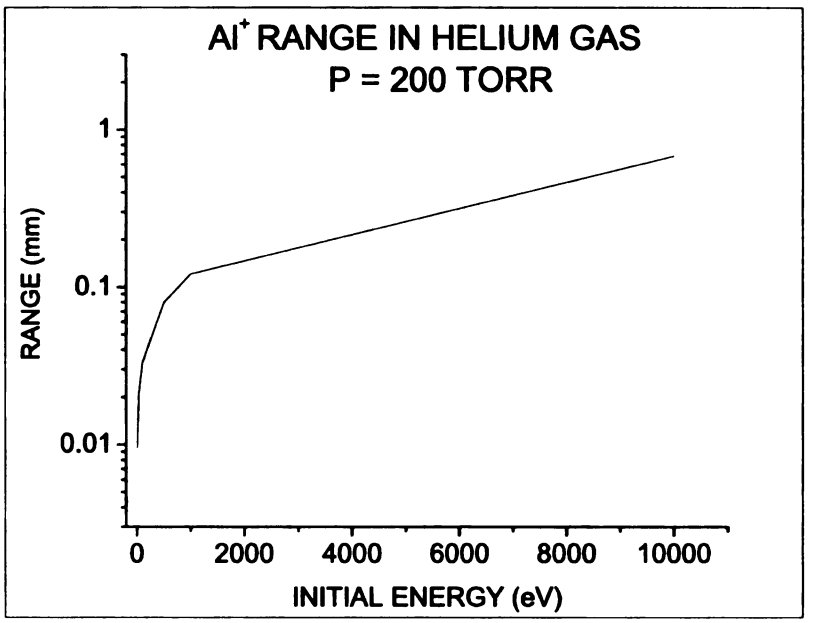

Figure 2.14: SRIM calculation of the plume length as a function of the kinetic energy of the ions for an aluminum target.

Carlo (SRIM) and adiabatic models agree at lower pressures, but diverge at higher pressures, as shown in Figure 2.15. The divergence is similar to other results [67], in which the calculated plume length at higher pressures is smaller than the adiabatic expansion model length. The SRIM calculations do not take plume collisions into account, and variables including laser energy, pulse length, and beam diameter, in addition to the plume geometry are not taken into account. On the other hand, the plume geometry changes at higher pressures [69], thus causing the adiabatic model to over-estimate the plume length. The plume length calculation helped to determine the ablation target geometry to optimize laser ablation, particularly when a background gas was present.

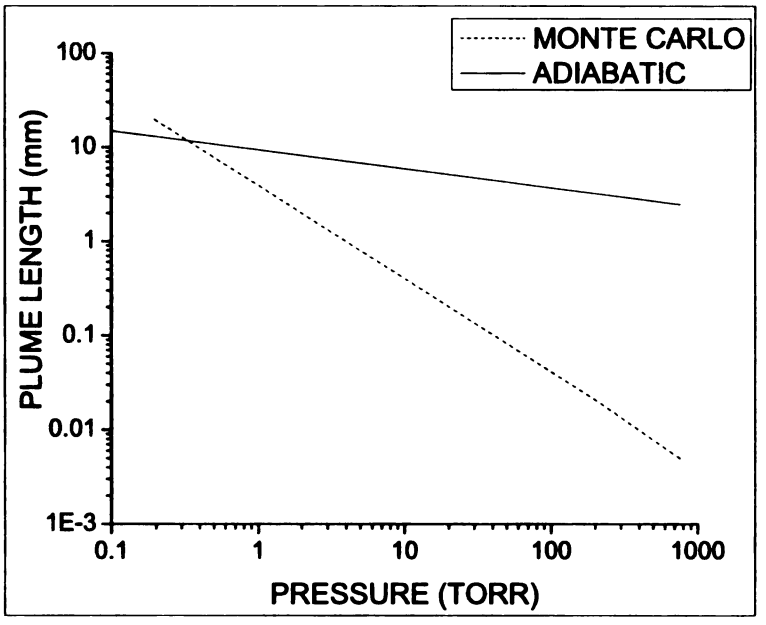

Figure 2.15: A comparison of the calculated plume length as a function of pressure using the adiabatic model and the Monte Carlo model SRIM. The models agree at lower pressure, but diverge at higher pressures.

2.4.4 Plume Splitting

As mentioned, it is evident that laser ablation with the added complication of a background gas can result in various processes including clustering, deceleration, plume oscillations, shock wave formation, thermalization, and plume splitting that are typically not present in vacuum. Like most processes associated with laser ablation at present, these processes are often impossible to separate. One phenomenon particularly applicable to the present study was plume splitting. Many authors have noticed that the plume is temporally split into fast and slow components, the slow being thermal components [70]. The plume typically splits at pressures greater than approximately 100 mTorr [67], although the plume has also been found to split under background vacuum conditions [70]. A variety of mechanisms or descriptions for these phenomena exist, and will be discussed further in Section 5.4.3 as part of the description of the plume splitting seen during the laser ablation of a carbon target in helium

in the present work.

2.5 Laser Ablation Theory and Calculations: Conclusion

The goal of this chapter was to introduce the theory behind the mechanisms and processes associated with laser ablation. Using the laser ablation models, various aspects of the laser ablation system in this research were calculated, including the expected threshold fluence and the length of the ablation plume. The approximations were complementary to the results discussed in Chapters 4 and 5, contributing to a broader understanding of the processes involved in laser ablation. The next chapter will describe some simulations done to describe the transport of the ions produced during ablation.

Chapter 3

Ion Transport Calculations

After the ions are produced in the laser ablation process, the ions must be transported for detection or for other applications such as their use as test ions. This section will provide details on simulations of the ion transport and, in addition, an introduction to ion mobility, which is important for ablation in the gas cell.

3.1 SIMION Calculations

SIMION can be used to approximate the transport of ions within an electrode system and was used to simulate the ion transport in the laser ablation system in the present work. As mentioned, the laser ablation system involved two chambers. The ions produced during ablation in either chamber are guided by a series of ring electrodes to either an exit nozzle in the case of the gas cell or to a detector in the high vacuum chamber. The detector in the high vacuum chamber is a residual gas analyzer (RGA) and will be discussed further in Chapter 4. An electric field is applied to the ring electrodes, creating a potential gradient, which will be described in detail in Section 4.1.2. A close-up of the ring electrodes is shown in Figure 3.1. The system has 21 ring electrodes connected by a linear resistor chain ending slightly above ground potential, due to an external resistor. The ablation target holder assembly is located at the cen-

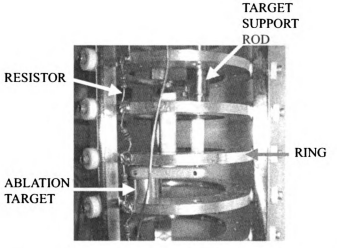

Figure 3.1: Photograph of the ring electrodes. The target assembly, supported by a long rod, is located in the center of the electrodes and resistors connect the rings.

ter of the rings electrically isolated and is off-center, being supported by a long rod, as seen in Figure 3.1. The geometry of the electrode system can be placed into SIMION and the ion transport can be simulated. The simulations are particularly useful to aid in determining whether the system geometry is conducive to ion transport and in estimating the needed electric field to transport ions effectively.

3.1.1 SIMION Calculations of Laser Ablation in the High Vacuum System

The ion optics and trajectories were modeled in SIMION to determine the effect of the electrostatic potential gradient on the system. The electrode system generally had a cylindrical symmetry but had to be modeled in 3D due to the shape of the laser target assembly. The geometry of the system was inserted into SIMION and various parameters were set, including the mass of the ions and the number of ions. The effect of both the potential gradient and the target voltage on the ion transport in the high vacuum chamber on the ion transport was modeled in SIMION.

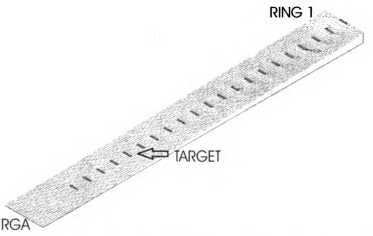

Figure 3.2: The potential gradient in SIMION created by the ring electrodes with +1000 V on the first ring and 0 V on the RGA.

Potential Gradient in SIMION under Vacuum

For the potential gradient effect simulation, the voltages on each ring were set in proportion to a linear decrease of the voltage from the highest value to slightly above zero on the last ring, and 1000 $^{63}Cu^{+}$ ions that originated at the target were sent through the system. The potential gradient is shown in Figure 3.2 and Table 3.1 provides a few possible gradients. Some of the results of the simulation are shown in Figure 3.3. In this figure, the voltage on the first ring is indicated, along with the voltage on the RGA, 0 V. The steep voltage gradient of 2.6 V/cm (with 1000 V on the first ring) accelerated the ions so that they hit the chamber wall, although some still made it to the RGA. As the gradient was decreased, more ions were found to reach the RGA detector. However, when the gradient was decreased to 0.1 V/cm, the ions did not reach the detector, implying that a very gradual potential gradient is not effective for ion transport. This simulation provided an estimate of an appropriate potential gradient of approximately 0.5 V/cm for ablation in vacuum for this system.

Target Voltage in SIMION under Vacuum

The effect of changing the voltage on the target within a constant potential on the ring electrodes was also simulated (in vacuum conditions). For these tests, the first

Table 3.1: SIMION potential gradients on the ring electrodes.

Voltage on Ring One	Potential Gradient (V/cm)
1000	26
500	13
80	2.1
75	2.0
20	0.5
5	0.1

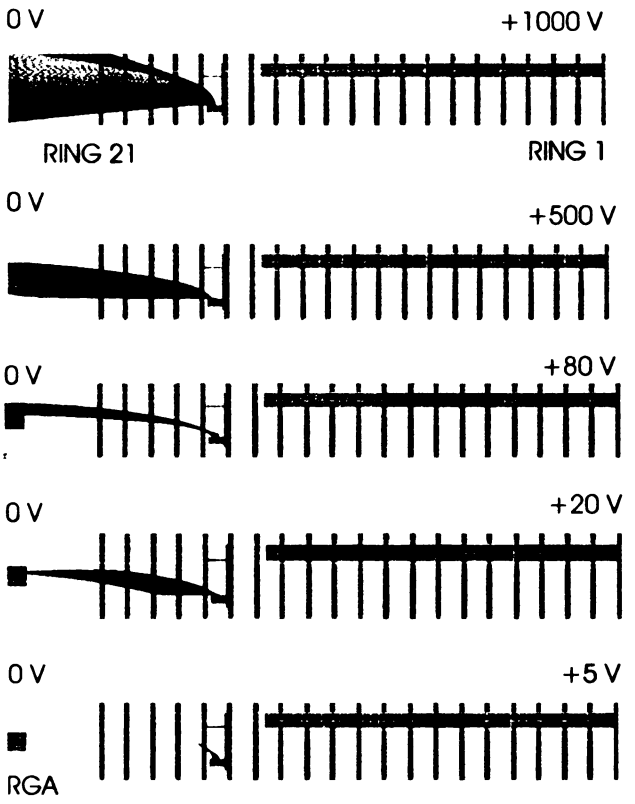

Figure 3.3: SIMION simulation of the potential gradient effect on the ion trajectories during the laser ablation of a Cu target in the high vacuum chamber; 1000 ions were used. The dark lines ending on the left side of the figure show the ion trajectories.

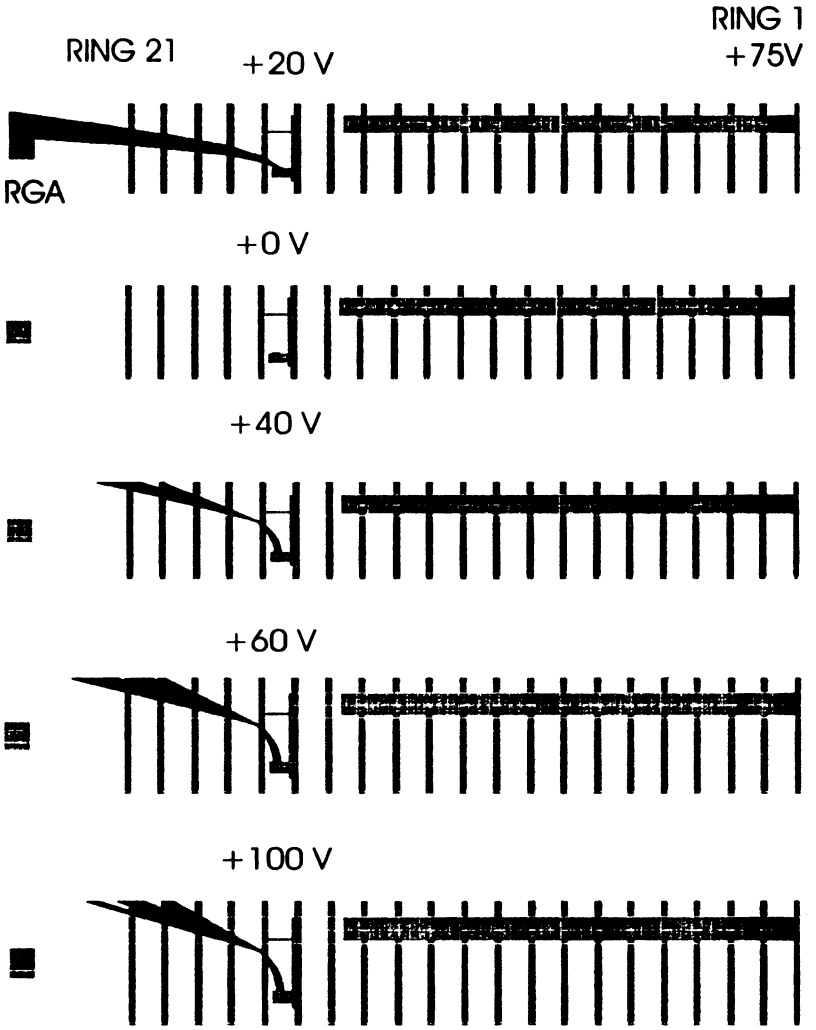

Figure 3.4: SIMION simulation of the target voltage effect on the ion trajectories during the laser ablation of a Cu target in the high vacuum chamber; 1000 ions were used.

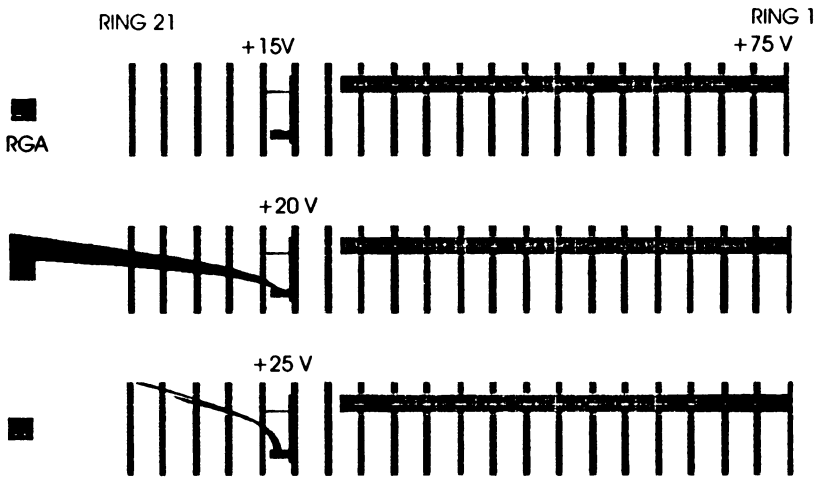

Figure 3.5: The effect of changing the target voltage by 5 V on the ion transport.

ring was set to 75 V, and the rest of the electrodes were set according to a linear voltage drop based on the resistor chain producing a potential gradient of 2.0 V/cm across the ring electrodes. In this simulation, the ablation target was located between Rings 16 and 17, which were set to 23 V and 20 V, respectively. The applied target voltage greatly affects the amount of ions reaching the detector in this simulation, as shown in Figure 3.4. Increasing the target voltage results in an acceleration of the ions into the chamber walls. If the target voltage is decreased from 20 V, the ions do not leave the target. The target voltage is even sensitive at the level of 5 V, as seen in Figure 3.5. These simulations provide some insight into the effects of the applied electric field, in addition to approximate values of the applied voltage that should be used for ion transport for ablation under vacuum conditions.

3.1.2 SIMION Calculations of Laser Ablation in the Gas Cell

SIMION was used to simulate the ion trajectories during laser ablation in the gas cell with the addition of a buffer gas, similar to the SIMION calculations just discussed. The motion of ions in an electric field with a buffer gas is qualitatively different from that in vacuum. The ions are not accelerated, but rather, drift along the field lines.

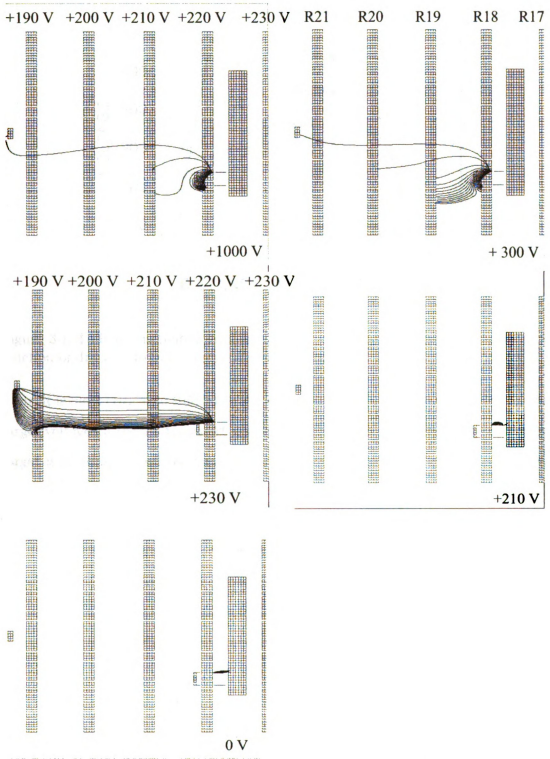

Figure 3.6: SIMION simulation of the target voltage effect on the ion trajectories during the laser ablation in the gas cell in the region of Rings 17-21. A small collection point at +150 V collects the ions.

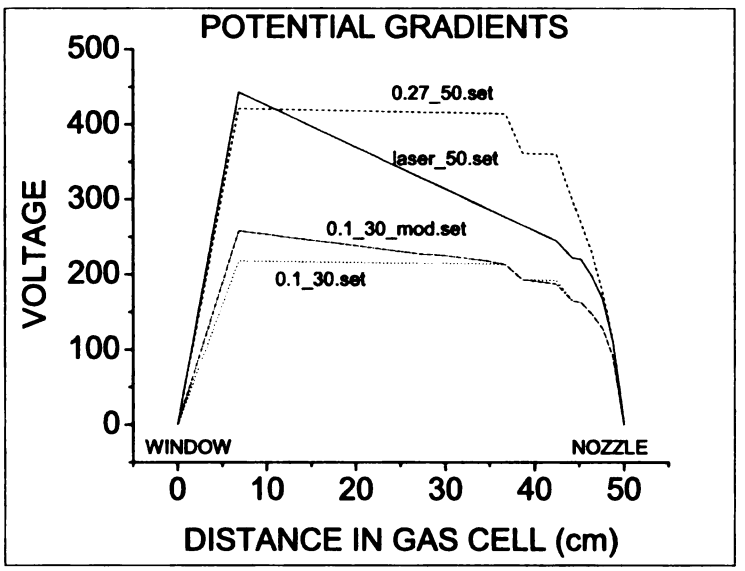

Figure 3.7: Different potential gradients in the gas cell; the voltage is shown as a function of distance from the entry window in the cell.

Thus, it is most critical to simulate the motion near the target. First, the effect of the target voltage on the ion transport was studied, as shown in Figure 3.6; the ablation target is at Ring 18 and the ions are transported to a collection point at + 150 V. For these simulations of the ion transport in the gas cell from the laser ablation of a carbon target, a small target holder (Section 4.1.5) was used, the pressure was 300 Torr, the ion mobility was set to 18 V/cm^2s, and the mass of the ions was 36 amu (a typical mass for a small carbon cluster). As seen in Figure 3.6, the target voltage inside the constant potential gradient from the rings again greatly affects the ion transport; the most efficient ion transport occurs when the target voltage matches the potential gradient at Ring 18 (the voltage at Ring 18 is +230 V).

The effect of the potential gradient in this region of the gas cell on the ion transport was also studied. Various potential gradients are shown in Figure 3.7, and the labels are the filenames of these voltage distributions (which will be discussed more later). For these simulations, the small target holder was used, the pressure was 200 Torr, the ion mobility was set to 28 V/cm^2s, and the mass of the ions was 55 amu. The

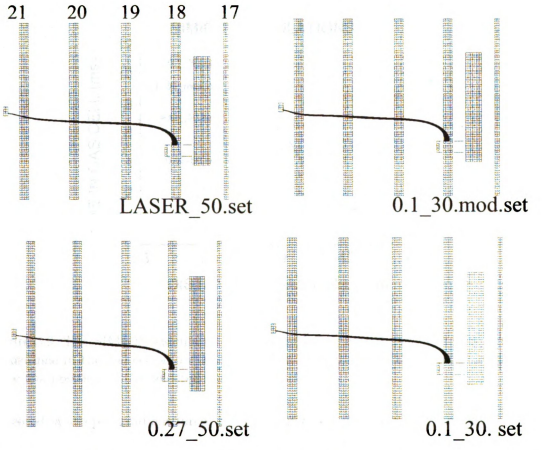

Figure 3.8: SIMION simulation of the effect of the voltage gradient at the end of the rings (Rings 17-21) on the ion transport. The file names of these distributions are also shown (see Figure 3.7).

simulations are shown in Figure 3.8. The ions make it to the collector, regardless of the voltage gradient used, which are almost identical in this region. In general, the voltage distribution over the entire ring electrode structure has the greatest effect on the ion transport.

The time-of-flight of the ions through the gas cell was also modeled in SIMION. The ions were started at different positions within the gas cell, between Ring 18 and Ring 21. For this simulation, 125 ions with masses of 38 amu were used. Figure 3.9 shows the time for ions to exit the gas cell, starting at different positions from Ring 17 to Ring 21 in the gas cell. The time for ions to exit the gas cell when the ions start at Ring 18 as a function of the potential gradient in V/cm is also shown in Figure 3.10. As

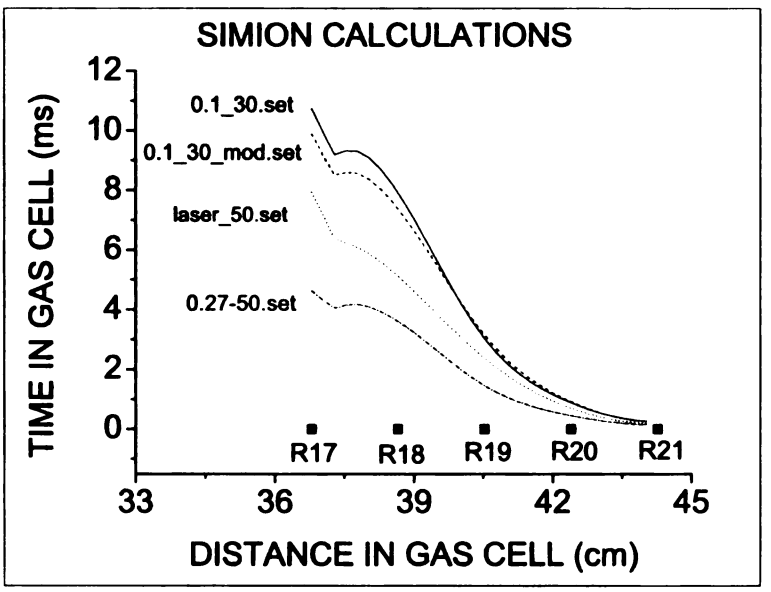

Figure 3.9: The SIMION-calculated time for an ion to exit the gas cell as a function of distance in the gas cell and different applied electric fields. The solid black points show the position of the selected ring electrodes.

expected, a steeper gradient forces the ions out faster than a more gradual gradient. The simulation will be compared to the experimental results of the timing in the gas cell in Section 5.4.4. The simulations done in SIMION were useful to determine the appropriate voltage distributions needed to effectively transport ions and will be compared to some of the results in the present work.

3.2 Ion Mobility Overview

Another aspect of this work was the measurement of ion mobility in the gas cell. Ion mobility measurements have been used to obtain structural information on clusters and biomolecules [71]. In addition, ion mobility measurements have become an important technique for analyzing unknown substances, particularly for national security applications [72]. Ion mobility describes how fast gas-phase ions travel through a gas-filled drift cell with an applied electric field. The ions are accelerated between

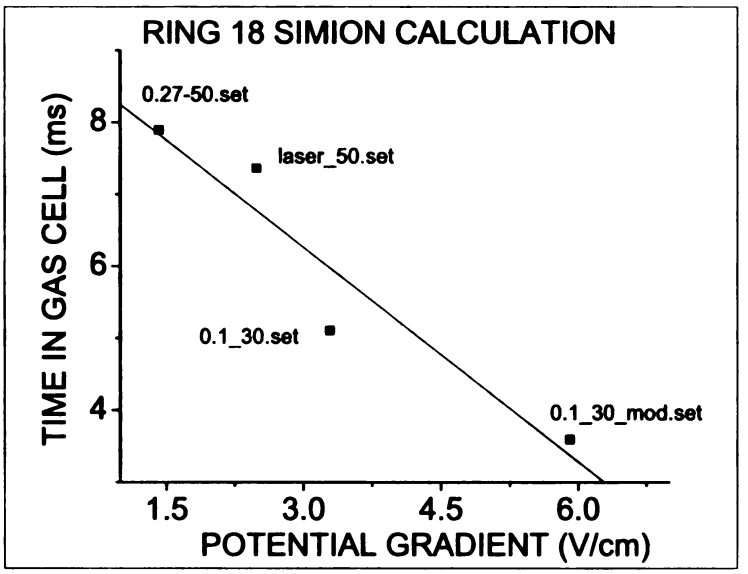

Figure 3.10: The SIMION-calculated time for an ion to exit the gas cell starting at Ring 18 as a function of potential gradient (V/cm). The labels are different voltage files used in the gas cell (see Section 5.4).

collisions by the electric field, yet are slowed by collisions with the background buffer gas. An important result from ion mobility studies is the ion mobility constant, K, which is also called the "scalar" ion mobility constant, and is expressed by

$$\mathbf{v_d} = K\mathbf{E}, \tag{3.1}$$

where $\mathbf{v_d}$ is the drift velocity of the ion and $\mathbf{E}$ is the electric field gradient in the cell [73]. The constant K depends on both the ion and the background gas. If $\mathbf{E}$ is known and the velocity is deduced from a plot of the distance traveled by the ions versus their travel time, K can be determined. To account for the experimental parameters of a given ion mobility measurement, K is replaced by K_0, the reduced mobility, which is defined by

$$K_0 = \frac{p}{760}\frac{273.16}{T}K, \tag{3.2}$$

where p is the pressure of the buffer gas in Torr and T is the gas temperature in Kelvin. The reduced mobility, K_0, thus normalizes K to the molecular number density.

3.3 Ion Transport Simulations: Conclusion

The goal of this chapter was to describe ion transport calculations that were done to model the laser ablation system. The SIMION simulations will be important when considering the results in Chapters 4 and 5. In addition, ion mobility was introduced, since it is a parameter of the ions measured in this research, and will be discussed further in Chapter 5.

Chapter 4

High Vacuum Laser Ablation System

This chapter provides a description of the laser ablation system that was constructed for this work. First, the experimental apparatus will be discussed, followed by calculations describing the system. Finally, the results of the ablation studies in a vacuum chamber and their significance will be presented.

4.1 Experimental Details

Two separate chambers were used for the ablation studies, a high-vacuum (HV) chamber and a gas cell filled with helium buffer gas, both chambers are shown in Figure 4.1. The laser ablation process was first studied under vacuum since the ablation in the presence of a background gas complicates the ablation process. In addition, due to the ultra-high vacuum (UHV) conditions needed for the gas cell, it was necessary to initially study and understand the ablation in a separate, controlled environment. In this section, experimental details are presented that are exclusive to the HV system, in addition to details that are common to both the HV system and the gas cell ablation system. Additional details pertaining only to the gas cell ablation system will

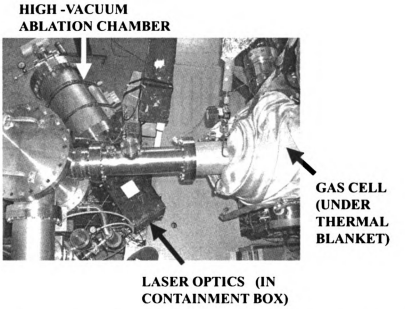

Figure 4.1: The high vacuum and gas cell chambers can be seen in this photograph, in addition to the laser ablation system, all of which is viewed from above.

be presented in Chapter 5.

4.1.1 High Vacuum Ablation Chamber

The laser chamber consisted of a 51 cm (20 inch) long stainless steel cylindrical chamber fabricated by A and N Corporation, as shown in Figure 4.2, with a 25.4 cm (10 inch) diameter. On the back side of this chamber was a 337 mm (13.25 inch) diameter CF flange with three 70 mm (2.75 inch) conflat zero-length reducers, aligned vertically. Attached to the top reducer was a four-way cross that supported a Pirani gauge, an ion gauge, and an air inlet valve for venting the chamber. The Pirani gauge was used to monitor the pressure of the chamber at pressures above 10^{-3} Torr, while the ion gauge monitored the pressure below 10^{-3} Torr. The middle reducer supported a Stanford Research Systems (SRS) residual gas analyzer (RGA), model 300, quadrupole assembly. Finally, an air-cooled turbo molecular pump was attached to the lower reducer. A Varian Scroll Pump was connected to the turbo pump as a backing pump and a block valve was used for the initial pump down. The chamber

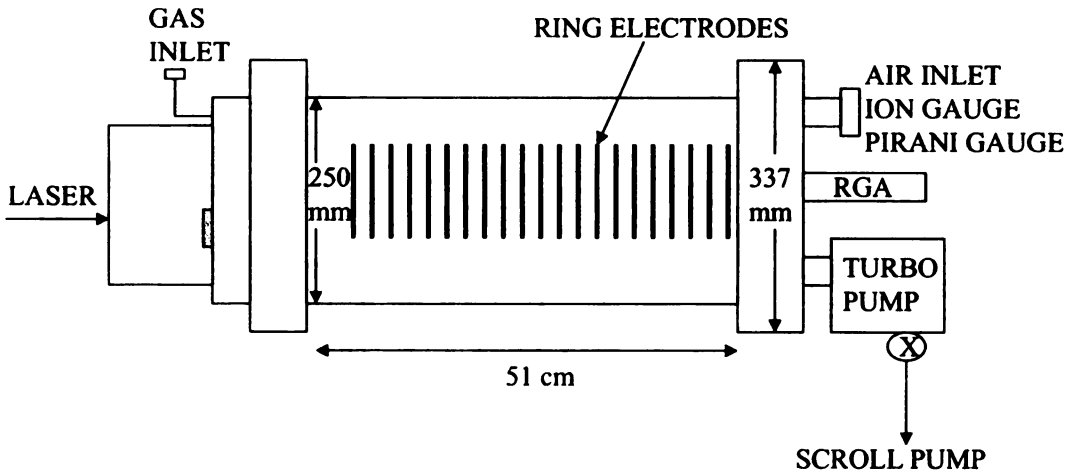

Figure 4.2: A simplified view of the HV laser ablation chamber. The laser enters the chamber from the left through a small window, and is incident on the target (not shown). The main body of the chamber is 51 cm long.

system was supported by a Klinger rail system.

The front face of the chamber, also a 337 mm conflat, supported a 250 mm (10 inch) reducer. This reducer flange supported the ring electrodes, and had a mini-conflat high-voltage feedthrough, to which the ring electrode bias was applied. In addition, a gas inlet valve was also attached to this reducer. The valve was used to introduce 760 Torr of helium to determine the maximum voltage on the rings and target holder when running the laser. This served as a preliminary test prior to moving the ablation system to the gas cell, and will be discussed in Section 4.5. The 114 mm (4.5 inch) diameter laser ablation target assembly fits inside the reducer.

The base pressure of this system ranged from 10^{-7} to 10^{-8} Torr. A mass spectrum from the RGA is shown in Figure 4.3, which is a typical spectrum, showing normal vacuum species and contaminants such as H_2, H_2O, N_2, O_2, CO_2, and some residual hydrocarbons at higher masses most likely from the resistors and wires inside the chamber. This spectrum was taken during the early phase of the work prior to attaining the ultimate base pressure.

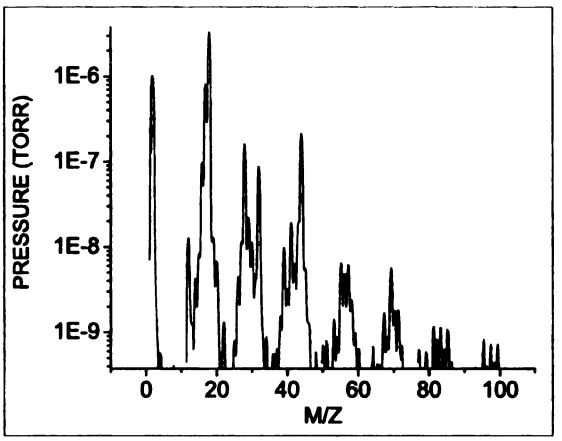

Figure 4.3: A typical spectrum of the contaminants present in the laser ablation vacuum chamber.

4.1.2 Ring Electrodes

A series of ring electrodes, shown in Figure 4.4, were located inside the chamber that created a potential gradient from the DC voltage applied to the high-voltage feedthrough, that were used to direct the ions towards the RGA. The voltage was supplied with a SRS power supply. There were 21 aluminum rings, 4 mm thick, spaced 2.25 cm apart, with a 5.6 cm inner diameter, and with a roughly cylindrical shape. Three rods supported the rings on their outer diameters. The screws connecting the rings to the rods were insulated with ceramic pieces and washers to prevent the rods and screws from creating a short circuit to the support rods. The first ring was approximately 3 cm into the chamber, and the last ring was approximately 2 cm from the rear chamber flange, where the RGA was located. This ring system was initially designed and fabricated at the NSCL for the gas cell, and the first ring had a wire mesh to terminate the electric field. The wire mesh blocked the laser ablation target, and therefore, the first ring was removed for this experiment. The voltage was therefore applied to the second ring. The rings were connected in series with 2 MΩ resistors, which were connected externally to a trimmer resistor set to 600 Ω, in order to keep the last ring slightly above ground potential; the total resistance of this

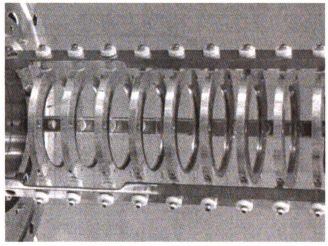

Figure 4.4: Photograph of the ring electrodes without the resistor chain to which a potential gradient is applied to focus the ions toward the RGA.

system was approximately 38 MΩ. The simulated effect of the ring electrodes on the ion transport was discussed previously in SIMION, and the results from the present work demonstrating the effect of the ring electrodes under vacuum conditions will be discussed in Section 4.3.4.

4.1.3 Laser Operation

The laser used in the present work was a Quantel (Big Sky) Q-switched Brilliant Series Nd:YAG laser. The main advantages of this laser are the small "footprint" of the power supply and the self-contained cooling system, in addition to the relatively simple normal maintenance, which can be done by the user.

The principle of operation for a Nd:YAG laser is based on the approximately 1% Nd-doped Yttrium-Aluminum-Garnet (YAG) rod ($Y_3Al_5O_{12}$). This solid-state laser is a 4-level laser. First, flashlamp pumping excites the ground state Nd^{3+} ions, primarily absorbing at 730 nm and 800 nm. The excited state quickly decays to a metastable state forming a population inversion between the $^4F_{3/2}$ and the $^4I_{11/2}$ states. Radiation is subsequently emitted primarily at 1064 nm, as illustrated in Figure 4.5. A second harmonic module attached to the laser head converts the 1064 nm

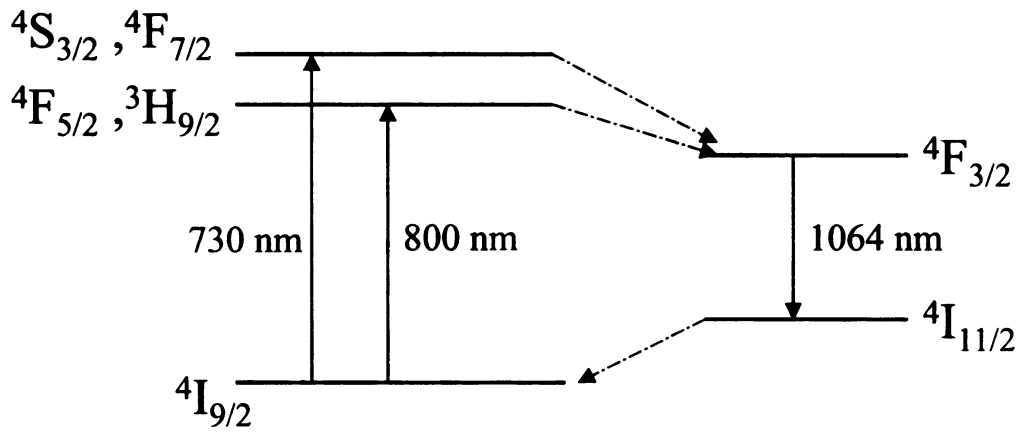

Figure 4.5: Four-level operation of a Nd:YAG laser. The Nd^{3+} ions are excited to their upper energy levels with a xenon flashlamp, and then decay non-radiatively to a metastable state, which emits the characteristic 1064 nm radiation.

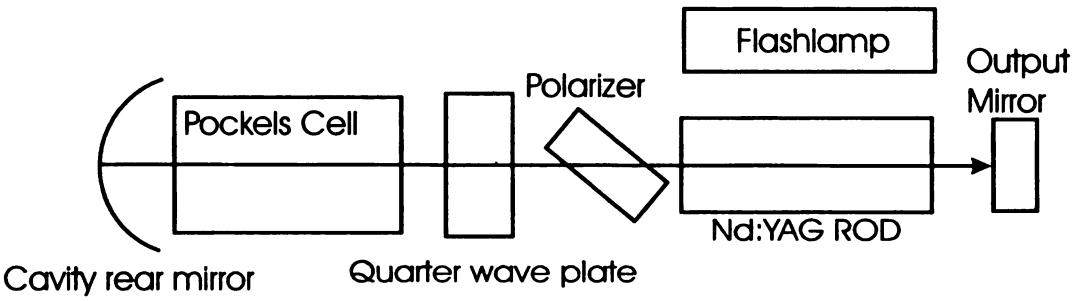

Figure 4.6: The laser cavity of the Brilliant Nd:YAG laser used in this research. The laser beam oscillates in this cavity until the intensity is amplified.

radiation to 532 nm light with a highly deuterated potassium dihydrogen phosphate (KDP) crystal, enclosed in a cell to maintain a stable temperature. At 532 nm, the laser beam has an average energy of 160 mJ per pulse, peak power of 38 MW, pulse width of 4 ns, beam diameter of 4.5 mm, and a repetition rate of 20 Hz. The laser energy was modified for experiments to determine the effect of the laser energy on the ablation yield, which will be discussed later in this chapter. In addition, the repetition rate was modified for ablation experiments in the gas cell in order to trigger the electronics for time of flight measurements and will be discussed in Chapter 5.

A so-called Q-switched laser can produce a short, powerful pulse. The Q-switch is obtained by changing the quality factor, or "Q" of the cavity that is a measure of the

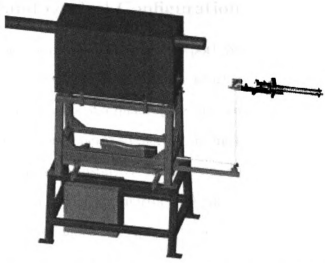

Figure 4.7: A CAD view of the laser ablation system. The laser head rests on an optical table mounted under the last superconducting magnet on the heavy-ion beamline to the gas cell. The entire laser system is enclosed in a safety enclosure to contain any stray light.

internal loss (or gain) in that cavity. If the Q-factor is forced to be unusually low by blocking the laser cavity with an active element such as a Pockels Cell (the electro-optical modulator or Q-switch used in this laser), stimulated emission is prevented and energy builds up in the medium. Once the Q-switch is turned off, the high population inversion is dumped, thus producing a very intense pulse, and the shorter the pulse, the higher the peak power. For an ablation experiment, a Q-switched laser has the advantage that a large amount of power is contained in each pulse.

A schematic of the laser cavity is shown in Figure 4.6. The Nd:YAG rod is 6 mm in diameter and 115 mm in length. The flashlamp contains low-pressure xenon gas. A closed-loop deionized water system cools the rod and flashlamp. The pumping light from the flashlamp is focused onto the rod; both are at the two foci in an elliptical cavity geometry.

4.1.4 Laser and Optical Configuration

The laser head was supported by three Newport ND01-A elastomeric vibrational isolators secured to a Newport optical table, which was attached with vibrational isolators to the steel supports of a quadrupole superconducting magnet, as shown in Figure 4.7. The optical components supported on this table included a halfwave plate, an optical isolator, and a beamsplitter. In addition, a power meter and a 78 cm long rail supporting a mirror holder and mirror were also secured to the table. The laser power supply was located under the optical table and the laser beam was sent in a vertical plane to the target. All optical components had a high damage threshold of 10 J/cm^2, except where noted.

The distance from the laser output to the ablation target in the vacuum chamber was 200 cm, while the distance to the gas cell ablation target was 262 cm. A system of optics was necessary to focus the laser onto both targets. The path of the laser beam is illustrated in Figure 4.8. After the 532 nm beam exited the second harmonic module, it encountered a CVI Laser QWPM-532-06-2 halfwave plate mounted on an 1100-06 15 mm rotary mount, which converted the vertically, or s-polarized light into horizontally, or p-polarized light. The p-polarized light then entered a customized CVI Laser OI-532-6.35-20-PBSO optical isolator, used to prevent any back-reflected light from entering the high-powered laser. This optical isolator acted as a one-way light valve. The incoming horizontally polarized light (p-polarized light) was first sent through a cubic beamsplitter polarizer to eliminate any residual s-polarized light. The p-polarized light then was incident on a quarter waveplate, which converts it to right-circularly polarized light. Any back-reflected light will be unable to pass through the optical isolator, since it will be left-circularly polarized after reflection.

After leaving the optical isolator, the laser beam encountered a beamsplitter, 28 cm from the laser output. Three CVI Laser beamsplitters were available: (1) 67% transmittance, 31% reflectance, (2) 80% transmittance, 20% reflectance, and (3) 2% transmittance, 98% reflectance. These values for the beamsplitter were chosen based

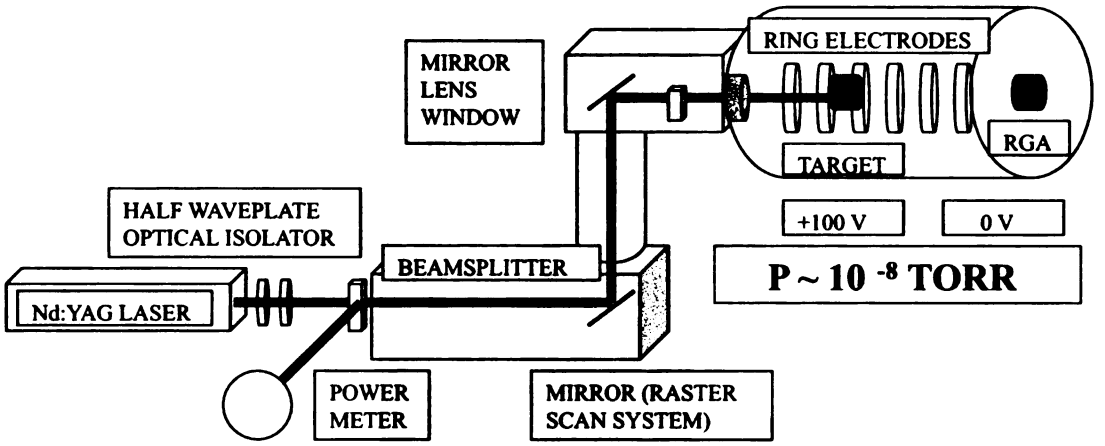

Figure 4.8: The optical path of the laser beam. The length from the laser to the ablation target is approximately 200 cm.

on the estimated energy density needed for the ablation experiments with various targets. The calibrations of these beamsplitters are provided in Appendix C.

Reflected light from the beamsplitter was sent to an Ophir Power Meter, used to monitor the laser power (energy) during experiments to determine the relationship between the laser power and the ion intensity detected by a residual gas analyzer (RGA). The power meter head was a pyroelectric type, model PE50BB-DIF, with a damage threshold of 3 J/cm^2 (a diffuser was attached to the head to allow for the high laser power). The power meter head is a thermopile sensor, monitoring the (temperature-dependent) voltage difference across bi-metallic junctions. This head was connected to the Ophir Laserstar 1Z01600 display and a PC via a RS-232 interface for data acquisition.

The transmitted light was sent via two mirrors, a focusing lens, and a conflat viewport into the vacuum chamber housing the ablation target. The first mirror, or lower mirror, bent the beam up and was raster-scanned in order to minimize drilling effects on the ablation target. The raster scan system will be explained in more detail in this section.

The beam traveling upward was bent onto the horizontal plane by the upper mirror and then sent through a lens mounted on a slide rail to focus the beam at

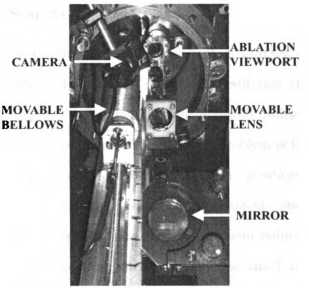

Figure 4.9: Photograph of the laser ablation flange with upper mirror, movable lens, ablation viewport, camera, and the movable bellows. The laser beam propagates via the mirror, lens, viewport and is then incident on the target (not shown) inside the chamber.

different positions. Various lenses were used in the ablation studies, with focal lengths of 30.0 cm, 40.0 cm, and 59.5 cm. The 30.0 cm and 40.0 cm lenses were Newport BK7 plano-convex lenses with damage thresholds of 2 J/cm^2, while the 59.5 cm lens was a CVI Laser BK7 plano-convex lens with a damage threshold of 10 J/cm^2. Several lenses were necessary to focus the laser onto the movable ablation target over a 30 cm range. Next, the beam encountered a 34 mm (1 1/3 inch) conflat window with a 16 mm (0.63 inch) inner diameter. These optics were situated in a safety containment box (Appendix C) to enclose the laser light; the assembly is shown in Figure 4.9.

The target was mounted on a movable bellows system designed and fabricated at the NSCL. The bellows made it possible to move the target under vacuum to different positions within the 21-ring-electrode system from Ring 8 (closest to the entrance window) to Ring 20. The movable target position system thus allowed studies of the laser ablation process and ion transport at different positions.

Lissajous Raster Scan System

When a high-power laser is incident on the same spot on a target, continuous operation will drill into the surface. The drilling changes the ablation characteristics, which change with target depth [74, 75]. In addition, non-uniformities occur after crater formation from drilling. A common solution to this problem is to rotate the ablation target itself [76]. Another solution is to change the laser position. A system to reduce drilling was not included initially due to the mechanical constraints. However, it became apparent that the drilling was a serious problem reducing the ion intensity. To eliminate this problem, the lower mirror was raster scanned, rather than modifying the support hardware.

The raster scan system moved the lower mirror in an adjustable pattern to ensure the beam spot moved continuously. All components of the system were purchased from Newport. A looped raster scan program was written and uploaded into an ESP300 controller, which operated two Newport CMA12CCL actuators connected to a U100 - A Ultima kinematic mount. The minimum step of the actuators was 0.2 μm, which corresponds to a mirror angle of 1.1 arcsec or 3×10^{-4} degrees.

The range of motion needed by the motorized actuators in this system was determined with an optical ray tracer program, Beam Three (Stellar Software). The optics and the dimensions of the system were put into Beam Three, and 68 rays starting from a 4.0 mm (0.158 inch) central portion of the lower mirror were tracked. The angle of the lower mirror was increased until the light was no longer incident on the target. Based on these calculations, the maximum angle of the lower mirror was 0.0795 degrees, moving the spot over a 3.4 mm diameter of the 5 mm actual target diameter. The entire target surface could not be covered by the raster scan system. The calculated values could then be implemented into the motion controller.

The actuators moved the mirror in a raster-scan motion approximately following a Lissajous figure (see Figure 4.10), which was chosen as the raster-scan pattern. A Lissajous function is sinusoidal and expressed by the parametric equations:

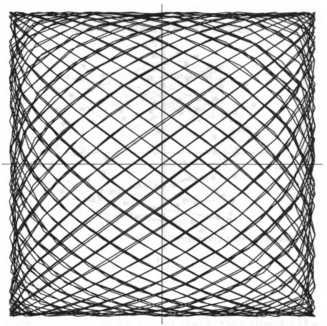

Figure 4.10: A generic Lissajous function with $a/b = 1$, $c/d = 0.5$, and $m/n = 0.72$.

$$x(t) = a\cos(nt + c) \tag{4.1}$$

and

$$y(t) = b\sin(mt + d), \tag{4.2}$$

where a and b are the amplitudes, n and m are the frequencies, and c and d represent the phases, in the x and y directions, respectively. For this ablation system, the values of a and b were based on the diameter of the target as determined by Beam Three. The actual pattern for this system is shown in Figure 4.11, which includes the mathematically determined values, and the manually adjusted points that were close to the border of the target. Rather than changing the function, the area was maximized by changing the coordinates of a few out-lying points, which were moved inside the estimated target diameter. In addition, the points near the corners of the pattern (Figure 4.10) were dropped to accommodate the circular geometry of the target.

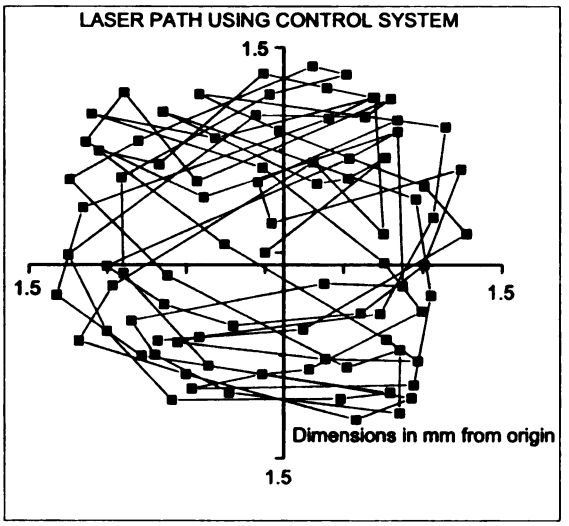

Figure 4.11: The path of the laser beam on the target due to the motion-controlled lower mirror. Each coordinate was programmed into the position controller attached to the mirror mount.

Using the maximum angles calculated in Beam Three and the Lissajous pattern, various stepping programs were written and tested. The final program used was looped, and the duration of each cycle was 34 s. The program contained 87 coordinate pairs, with a delay of 2 ms at each position. This resulted in an average of 8 pulses per coordinate position per 34 s cycle, assuming the laser was running at a repetition rate of 20 Hz. For the gas cell ablation tests at 0.5 Hz (Section 5.4.2), each target position was hit with less than 1 pulse on average. The program was tested whenever the target and optics were modified. The raster-scan system greatly reduced the negative effects due to target drilling.

Laser Beamspot Measurements

An important parameter to determine in laser ablation experiments is the laser fluence, which is expressed in energy per unit area. Various methods are used to determine the spot size, from measuring the diameter of the ablation crater, to using a CCD camera to image the spot, or using burn paper [58,77–79]. For this research, the

spot diameter was measured by observing burn paper marks using Zap-It^{TM} burnpaper. The spot size and profile were first measured at each optical component to check for any non-uniformities. The spot size was measured at the laser ablation target by placing the Zap-It^{TM} burnpaper at the approximate focal point of the lens. The RGA quadrupole tube was removed from the chamber (see Figure 4.2 for an overview schematic), and the rod with the burnpaper was inserted through the CF port. The laser beam properties can also be obtained using a few simple calculations. The beam diameter at the focus, d_0, can be approximated by [80]

$$d_0 \approx 2f^{\#}\lambda, \tag{4.3}$$

where λ is the wavelength of the laser and the f-number, or $f^{\#}$ is defined as

$$f^{\#} \equiv f/D, \tag{4.4}$$

where f is the focal length of the lens and D is the laser beam diameter (when the beam is incident on the lens). The laser beam diameter can be used to calculate the laser fluence, F, which is defined as

$$F = E/(\pi r^2), \tag{4.5}$$

where E is the laser energy in joules and r is the beam spot radius ($d_0/2$). The discussed values including the beamspot were measured in the present work. Since a beamsplitter (80% transmittance) was used in these measurements, the maximum energy of the laser is approximately 93 mJ, which was used for the fluence calculations, F_{max}. The laser energy values were obtained with the power meter. The calculated and measured values are summarized in Table 4.1 for the 59.5 cm lens used in this research. The calculated and measured values in Table 4.1 differ greatly. For instance, the calculated value for d_0 is approximately 12% of the measured value. The discrep-

Table 4.1: Beamspot calculations and measurements, see the text.

Variable	Calculated	Experimental
D	-	0.62 cm
$f\#$	95.967	-
d_0	0.010 cm	0.086 cm
area	8.17×10^{-5} cm^2	5.5×10^{-3} cm^2
F_{max}	1138 J/cm^2	17 J/cm^2

ancy between the calculations and measured values are due to a number of effects. First, the calculations assume perfect focus, no laser beam divergence, and an ideal Gaussian distribution of the spatial laser intensity. In addition, effects of the window are not taken into account, which may cause some degree of thermal lensing, producing larger measured values. The effects discussed contribute to the much smaller calculated values versus the measured values in Table 4.1.

Laser Alignment

The initial alignment of the optical path was performed with the N4 vault closed to other personnel and the laser safety system (Appendix C) overridden. Kentek Corp. safety goggles were used while the beamspot location at each of the first eight components was positioned using small targets with cross-hairs. Once the beam was aligned at the glass viewport entrance to the chamber, the vault was re-opened and a Spy Camera Bullet WBC-021 camera, with a L-16.0 lens, was used to align the beam on the target inside the chamber. A small magenta plexiglass piece was attached to the camera to act as a filter to prevent damage to the light sensitive pixels from the large amount of laser light. The angle of the upper mirror was adjusted to center the target. Once the beam was centered, the raster scan system could then be initiated. The optical alignment of the first eight elements was re-evaluated on a regular basis.

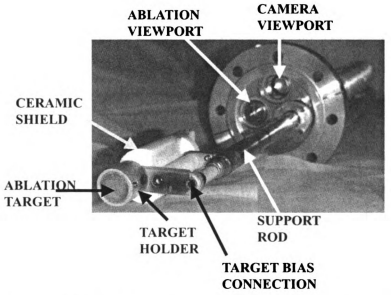

Figure 4.12: Photograph of the laser ablation target assembly, with various components labeled. The laser beam enters the viewport, travels through the ceramic shield and is incident on the target inside the holder, supported by a movable metal rod.

4.1.5 Laser Ablation Target Assembly

A laser ablation target assembly consisting of the ablation target, target holder, and support structure was designed and fabricated at the NSCL specifically for ablation studies. This entire assembly had to fit inside the drift ring structure in the vacuum chamber. The target was mounted on a movable rod on a conflat flange and an electrical bias could be applied to the target. An overview picture is shown in Figure 4.12.

Target Materials

A variety of materials were chosen for the ablation studies: carbon, aluminum, iron, zinc, copper, silver, and gold. These targets cover a mass range of 12 amu to 197 amu. The isotopic abundances of these elements are shown in Table 4.2, and selected macroscopic properties are given in Table 4.3. The main motivation for choosing the aluminum, iron, copper, and gold was the relative ease to obtain and machine the target. An indium target was also used for ablation, yet no signal was detected, most likely

due to its rapid destruction given its low melting point (430 K). Zinc and silver were selected to extend the number of targets available for LEBIT laser ablation studies, which will be discussed in Chapter 5. Since there is such a large difference in mass between gold and the other targets, silver was used to provide an intermediate mass.

On the other hand, a variety of factors contributed to the choice of carbon as an ablation target. The main motivation was that carbon is an excellent mass reference [5, 81] since its mass is known exactly, which is particularly applicable for LEBIT calibrations. In addition, the laser ablation of carbon has been studied extensively [5, 48, 81–83].

A glassy or vitreous carbon pellet was used in the present work. The trade name of this glassy carbon target is Sigradur^{TM}, which is manufactured by Hochtemperatur-Werkstoffe GmbH (HTW). Sigradur^{TM} is similar to graphite, but has an amorphous structure, which makes it less vulnerable to oxidation and corrosive materials. The structure of this glassy, or vitreous carbon can be described as a network composed of graphite-like bands containing a large amount of micropores [84]. This structure explains its low density (1.42 g/cm3) relative to graphite (2.27 g/cm3) [85]. In addition, the average bond angles of glassy carbon are roughly 117 degrees, while graphite contains bond angles of 120 degrees. Vitreous carbon also contains non-hexagonal rings. There are two types of Sigradur^{TM}: G and K, differing mainly in the temperature at which they splinter, 3000^{o} C and 1000^{o} C, and their densities, 1.42 g/cm^3 and 1.54 g/cm^3, respectively. For this research, Sigradur^{TM} G was chosen as the target due to its greater physical stability under high temperatures.

Target Holder

Two target holders and targets were used for laser ablation experiments, as shown in Figure 4.13. Both target holders, made of aluminum, were designed and fabricated at the NSCL. During ablation measurements, the aluminum mass peak was monitored with the RGA to determine whether the target holder was also being ablated. The

Table 4.2: Target isotopic abundances

Target	Isotopic Abundance
Sigradur-G	12 (98.89%), 13 (1.11%)
Al	27 (100%)
Fe	54 (5.85%), 56 (91.75%), 57 (2.12%), 58 (0.28%)
Cu	63 (69.17%), 65 (30.83%)
Zn	64 (48.60%), 66 (27.90%), 67 (4.10%), 68 (18.8%), 70 (0.60%)
Ag	107 (51.84%), 109 (48.16%)
Au	197 (100%)

Table 4.3: Target property comparison, where T_m is the melting point and T_b is the boiling point.

Target	M.W. (amu)	Density (g/cm^3)	T_m(K)	T_b(K)
Sigradur-G	12	1.42	3800	4300
Al	27	2.7	933	2329
Fe	56	7.87	1808	3273
Cu	64	8.96	1356	2840
Zn	65	7.03	693	1180
Ag	108	10.49	1234	2485
Au	197	19.32	1337	2340

first target holder, Holder A, was relatively small, with a side exit hole for the ablation products. However, the disadvantage of this holder is the flat surface of the target that resulted in back-reflection of the laser light. At one point, the laser reflected back to the viewport, heating the glass and destroying the welded seal to the glass. Therefore, an angled target surface was used in further tests in vacuum. Holder B was designed to support a target with an angled surface and contain it in an enclosed volume, as shown in Figure 4.14a. The purpose of the enclosed volume was to internally reflect any stray laser light, and in addition, prevent the ablation products from coating the nearby ring electrodes and chamber walls. However, the larger target was not practical under gaseous conditions. As already discussed in Section 2.4.3, the length of the ablation plume changes with pressure, in addition to laser energy, laser pulse length, plume geometry and plume velocity. Thus, Holder A was used during ablation experiments in the presence of a buffer gas. The exit hole on Holder B was enlarged

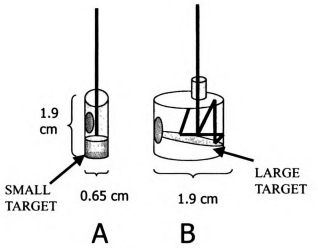

Figure 4.13: Schematic view of (A) the small target and target holder, which resulted in back-reflection, but was better-suited for gaseous conditions and (B) the larger target holder, with an enclosed chamber to prevent back-reflection, but was too large for the plume to efficiently escape in the presence of a background gas.

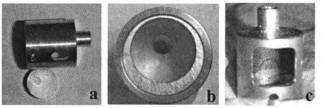

Figure 4.14: Photographs of (a) an ablated Ag target with Holder B, (b) the added collar to hold the Ag and Zn targets (no target present), and (c) the opening of Holder B that was modified to make it larger for more of the plume to escape.

as seen in Figure 4.14c to maximize the amount of ablated products that could exit the holder.

Other components were added to optimize the ablation conditions. The large ceramic piece seen in Figures 4.12 and 4.15 was constructed after running the ablation experiment with a buffer gas. The first ablation in the gas cell (Chapter 5) using an Fe target resulted in many small metal fibers. The ceramic shield seen in Figure 4.15B was designed to catch some of the ablated fibrous substance and to prevent the material from coating the insulators, the ring electrodes and other gas cell components. As a side note, the fibrous material in Figure 4.15 was from a carbon target.

The target holder assembly was positively biased externally by a SRS high voltage

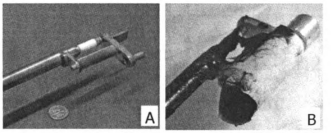

Figure 4.15: Photographs of (A) the ablation target assembly with the small target holder, Holder A. (B) The assembly with the larger target holder, Holder B. The large ceramic piece was added to collect some of the fibrous material ablated from a carbon target, which is the black material seen coating this piece.

power supply in order to force the positive ions away from the holder. The target bias was applied from outside the chamber on an insulated wire. A ceramic rod insulates the wire within the metal support rod.

Ablation Targets

All of the targets were solid metal pieces, except the gold target. The dimensions and geometry of the targets are provided in Figure 4.16. The gold target was made by layering approximately 12 thin foils to create a 3 mm thick target that could withstand the ablation process. After the gold layers were compressed with a vice, the piece was glued to a previously ablated copper target so that the assembly could be mounted in the holder. As a side note, the copper mass signal was monitored during the gold ablation trials to ensure that a hole was not drilled through the gold target. The 12.7 mm diameter zinc and 12.5 mm diameter Premion^{TM} silver materials were obtained from Alfa Aesar. The purity of these targets was 99.9% and 99.9985%, respectively. The diameter of the zinc and silver targets was smaller than the other targets so a collar was designed and fabricated, as shown in Figure 4.14. The Sigradur^{TM} was machined by HTW.

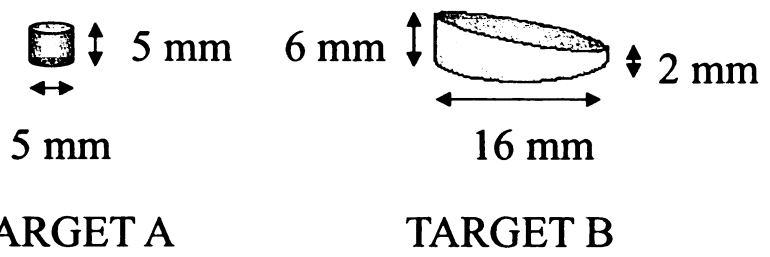

Figure 4.16: Schematic view of the targets A and B with dimensions in mm.

4.2 RGA Operation and Modifications

The masses of the ablated ions were measured in the vacuum ablation studies with a modified residual gas analyzer. The SRS Residual Gas Analyzer (RGA) 300 operates using the same principles as quadrupole mass spectrometry. The device is relatively compact, easy to transfer between systems, and is relatively simple to use. The residual gas analyzer's backbone is a quadrupole mass filter, which separates species based on mass-to-charge ratios. This filter is composed of four rods, which are 0.64 cm in diameter and 11.4 cm in length. A combination of DC and RF voltages are applied to these rods, as shown in Figure 4.17. The RF and DC amplitudes are varied and only those ions with stable trajectories are transmitted through the center of the device. The potentials applied to the rods are given by

$$V_{x/y} = +/- (U + V_0 \cos \omega t), \tag{4.6}$$

where U is the magnitude of the DC voltage on either set of rods, V_0 is the RF voltage amplitude applied to either rod set, and ω is the angular frequency of the RF voltage. The combination of the sinusoidal RF and negative (or positive) DC voltages is applied to one set of rods. The sinusoidal RF field is 180 degrees out of phase from that on the other set of rods. The RF to DC ratio determines the transmitted masses, while the DC to RF ratio determines the filter selectivity. By adjusting the DC/RF ratio, the mass selectivity can be optimized, while tuning to a specific mass using the

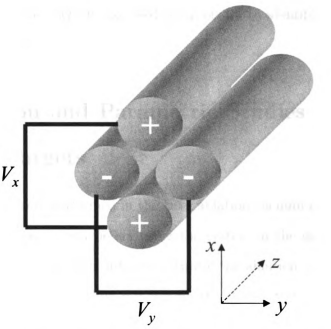

Figure 4.17: A sketch of the quadrupole design and operation of the RGA.

RF/DC ratio.

The ion current was measured in either a Faraday cup or a multi-channel continuous dynode electron multiplier (CDEM). The CDEM had a greater sensitivity, better signal to noise, and faster scan rates than the default Faraday Cup. The CDEM is a straight, four channel tube of glass, which is conical on one end and negatively biased relative to the back end. The principle of operation of the CDEM is similar to a photomultiplier tube. The cations strike a metal cathode, and electrons are liberated, these electrons cascade down the tube creating more electrons via an avalanche process. The anode plate of the CDEM collects these electrons.

The usual use of residual gas analysis is the detection of neutral molecules. These molecules are ionized and dissociate in the acceleration section of the RGA and are then selected by the rods and detected by the Faraday cup. In order to detect incident particles that are already ionized, a few modifications to the RGA were necessary, including bypassing the filament, which ionizes neutral species. A slide switch was added to block the current for "ion detection mode." Flipping the switch back allows

"neutral detection mode," which was used occasionally to identify possible vacuum contaminants and leaks.

4.3 Detection and Parametric Studies of the Ablation Targets

Various experiments were performed in the laser ablation vacuum chamber to understand the laser ablation system before using the system in the gas cell. With each target, parameters were varied in order to optimize the ablation yield. The detected ion intensity was maximized, while minimizing the destruction of the target. The parameters that were investigated included the potential gradient, the bias on the target, the target position, the laser energy or fluence, and the reproducibility of the data. During each test, all parameters were kept fixed except for the parameter being studied, as usual.

4.3.1 Mass Scan Studies

Prior to changing parameters and optimizing the ablation conditions, the mass spectrum in the range of $1 \leq A \leq 300$ was obtained during the ablation of each target to identify the ablated species. The laser energy was increased until the desired ions were detected, which gave an approximate value of the threshold laser fluence for ablation, and will be discussed further in Section 4.3.4. RGA parameters included the units (amps) and mass range, in addition to the mass-scan speed determining the noise floor. The parameters during the initial work are shown in Table 4.4, where the number of scans is given, the target position is the ring number where the target was located, V_R is the potential gradient on the ring electrodes (V/cm) and V_t is the voltage applied to the ablation target.

For each panel in Figure 4.18, mass peaks are present below 10 m/z, which are

Table 4.4: Parameters during mass scan experiments, where LF is the laser fluence and TP is the ring number where the target is located.

Target	Scans	LF (J/cm^2)	TP	V_R (V/cm)	V_t (V)
Cu	3	2.6	15	1.96	26
Al	10	18.0	14	2.34	32
Au	1	1.9	15	1.59	21
Fe	2	4.7	15	1.96	26
Ag	3	0.6	15	1.96	26
Zn	4	0.4	15	1.96	26
C	9	1.2	15	0	0

artifacts. At 10 amu, the applied electric field in the RGA is too small to stop energetic ions from passing through the quadrupole and being collected.

As the laser fluence was increased, the presence of 2^+ ions was detected, similar to other results [58]. Figure 4.19 demonstrates the effect of increasing the laser fluence on the mass scan for silver and zinc. Figure 4.20 shows similar three-dimensional data for silver, but in a different presentation. The intensity of all peaks increased with increasing laser fluence. In addition, with increasing fluence, the peak at m/z 27 also increased, which corresponds to aluminum. The target holder is composed of aluminum, and as the laser power increased, stray laser light ablated the holder. Peaks appear at m/z 107 and 109 at higher laser fluences with the zinc target that are due to the presence of silver in the target holder. Prior to the zinc experiment, silver was ablated, and the target holder interior became silver-plated; this silver coating was also ablated at higher fluences by stray laser light.

4.3.2 Isotopic Abundances

Laser ablation is often used to determine the material composition, or even to determine the abundance of specific astrophysical s-process elements in meteorites [86]. The isotopic abundance of the ablated targets was also readily obtained from the present data. Determining the isotopic abundances of the targets is useful for confirming the target composition prior to using the ablation products as mass references

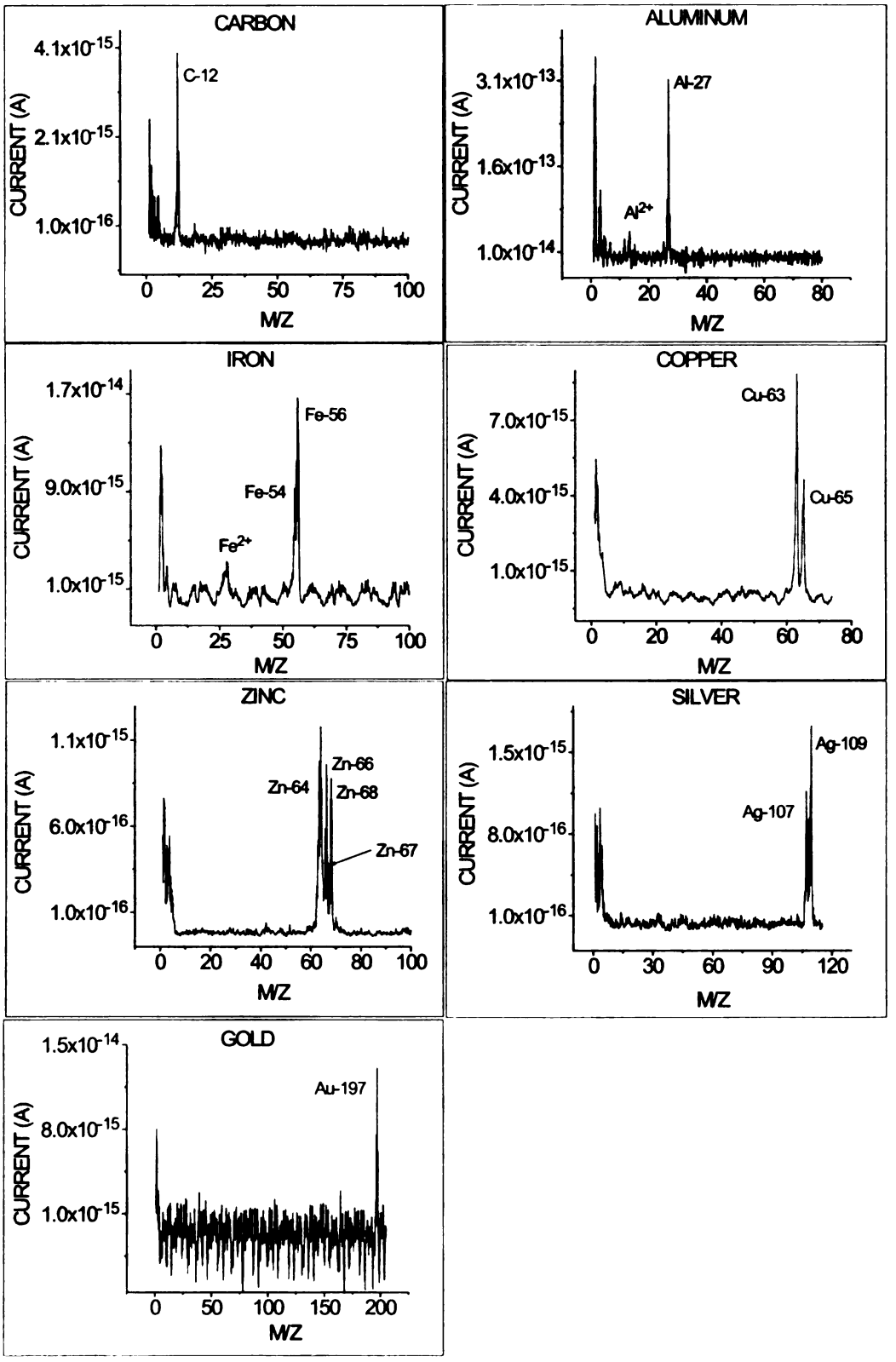

Figure 4.18: Average mass spectrum for each ablation target is shown.

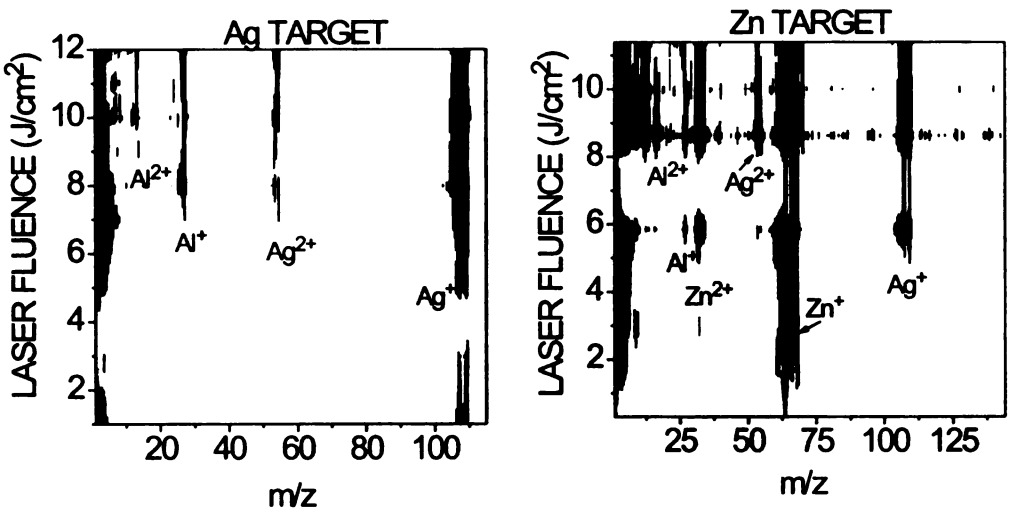

Figure 4.19: Contour plots showing the mass spectra as a function of laser fluence, see the text for explanation.

in LEBIT. In addition, it is useful to measure the isotopic abundances in order to test the sensitivity of the RGA. From the data taken in the P vs. T mode (described below) of the RGA, the abundances during each run were obtained and averaged, and the results are shown in Figure 4.21. (Since aluminum and gold have one naturally occurring isotope, they are omitted from this data.) For copper and silver, the relative abundances are fairly evenly distributed among the isotopes. The experimental isotopic abundances are very close to the natural abundances. However, for the iron and zinc data, the experimental isotopic abundances do not agree completely with the literature values. This is mostly due to the isotopes with less than two percent abundance, which were not always accurately detected by the RGA since the intensity was at the threshold/ noise level of the RGA. This in turn affected the relative abundances of the other isotopes. In general, however, the data agree fairly well with the known abundances and indicates that the system is sensitive down to the level of a few percent.

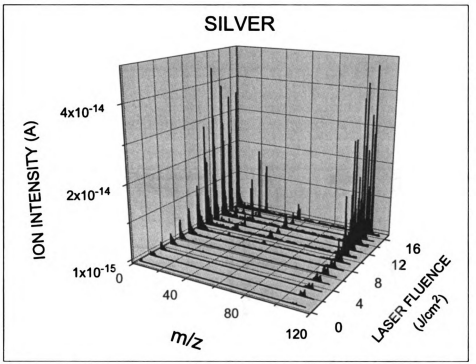

Figure 4.20: Silver mass spectrum as a function of laser fluence.

4.3.3 Data Acquisition and Analysis

The pressure versus time (P vs. T) mode of the RGA was utilized to study the yield as a function of various parameters. Rather than pressure, the current (A) was recorded. The P vs. T mode made it possible to gate on individual mass-to-charge ratios rather than scanning the entire mass range. The RGA records the partial pressures for each mass individually. In this mode, the number of selected masses determines the noise level. Data were acquired over a two minute time period. The peaks for each individual isotope were monitored, in addition to monitoring the 2^+ peak of the most abundant isotope, possible cluster peaks, the aluminum peak, and several background masses up to a maximum of eight peaks. Therefore, an effort was made to only select the most important peaks. The background peak was chosen among masses not present in the spectrum. To ensure that the background was independent of mass choice, gold

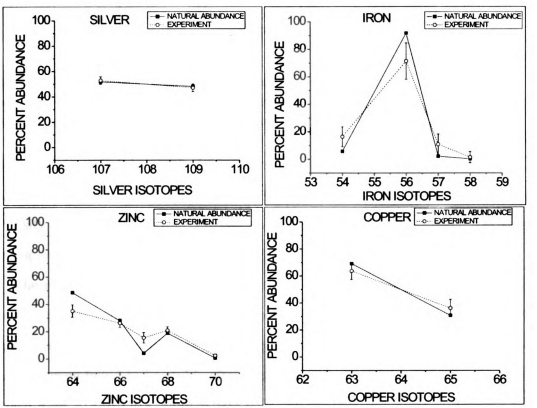

Figure 4.21: The measured isotopic abundances from this research compared to the literature values. Lines are drawn to guide the eye.

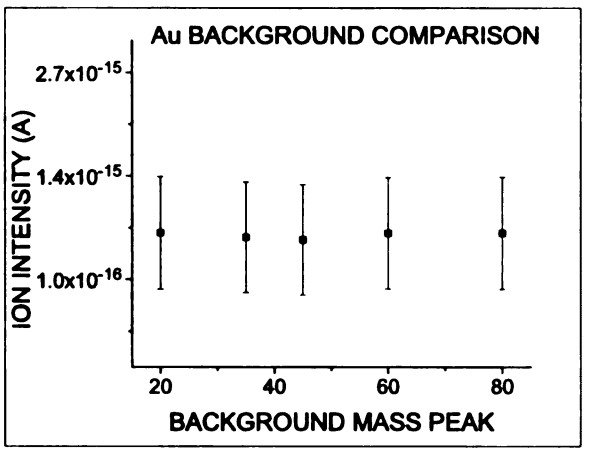

Figure 4.22: The effect of changing the mass of the background measurement. The data were taken for the ablation of a gold target with a laser fluence of 4.3 J/cm^2. No significant change is seen between different background peaks.

ablation data were taken with the background sampled at varying masses, shown in Figure 4.22. The ablation of a gold target at 4.3 J/cm^2 clearly shows that the ion intensity at various background masses is constant. The background was measured during every trial.

The ion current was found to vary depending on laser operation, time of irradiation, mirror control program, target properties, etc. Thus, a procedure to give reproducible measurements was necessary. After the RGA and laser were initiated, the data were found to be stable after approximately 30 s. The values were thus averaged from 30 s to 120 s. Sample data from the ablation of a zinc target with a laser fluence of 0.5 J/cm^2 are shown in Figure 4.23. The distribution of the data points is shown in Figure 4.24. Outlying data points in a scan were removed if they were more than 3σ from the mean, such as for the Zn-68 data shown in Figure 4.24. However, less than 1% of the data points were removed from the entire data collection. There was a large amount of fluctuation in a typical RGA scan, as can be seen with the sample zinc data. The fluctuation in this data was most likely due to the chaotic environment involving the rapidly changing plasma, in addition to the scanning laser

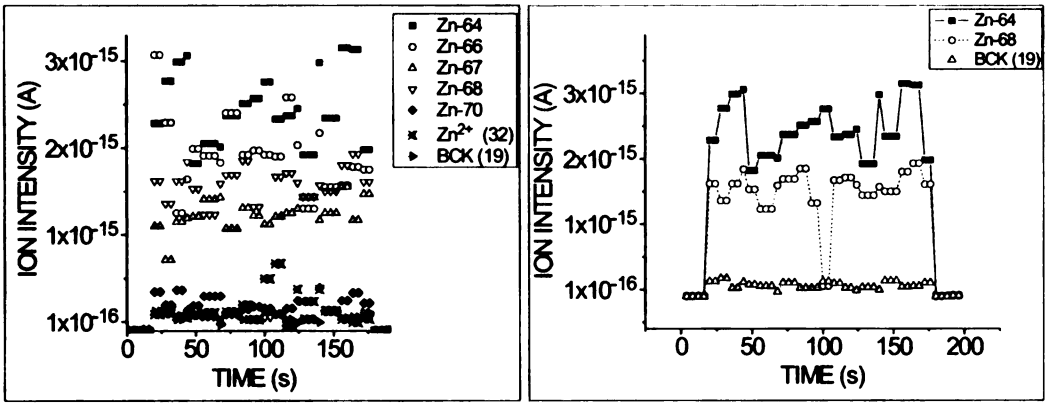

Figure 4.23: (Left) Raw data from the ablation of a zinc target with laser fluence 0.5 J/cm^2. (Right) Part of the data from the same data set. The Zn-68 demonstrates 2 data points, which were removed according to the criteria discussed.

beam. In addition, the signal would fluctuate more as the target degraded (which was minimized with the raster scan system). The total ion intensity for a given target during a 90 s scan was obtained by summing the average recorded currents for each isotope. The error in each measurement resulted from the standard deviation in the recorded current of each isotope, in addition to the standard deviation of the background current, which were added in quadrature.

4.3.4 Metal Targets in Vacuum

The discussion of the parameter studies is divided into the metal targets and the Sigradur^{TM} target, due to the very different properties of the carbon target. This section is divided into parts for each parametric study.

Potential Gradient

The effect of changing the potential gradient applied to the drift rings on the ablation yield was determined. Since the potential is created using a resistor chain, the voltage was changed on the first ring. The target bias was also changed in order to match the bias of the ring at the target's position. Additional parameters held constant

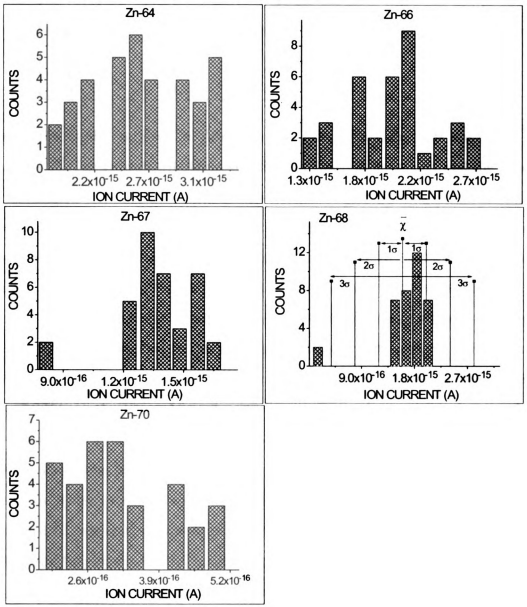

Figure 4.24: The distribution of the zinc data from Figure 4.23. The histograms illustrate the fluctuation of the data by binning the number of points from Figure 4.23 in specific current ranges. Data points were only removed if they were more than 3σ from the mean, as in the case of the Zn-68 data where two outlying points were removed.

Table 4.5: Ablation parameters during potential gradient experiments.

Target	Laser Fluence (J/cm^2)	Target Position (Ring Number)
Cu	5.8	15
Al	5.8	14
Au	10.3	15
Fe	11.0	15
Ag	1.1	15
Zn	1.2	15

during this study are given in Table 4.5. The data from these tests are shown in Figure 4.25. The yield distributions were fit with Gaussian functions, and the values of the centroids are illustrated in Figure 4.26. The weighted average of the centroid was found to be 1.73 $\pm$ 0.15 V/cm for all of the targets. For some of the data, including the gold and iron targets, the error bars are so large (due to the large fluctuations during data acquisition) that it is difficult to see a change in the ion intensity with changing potential gradient. In general, the ion intensity decreased when either a high or low voltage was applied to the first ring, creating a fairly steep or flat gradient, respectively. When a steep gradient was created with a high voltage on the first ring (e.g. 7.8 V/cm), the detected ion intensity decreased since the ions were accelerated to the point of not being detected by the RGA. On the other hand, low (e.g. 0.2 V/cm), zero and negative (e.g. -2.6 V/cm) gradients did not effectively guide the ions to the RGA. These results generally agreed with the SIMION calculations discussed in Section 3.1.1, where an intermediate potential gradient on the rings was more efficient in transporting ions to the RGA. For instance, in SIMION, a gradient of 2.1 V/cm was more effective in transporting ions than either 13.0 V/cm or 0.1 V/cm, similar to the results of this experiment that demonstrate the optimum potential gradient to be 1.73 $\pm$ 0.15 V/cm.

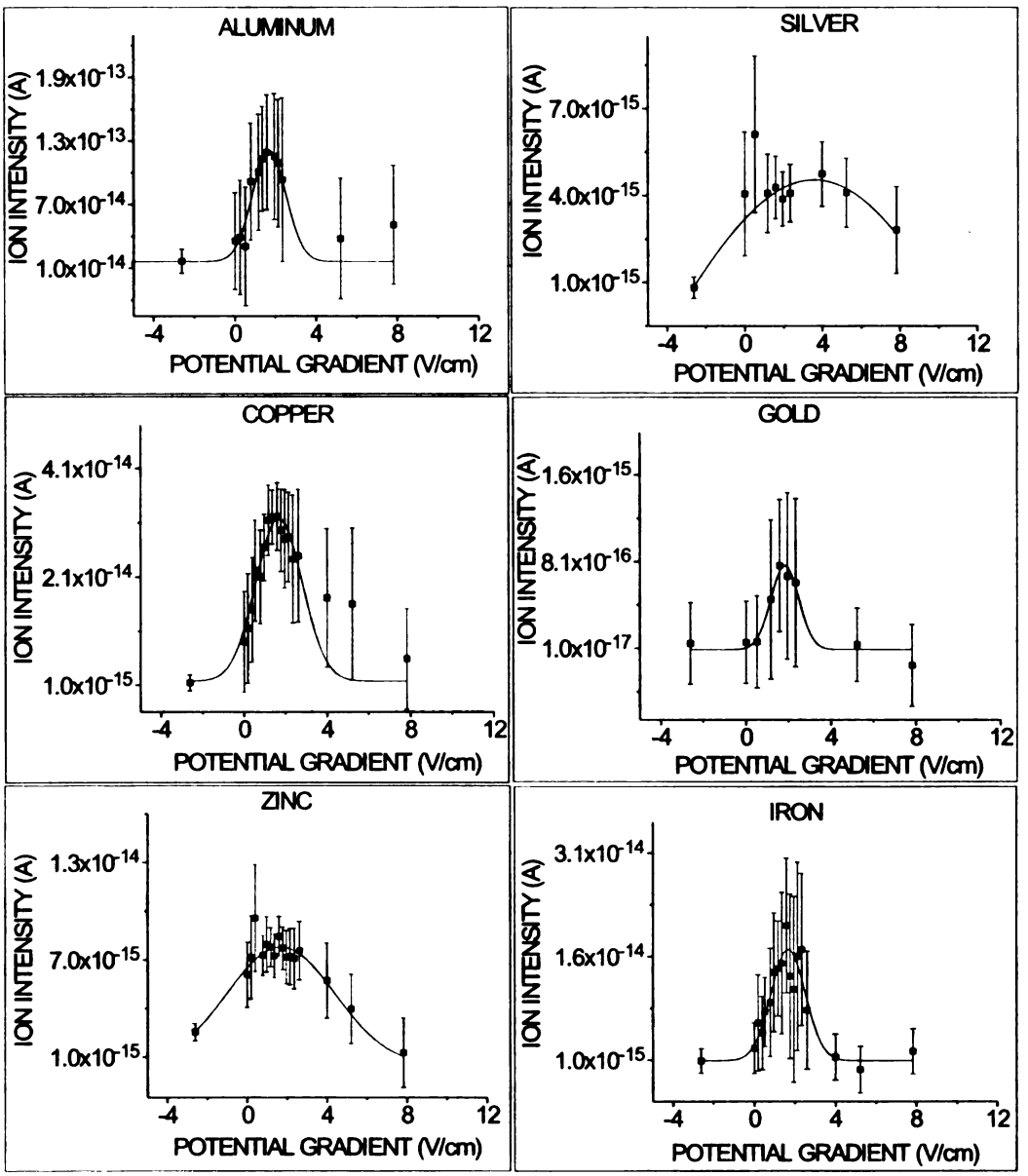

Figure 4.25: The detected ion intensity as a function of potential gradient for each metal ablation target. The peaks were fit with Gaussian functions.

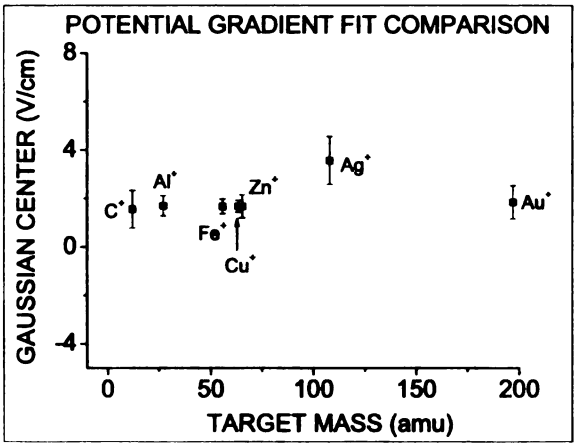

Figure 4.26: The centroid of the Gaussian function fitted to the data from the study of the effect of the potential gradient on the ablation yield.

Table 4.6: Ablation parameters during target bias experiments.

Target	Laser Fluence (J/cm^2)	Target Position (Ring)	V_R (V/cm)
Cu	3.8	15	1.96
Al	6.0	14	2.40
Au	2.6	15	1.96
Fe	2.2	15	1.96
Ag	1.1	15	1.96
Zn	1.1	15	1.96

Target Bias

The bias on the target was also varied, while keeping the potential gradient fixed. The parameters for the target bias experiments are summarized in Table 4.6. The data are shown in Figure 4.27. According to the calculation with SIMION, shown in Figures 3.4 and 3.5, the ion transport to the RGA should be very sensitive to the voltage on the target. However, in general, the data from these experiments demonstrate the target bias has little effect on the ion intensity detected. The ring electrodes appear to have more impact on the ablation yield than the target bias.

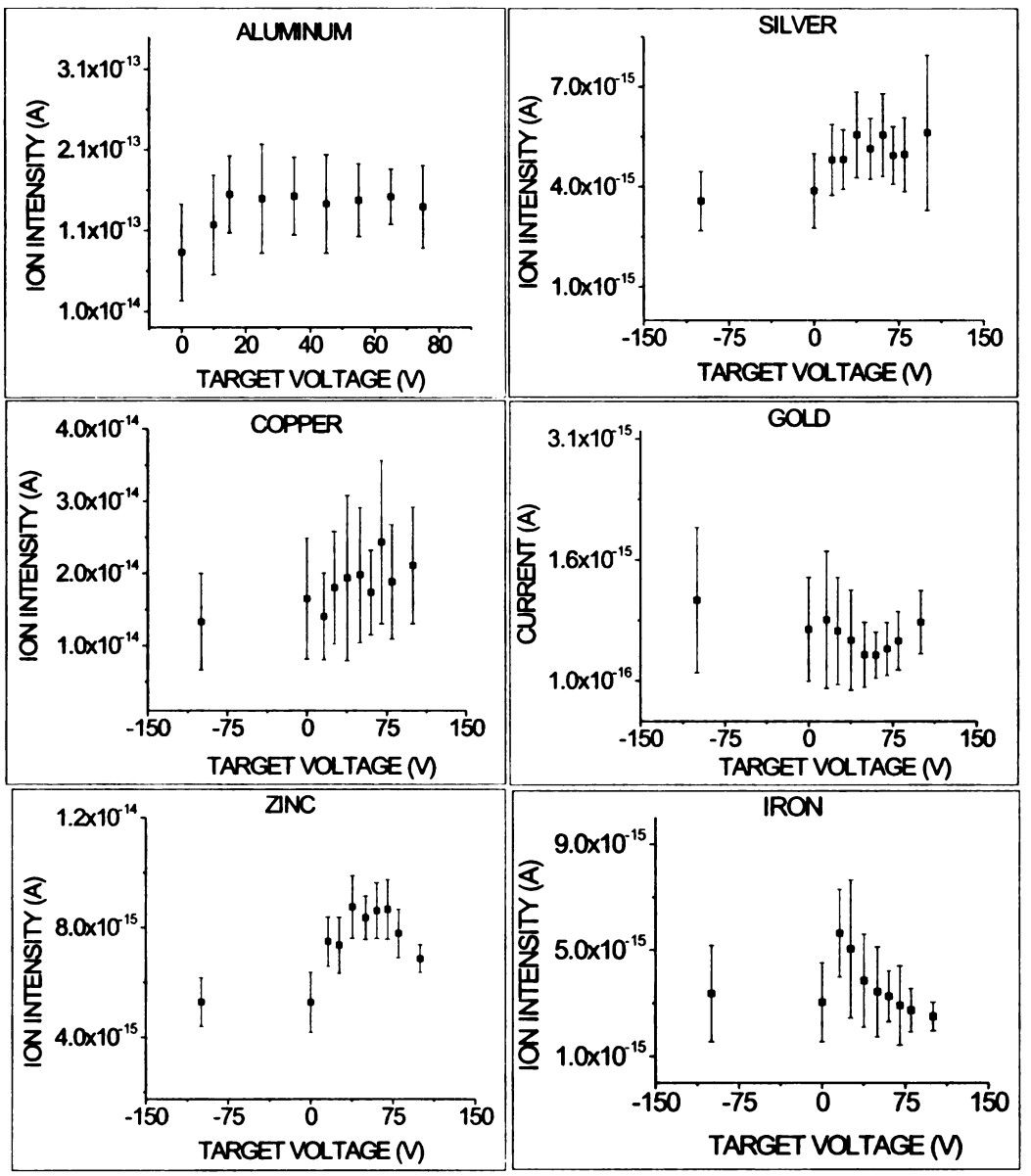

Figure 4.27: The detected ion intensity as a function of target voltage for each metal ablation target. The target voltage does not have a large effect on the detected ion intensity.

Table 4.7: Ablation parameters during target location experiments.

Target	Laser Fluence (J/cm^2)	V_R (V/cm)
Cu	3.8	1.96
Al	5.8	2.34
Au	3.9	1.59
Fe	2.2	1.96
Ag	1.1	1.96
Zn	1.1	1.96

Laser Ablation Target Position

The position of the target relative to the rings was also varied to determine whether the location of the ablation affected the collection. When the position was changed, the target bias and the lens position were also changed to keep the other parameters constant. The ablation parameters during the target position study are shown in Table 4.7. As expected for the ablation under vacuum conditions, there is not a large effect on the data due to the target position, as shown in Figure 4.28. The drift ring system thus seems to efficiently transport the ions to the end. The intensity increases slightly in the vicinity of the RGA, or near the rings furthest from the window. This increase could be due to electronic noise created by the close proximity of the laser to the RGA quadrupole tube or a more efficient capture of ions close to the RGA.

Laser Fluence

The effect of the laser fluence on the target was studied. The laser fluence was adjusted by initially changing the delay between the flashlamp and Q-switch firing. The optimum value was found to be 180 μs; deviation from this value decreased the energy output of the laser, as shown in Figure 4.29. This delay could be changed to decrease the laser energy, but only to a point before the beam quality would degrade. The shot-to-shot stability decreased when the delay was greater than 250 μs and the pulse duration increased from 4 ns to 6 ns at a delay of 300 μs [87]. In order to minimize the degradation of the laser profile caused by adjusting this delay, the laser energy could

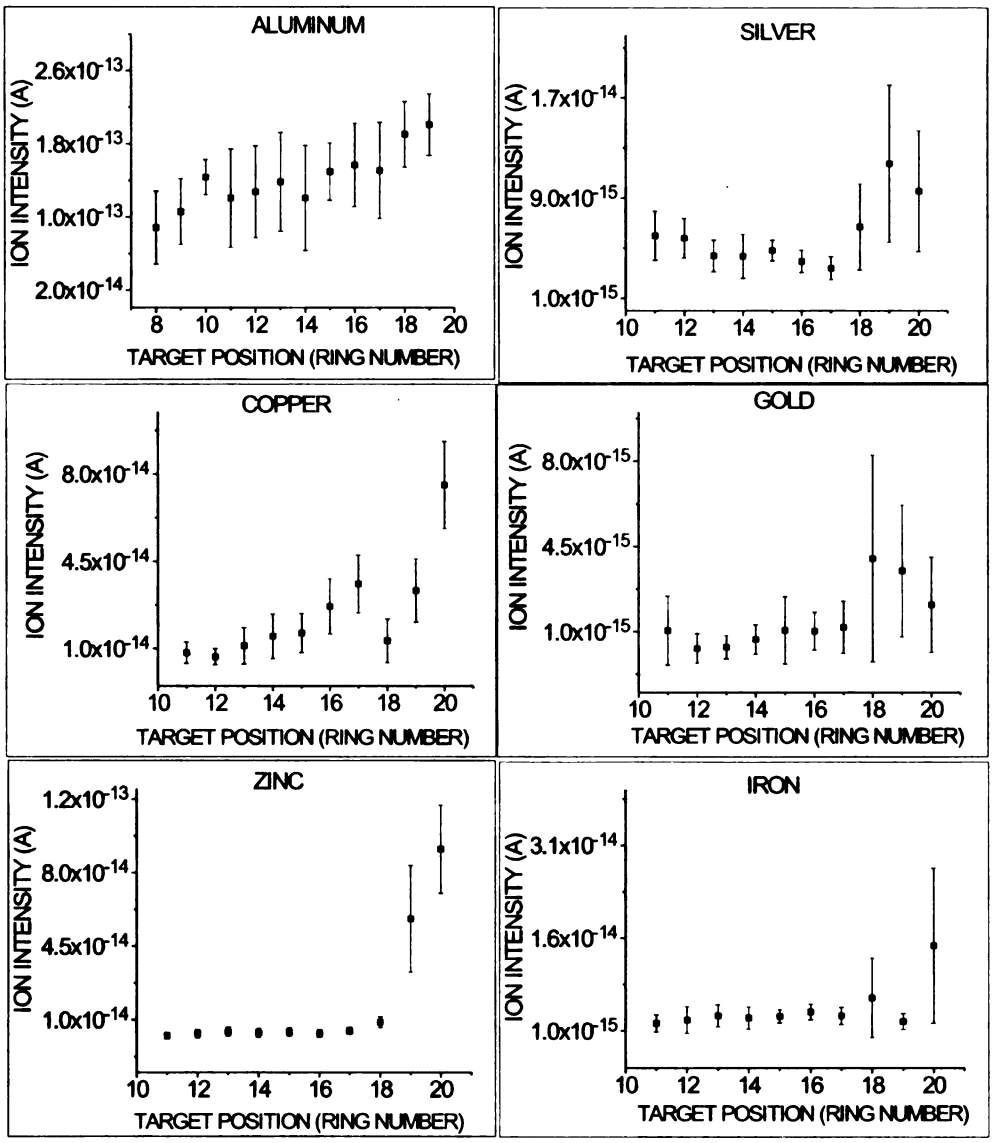

Figure 4.28: The detected ion intensity as a function of target position for each metal ablation target. There is not a large effect, although there is a general increase when the ablation target is at Ring 20, closest to the RGA.

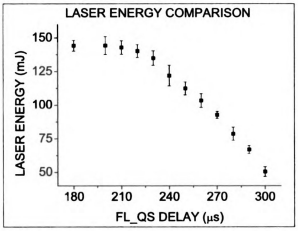

Figure 4.29: The laser energy as a function of the delay between the flashlamp and Q-switch. The default, optimum value is 180 μs; deviation from this value causes the energy to decrease.

also be adjusted by the combination of a halfwave plate and optical isolator. The laser energy reaching the target was controlled by adjusting the angle or position of the optics with a rotary mount; calibration plots are shown in Figure 4.30. These data were taken using the 80/20 beamsplitter, for the calibration of the half waveplate (HWP), the angle of the optical isolator (OI) was 0 degrees, while the angle of the HWP was 95 degrees for the calibration of the OI. The solid line is a $\sin 2\theta$ function. When the energy is at the maximum value, the light is optimized for circular polarization.

Ion Intensity as a Function of Laser Fluence

For the laser fluence experiments, the laser energy was monitored with the power meter; the ablation parameters are given in Table 4.8. The data were fitted with a weighted fit in ORIGIN from OriginLab Corporation with the so-called Hill function (similar to a Michaelis-Menten equation common in enzyme kinetics):

$$y = \frac{I_{max} x^n}{k^n + x^n}, \tag{4.7}$$

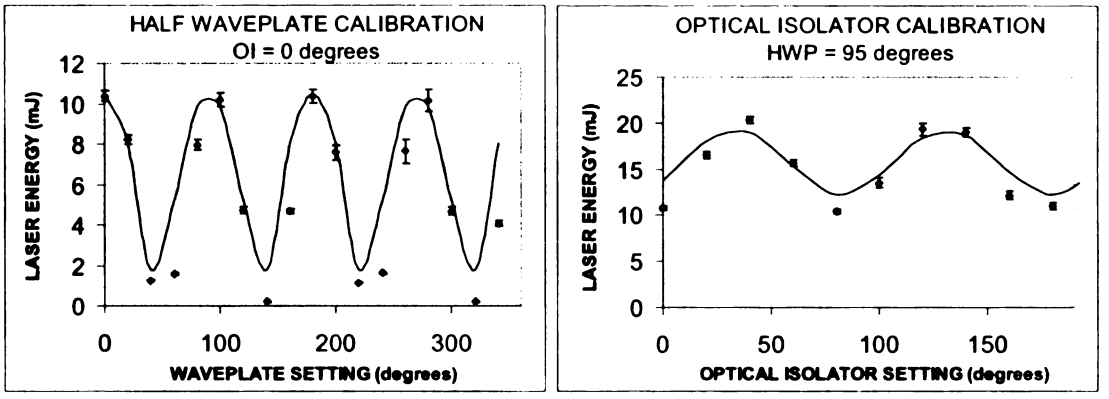

Figure 4.30: The calibration of the half waveplate (HWP) and optical isolator (OI) using an 80/20 beamsplitter. The solid line is a $\sin 2\theta$ function, multiplied by a factor for viewing. The laser energy is given at the power meter. For the HWP calibration, the angle of the OI was 0 degrees, and for the OI calibration, the angle of the HWP was 95 degrees.

where I_{max} is maximum value of the data, and k and n determine the slope. In addition, the data were also fitted in ORIGIN with the so-called Sigmoidal Richards (SRICHARDS) equation:

$$y = \begin{cases} \left(a^{1-d} + \exp[-b(x - x_c)]\right)^{1/(1-d)} & \text{for } d < 1 \\ \left(a^{1-d} - \exp[-b(x - x_c)]\right)^{1/(1-d)} & \text{for } d > 1 \end{cases} \tag{4.8}$$

In the SRICHARDS equation, a is the maximum value of the data, x_c determines the offset, while b and d affect the shape. The data and fitted functions using both the HILL and SRICHARDS equations are shown in Figure 4.31, while the fit parameters obtained in ORIGIN are given in Tables 4.9 and 4.10, respectively. The fits are almost identical, except for the fit to the data at the lower fluences, which will be important in determining the threshold fluence for ablation (discussed below).

The detected ion intensity increased with increasing laser fluence until a saturation point was reached. The saturation plateau occurred with all of the targets, including Sigradur^{TM} (Section 4.3.6). The saturation behavior has also been noticed in other ablation work [59–61] and results from plasma shielding, as discussed in Section 2.3.1. As mentioned, plasma shielding results from free electrons created during the leading

Table 4.8: Ablation parameters during laser fluence experiments.

Target	Target Position	V_R (V/cm)	V_t (V)
Cu	15	1.96	26
Al	14	2.34	32
Fe	15	1.96	26
Ag	15	1.96	26
Zn	15	1.96	26
Au	15	1.77	28

Table 4.9: Fit parameters for the laser fluence data using the HILL equation, Eqn. 4.7.

Target	I_{max}	k	n
Al	2.00×10^{-13}	4.22	4.13
Cu	7.61×10^{-14}	5.89	5.19
Fe	4.90×10^{-14}	6.72	5.96
Ag	6.77×10^{-14}	4.37	4.07
Zn	7.52×10^{-14}	3.22	15.1
Au	1.62×10^{-15}	2.07	3.42
Sigradur	2.23×10^{-14}	3.05	4.46

Table 4.10: Fit parameters for the laser fluence data using the SRICHARDS equation, Eqn. 4.8.

Target	a	x_c	d	b
Al	1.99×10^{-13}	-9.73	0.80	0.57
Cu	7.41×10^{-14}	43.7	2.22	0.98
Fe	4.79×10^{-14}	51.8	2.46	1.01
Ag	6.61×10^{-14}	51.1	2.64	1.09
Zn	7.52×10^{-14}	28.4	21.6	25.3
Au	1.61×10^{-15}	58.3	3.16	1.36
Sigradur	2.23×10^{-14}	7.56	1.21	1.04

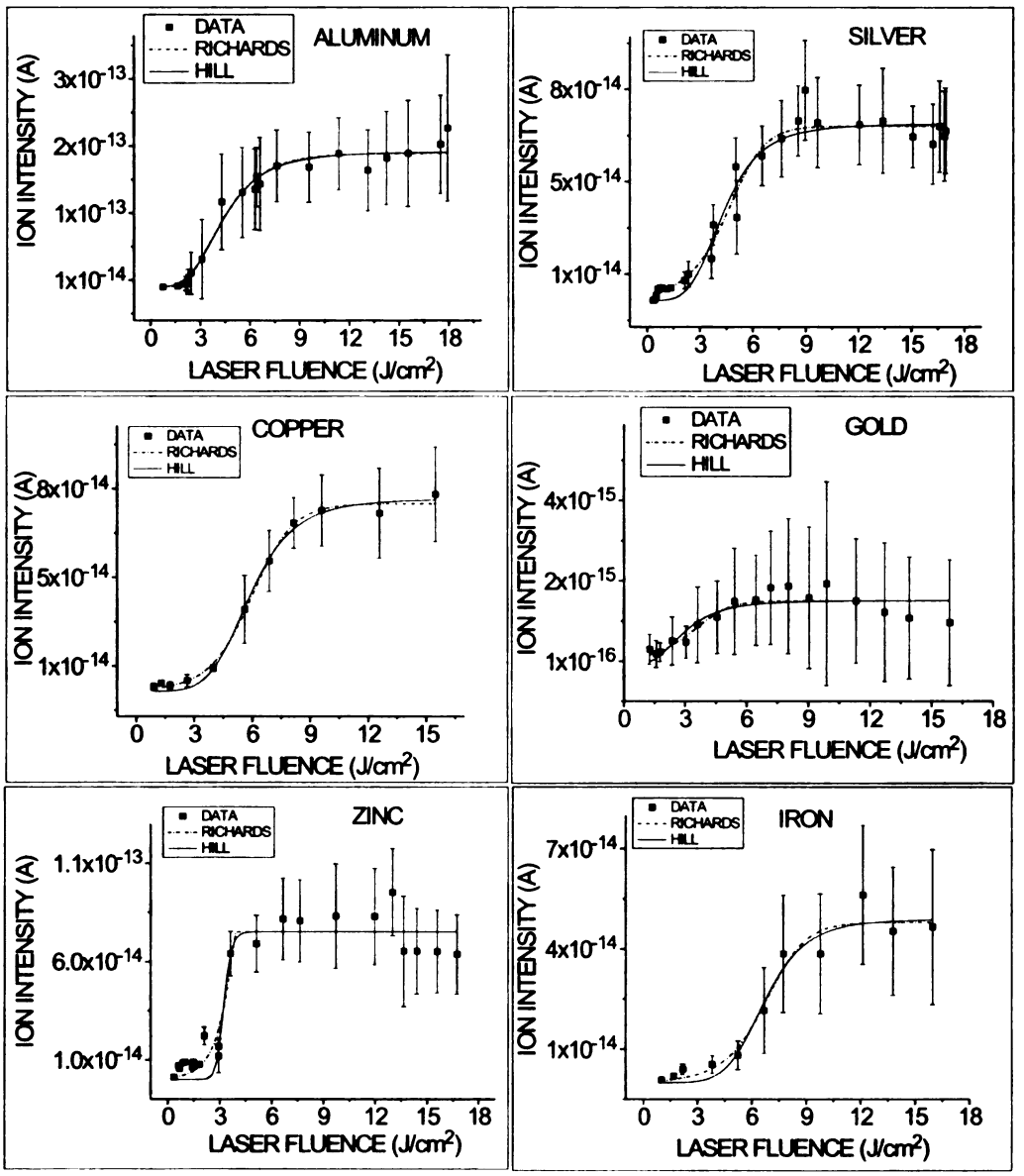

Figure 4.31: The detected ion intensity as a function of laser fluence. The ion intensity increases until a saturation point, which results from plasma shielding.

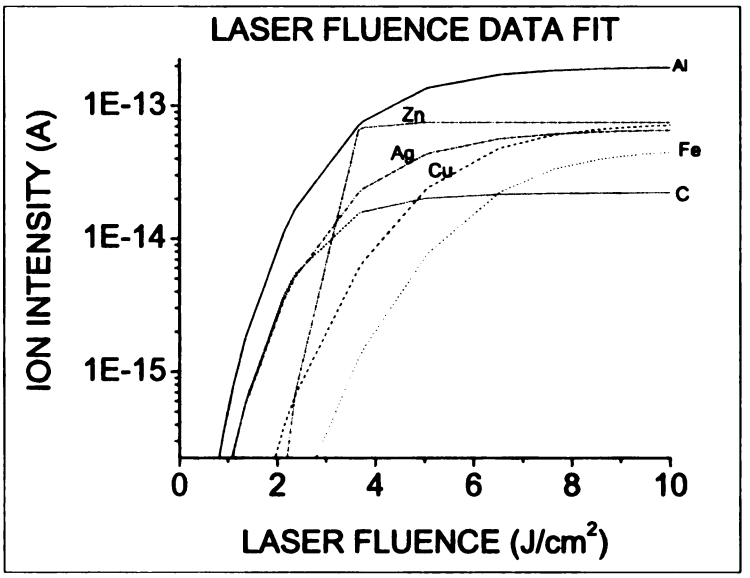

Figure 4.32: A comparison of the fitted functions using the HILL function from the laser fluence experiments.

edge of the laser pulse from the processes of inverse bremsstrahlung and multiphoton ionization. The free electrons shield the ablation target from further ablation during the nanosecond laser pulse. The actual fluence at which the plateau was reached was different for each target, as shown in Figure 4.32, but this saturation point always occurs at moderate fluences under 10 J/cm^2, similar to other results [58]. A further indication of the saturation of the ion intensity is shown in Figure 4.33, which shows the leakage current on the rings (V_r) and the target (V_t). As the laser intensity increases, the leakage current also increases until a saturation point is reached (the applied bias on the rings and the target was held constant for these trials). This further illustrates the generation of a strong and saturated plasma during the ablation process.

Threshold Laser Fluence

The threshold laser fluence is the laser energy per unit area needed to initiate the removal of material from a target surface. For the present study, the threshold fluence,

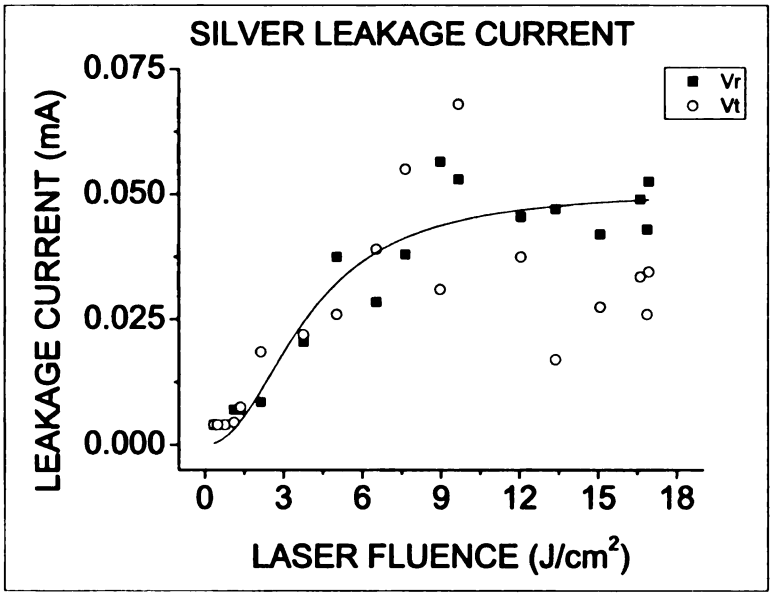

Figure 4.33: The leakage current during the laser ablation fluence studies of a silver target, which demonstrates a saturation level.

F_{th} is defined as the point when the ablated ion intensity is 1.5 % of the maximum value, or the saturation value. The threshold value was determined from the fits to the fluence data in Figure 4.31. At low fluences, the HILL fit (Eqn. 4.7) provided the best fit for the Al and Ag data, while the SRICHARDS fit (Eqn. 4.8) was more appropriate for the other targets. A fit comparison for Ag and Zn is shown in Figure 4.34. The threshold fluence $F_{th}(EXP)$ is given in Table 4.11, along with the calculated threshold fluence from Section 2.2.2, $(F_{RGA}(EXP))$, and literature values. The F_{RGA} is the minimum laser energy needed to ablate the target to a level that ions can be detected by the RGA and was measured in mass scan mode of the RGA as previously mentioned in this chapter. The measured threshold fluences, both F_{th} and F_{RGA} are compared to the calculated values and literature values in Figure 4.35. As previously discussed in Section 2.2.2, the thermal model seems to over-estimate the threshold fluence for silver. In general, the experimental values agree with the thermal model.

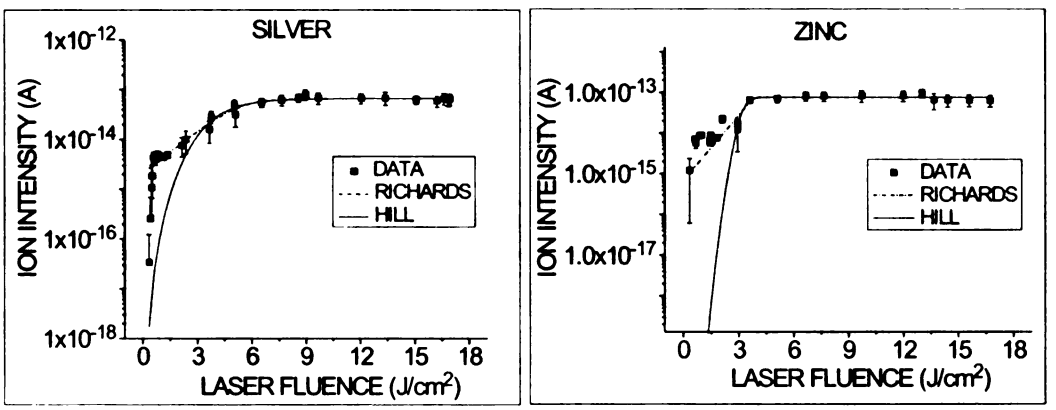

Figure 4.34: A comparison of the fits to the data for Ag and Zn. The HILL equation matches the data better at low fluences for silver, while the RICHARDS equation matches the data better at low fluences for zinc.

Table 4.11: Calculated and measured fluence threshold for the ablation of metal targets determined in this research. All values are in units of J/cm^2.

Target	$F_{th}(CALC.)$	$F_{th}(EXP.)$	$F_{RGA}(EXP)$	F_{th} [88]
Al	1.74	1.54	1.65	0.99
Fe	0.53	1.22	0.99	1.20
Cu	0.92	1.03	0.96	1.18
Zn	0.58	0.41	0.34	0.86
Ag	3.20	1.54	0.48	-
Au	1.10	0.64	1.28	-
C	0.35	0.98	1.21	-

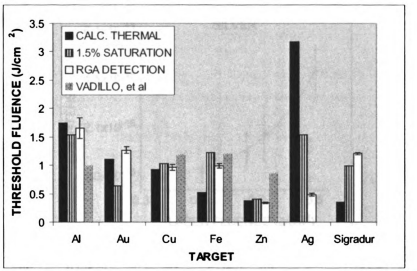

Figure 4.35: The threshold fluence (1.5 % saturation) is compared with the RGA threshold fluence, calculated values with the thermal model (Section 2.2.2) and other work [88].

Multiphoton Ionization

As discussed in Section 2.3, multiphoton ionization (MPI) is a process that occurs during plasma creation in laser ablation. A power law fit to the data can determine the presence of multiphoton processes [89]. The power law fit can be described by the following equation:

$$I = aF^{n_p}, \tag{4.9}$$

where I is the ion intensity, a is a coefficient, F is the laser fluence (J/cm^2), and n_p is the power or number of photons. The low-fluence data (at approximately the threshold fluence level) from the laser fluence experiments (Figure 4.31) were fit with Equation 4.9. However, the ion intensity of the low-fluence data was not accurately detected by the RGA since the intensity is at the low threshold/noise level of the RGA. Therefore, the statistics were fairly low for the low-fluence data. The presence of MPI was inferred using the power law fit method for the carbon, aluminum and silver targets. For instance, the silver data and power law fit are shown in Figure 4.36. Based on the ionization energy of silver, 7.6 eV, four 2.3 eV photons are needed to

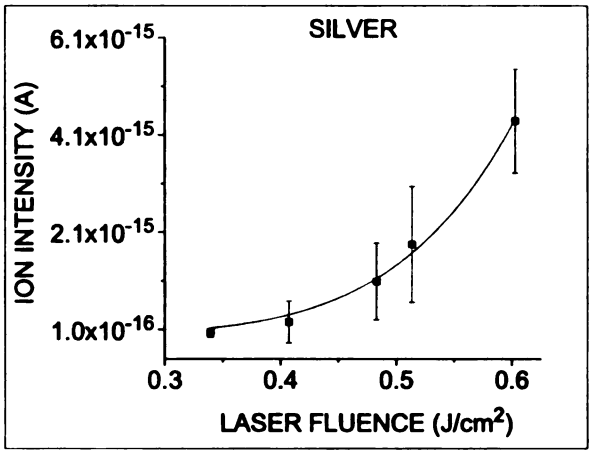

Figure 4.36: The multiphoton ionization of silver. The data were fit by a power law, and n_p is approximately 6, corresponding to 6 photons.

Table 4.12: Results from the power law fit method indicating a multiphoton process, where P_{min} is the minimum number of 2.3 eV photons needed for ionization and n_p is number of photons from the power law data fit.

Target	IE (ev)	P_{min}	n_p
C	11.3	5	6.8 ± 0.4
Al	6.0	3	11.3 ± 1.5
Ag	7.6	4	6.1 ± 0.4

ionize silver. From Figure 4.36, n_p is approximately six, corresponding to a six-photon ionization process. A silver atom can absorb more photons than needed for ionization, which is a process called "Above-Threshold Ionization" (ATI) [90]. The results of the power law fits for carbon, aluminum, and silver are summarized in Table 4.12. The low fluence results demonstrate the contribution of MPI during laser ablation.

4.3.5 Ablation Stability and Reproducibility

Having optimized all of the parameters, it was important to check the overall reproducibility and stability of the system. Since the process of laser ablation is multi-dimensional and can be difficult to control due to the large amount of processes involved, it was also necessary to determine how fast a given target would degrade

Table 4.13: Parameters during the laser ablation stability experiment.

PARAMETER	VALUE
Target Material	Iron
Target Position	Ring 15
V_R	1.96 V/cm
V_t	26 V
Laser Fluence	13 (J/cm^2)
Pulses (Day 1)	71828
Pulses (Day 2)	126525

and evolve over time. Multiple two-minute trials were performed with all parameters held fixed and the ion intensity was monitored as a function of total laser pulses for the metal targets. In general, the ion intensity was nearly constant over time and the data were reproducible, as shown in Figure 4.37.

Similar questions can be raised about the day-to-day stability of the laser ablation system. For the laser ablation in the gas cell (Chapter 5), it was necessary to have the ablation system running continuously for hours at a time. Ablation experiments in the literature often involve the ablation of a target for less than 1000 shots, which works out to ablation for only 50 s, assuming a 20 Hz laser. Therefore, it was necessary to determine how the laser ablation system would function over long periods of time. A stability experiment was run over two days; the parameters are given in Table 4.13. The data obtained during this continuous laser ablation were divided into 2-minute segments and is shown in Figure 4.38. It is apparent from Figure 4.38 that the laser ablation system is stable enough to run continuously for multiple hours.

4.3.6 Sigradur^{TM} Target in Vacuum

In addition to a variety of metal targets, the laser ablation of carbon was also studied. As mentioned previously, others have studied the ablation of carbon extensively. One study found that Sigradur-G^{TM} does not melt during laser ablation, but evaporation occurs directly from the solid surface [83]. Another study found that carbon clusters are vaporized directly from the surface of a graphite target from multiphoton

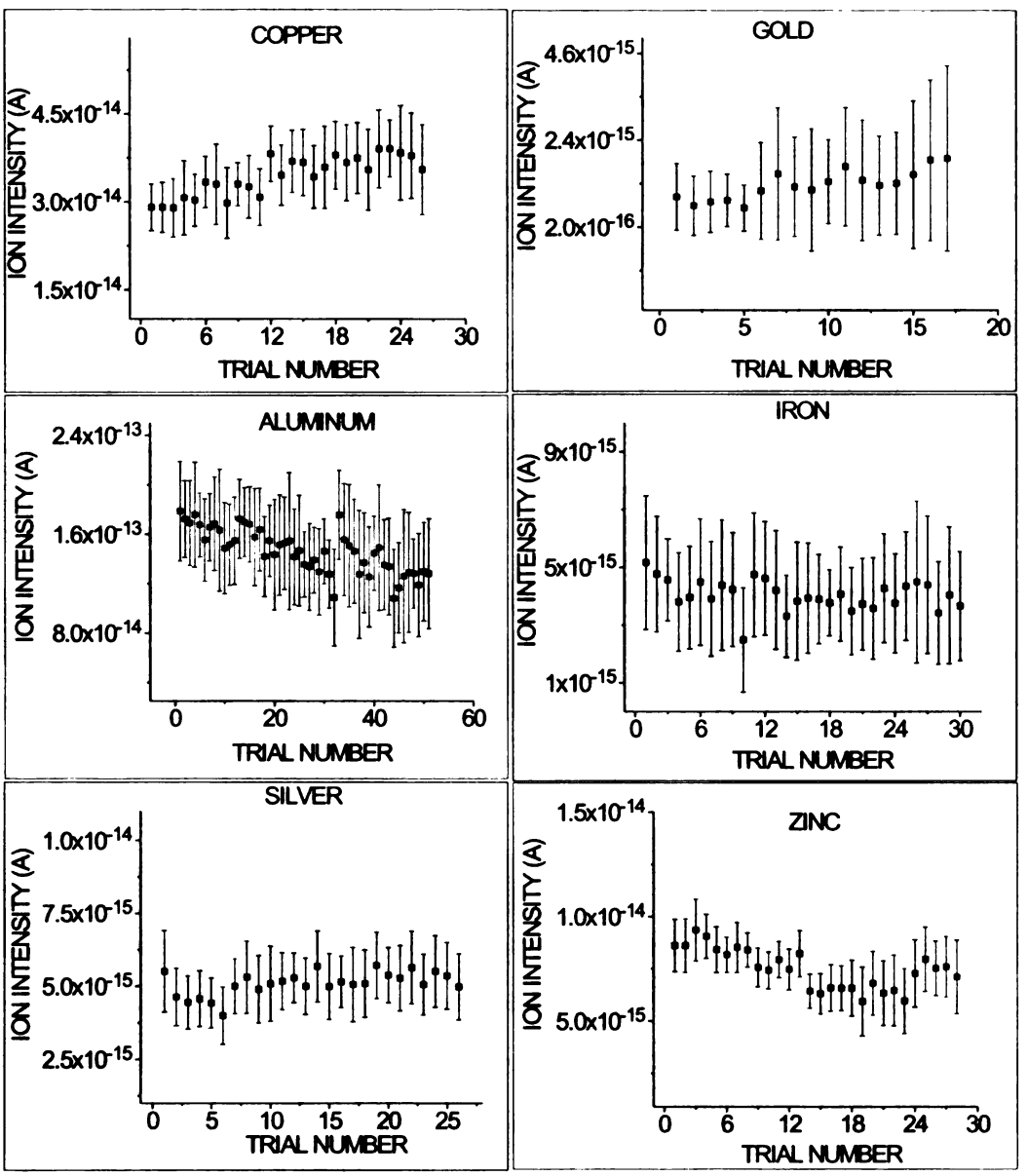

Figure 4.37: The reproducibility of the ion intensity as a function of trial number for the metal targets. The process of laser ablation was found to be reasonably reproducible, except for the target degradation and evolution over time.

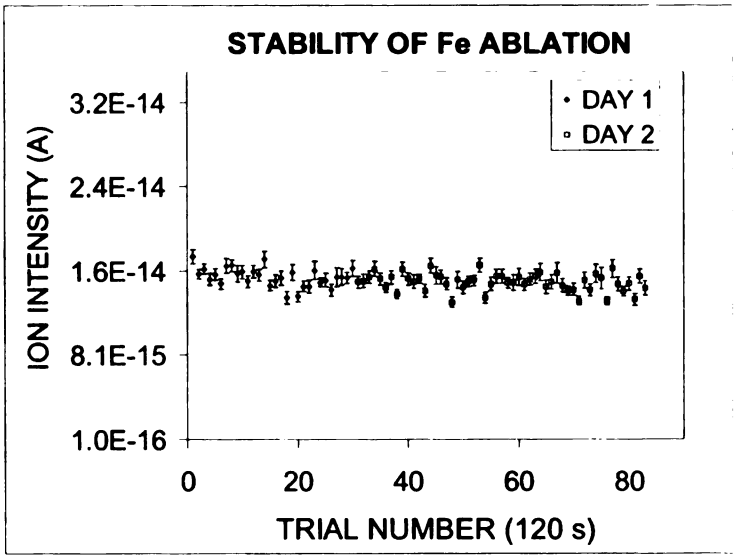

Figure 4.38: The ion intensity during the continuous laser ablation of an iron target over the course of two days.

conversion into thermal energy at fluences ranging from 0.65 J/cm^2 to 3.35 J/cm^2 with 532 nm laser photons [82]. Carbon clusters are formed when graphite or glassy carbon is ablated both under vacuum and atmospheric conditions [46,48,82]. In addition, it has been shown that C_{60} and Sigradur^{TM} produce clusters when ablated [81]. During the ablation of Sigradur^{TM} with fluences as low as 0.1 J/cm^2, Blaum found C_n clusters of up to n = 23, but the most common clusters were $3 < n < 11$ [37]. Experiments were performed in the present work with the goal of producing clusters, yet none were detected. The low fluence range (0.1 J/cm^2) used by Blaum to produce clusters was obtained in the present system by adjusting the optical isolator and half wave plate settings to lower the laser energy. However, no clusters were detected under vacuum conditions. Several possibilities can explain the lack of clusters: the intensity of the produced clusters could have been below the threshold of the RGA detector, (typical RGA scans for detected ion currents were already low, at the fA range), or photodissociation by the laser during the ns pulse, or dissociation by collision with other clusters and ablated species [46,91]. The dense, hot plasma formed within the enclosed target holder during laser ablation provides an environment conducive to

collisions between its constituent particles. As a side note, no clusters were detected in the case of the metal targets, and other groups have also noticed no metal clusters under similar ablation conditions [67].

Carbon Parametric Studies

The data from the parametric studies of carbon in the high vacuum chamber are shown in Figure 4.39. In general, the ablation of carbon in vacuum was not greatly affected by changing the experimental parameters in contrast to the metal targets except that the detected ion intensity seems to increase as the ablation target was moved further back in the chamber, closer to the RGA. However, the error bars on the data are large, making the clear identification of trends difficult.

4.3.7 Target Comparison and Target Properties

The laser ablation data for the metal targets were compared to physical/chemical properties of the bulk targets, as shown in Figures 4.40 and 4.41. The data are for the ablation of metal targets under the same conditions at a laser fluence of 1.6 J/cm^2.

The electron workfunction, Φ, is the energy needed to remove an electron from a metal surface. Both the chemical bond strength and Φ are related to the amount of energy needed to ablate the sample and as expected, as the bond strength increases, it is more difficult to ablate the sample, and the detected ion intensity decreases, as shown in Figure 4.40. Similarly, as Φ increases, more energy is required to remove an electron, and the detected ion intensity decreases.

The final three properties shown in Figure 4.40, T_m (K), T_b (K) and $\Delta_{vap}H^0$, are all related to the bond energy, and show the same general trend of the ion intensity being inversely proportional to each variable. The enthalpy of vaporization, $\Delta_{vap}H^0$, is the amount of energy needed to vaporize a sample. As $\Delta_{vap}H^0$ increases, the

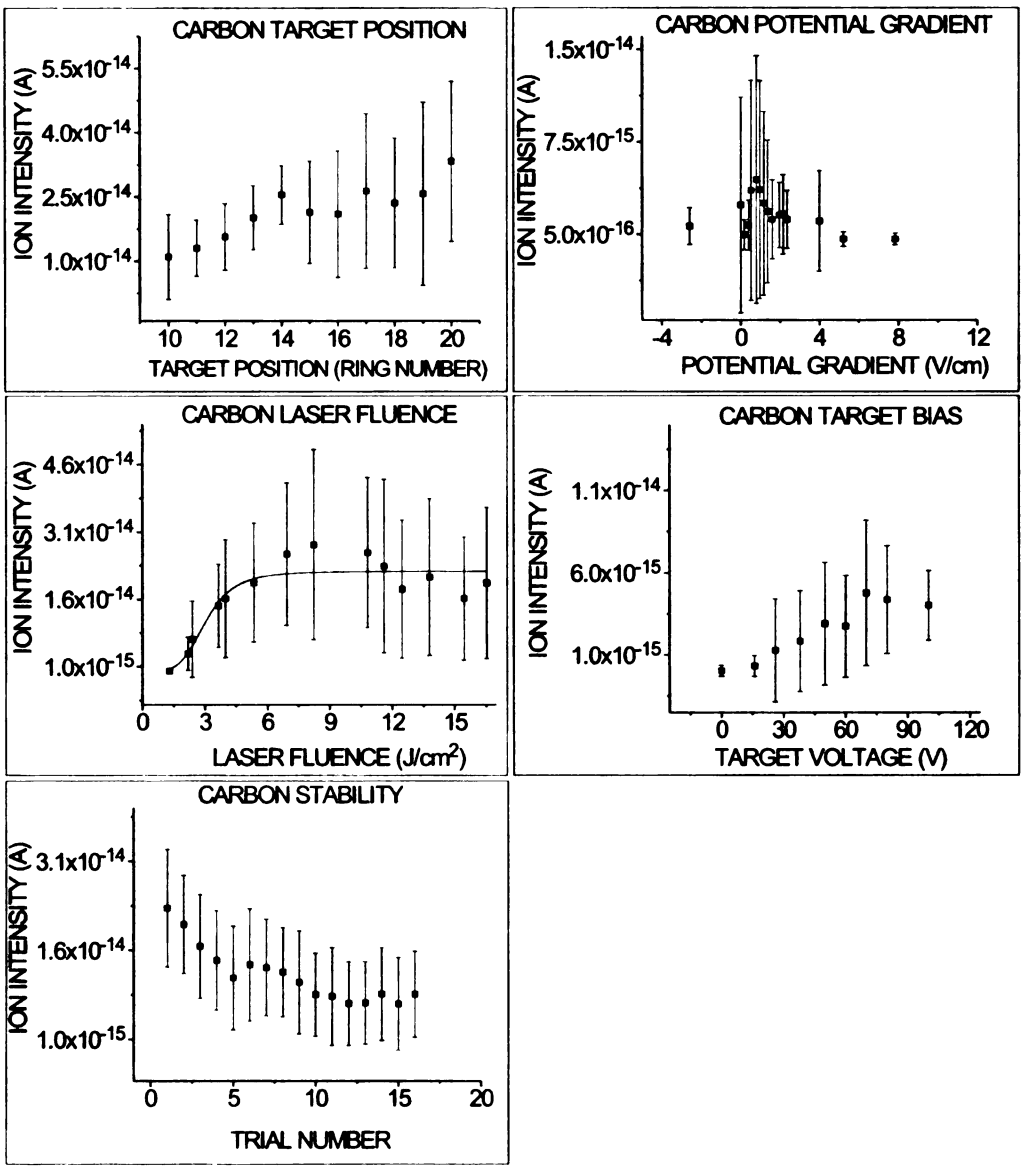

Figure 4.39: Data from the laser ablation of a Sigradur^{TM} target under vacuum conditions.

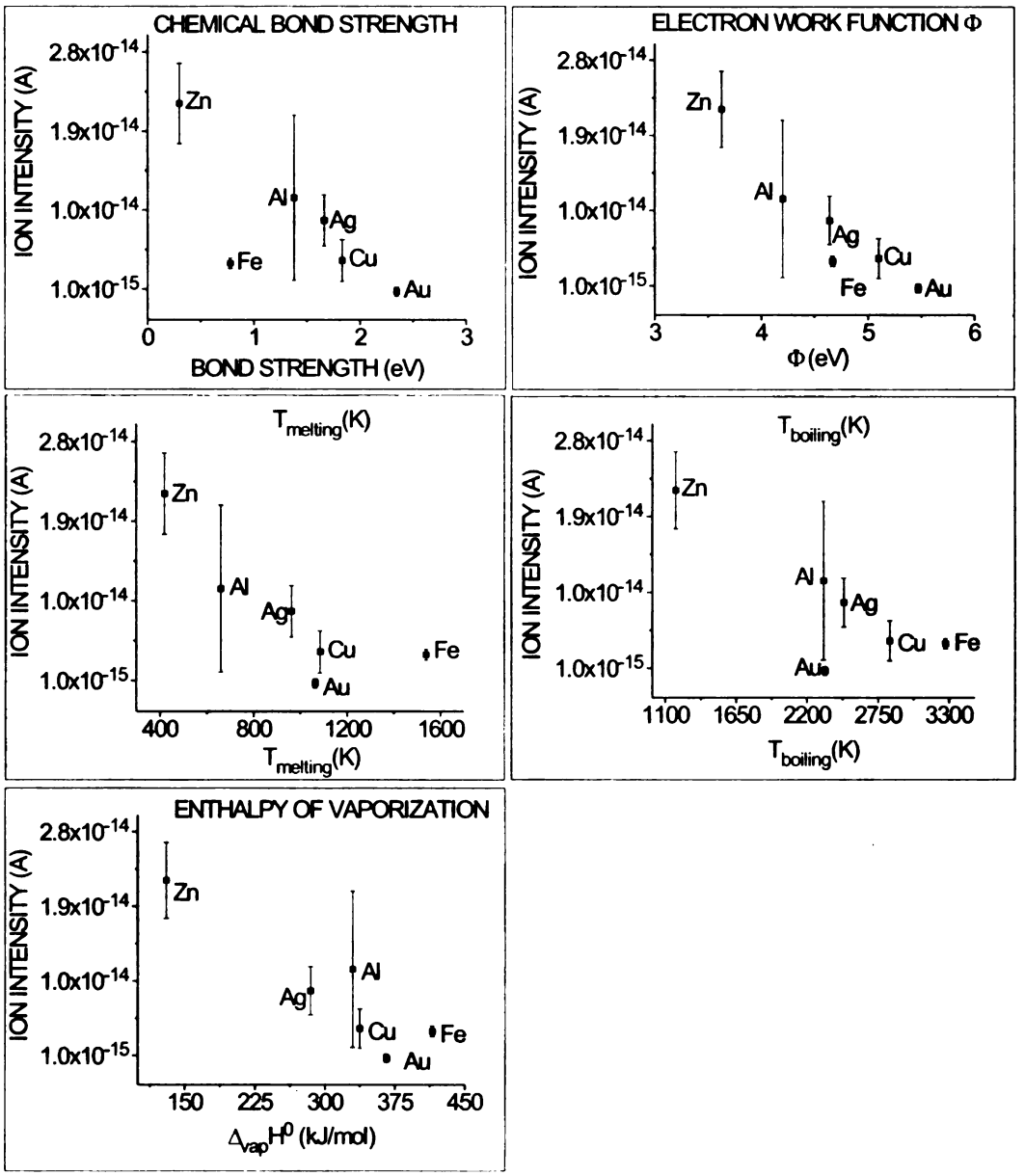

Figure 4.40: The laser ablation data as a function of bulk metal target physical/chemical properties.

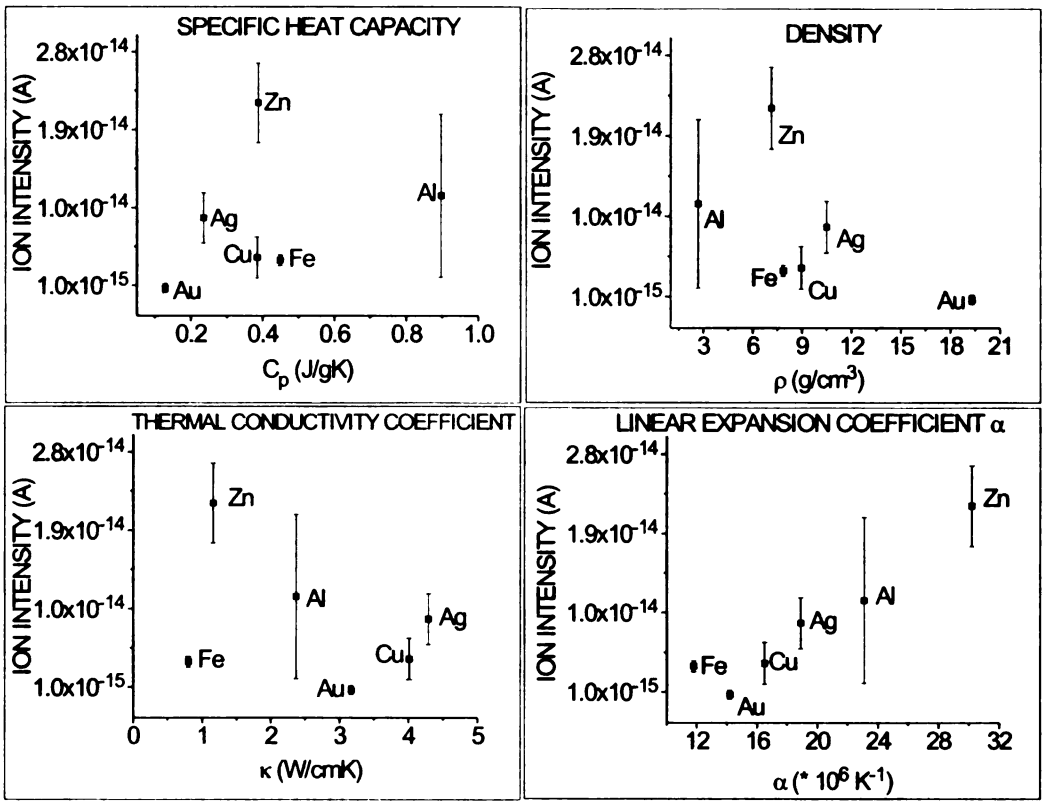

Figure 4.41: The laser ablation data as a function of bulk metal target physical/chemical properties.

detected ion intensity decreases, a trend that has been seen by others [92]:

$$R_{evap} \propto \frac{1}{\Delta_{vap}H}, \tag{4.10}$$

where R_{evap} is the rate of evaporation.

There does not seem to be a correlation between the detected ion intensity and the specific heat capacity c, the density ρ, and the thermal conductivity of the target κ, as shown in Figure 4.41. Recall that the thermal model, Section 2.2, depends on these values. The threshold fluence was estimated using the thermal model and agrees reasonably well with the results, as previously mentioned. However, the data (above the threshold fluence) do not seem to depend on c, ρ, and κ. Therefore, since no relationship is seen in Figure 4.41, it seems that the thermal model is not complete in describing the laser ablation mechanism above the threshold fluence; other parameters contribute to the ablation process.

Another property, the linear expansion coefficient α, is a measure of the change in length (volume) in response to a change in temperature:

$$\alpha = \frac{1}{V}\left(\frac{\partial V}{\partial T}\right)_p \tag{4.11}$$

In the exfoliational sputtering model [44] of laser ablation, flakes are removed from the target surface as a result of thermal shocks. The amount of thermal shock experienced by a target can be described by the thermal stress, S_t:

$$S_t \propto E\alpha, \tag{4.12}$$

where E is Young's Modulus and α is the linear coefficient of thermal expansion. As the amount of thermal shock to the target increases, which is proportional to α, the amount ablated increases, which is seen in Figure 4.41. It is apparent that the laser ablation mechanism and yield are dependent on the bulk properties of the target, in

addition to laser characteristics and the background conditions.

4.4 Mass Loss Calculations and Results

The mass ablation rate, $\dot{m}$, is defined as the amount of mass ablated per second per unit area, and is a useful parameter for laser produced plasmas [52,93,94]. The related $\dot{m}_m$ is written in terms of the laser energy, mass change of the sample, the time of ablation, spot size or area of ablation, and the molecular mass of the material itself, and is defined as

$$\dot{m}_m = \frac{\Delta m_t}{\mathcal{M} S_0 (P_l / r_r)}, \tag{4.13}$$

where $\dot{m}_m$ is the mass ablation rate in ablated moles per second per area, Δm_t is mass loss of the target, $\mathcal{M}$ is the molecular mass of the target, S_0 is the beamspot area, P_l is the number of laser pulses, and r_r is the laser repetition rate, 20 Hz.

The mass loss of each target was determined by weighing the targets before and after each ablation experiment. The change in mass of the target holder was also measured, since some of the ablated material did not escape the holder. Table 4.14 illustrates the change in mass of target and target holder, the weighted average laser energy, the number of laser pulses, and finally, the calculated number of ions escaping the target holder per pulse (from the measured target mass before and after ablation). The negative values of Δm_t describe the mass loss of the target, while the positive values of Δm_h describe the mass gain of the holder. The holder occasionally lost mass, given by negative Δm_h values. In order to determine whether a relationship existed between the laser energy and $\dot{m}$ among the metal targets with varying molecular masses, $\dot{m}$ was first converted to the number of moles ablated per second per area $\dot{m}_m$, only considering the mass loss of the target. The results are shown in Figure 4.42, which shows a linear relationship between the average laser energy and the mass

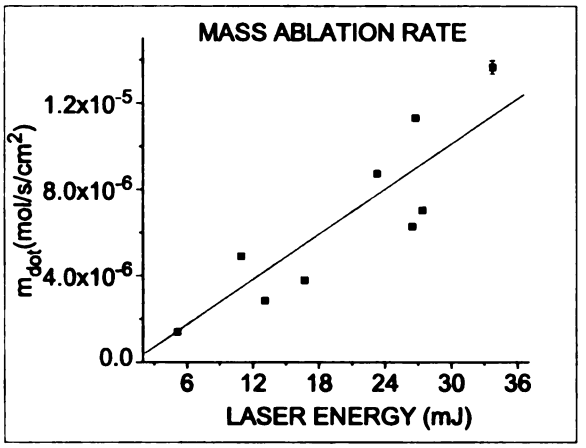

Figure 4.42: The mass ablation rate, $\dot{m}$, as a function of average laser energy for the metal targets in this research.

Table 4.14: Data for mass loss calculations

Target	Δm_l	Δm_h	Energy (mJ)	Pulses	Particles/s
Al	-0.032	0.031	23.2	489800	$1.8 \cdot 10^{13}$
Al	-0.023	-0.054	33.7	222120	$7.7 \cdot 10^{15}$
Cu	-0.024	0.020	26.5	216740	$1.8 \cdot 10^{14}$
Fe	-0.013	0.010	16.7	215957	$1.1 \cdot 10^{14}$
Au	-0.049	0.041	27.4	127589	$1.9 \cdot 10^{14}$
Au	-0.086	0.052	26.8	140539	$7.4 \cdot 10^{14}$
Ag	-0.020	0.017	13.1	239975	$7.9 \cdot 10^{13}$
Zn	-0.039	0.034	10.9	437867	$9.9 \cdot 10^{13}$
C	-0.028	0.016	24.4	160283	$3.7 \cdot 10^{15}$

ablation rate. The data could be fitted with the following equation:

$$\dot{m}_m = 3.49 \cdot 10^{-7} \phi_a - 3.6 \cdot 10^{-7}, \tag{4.14}$$

where ϕ_a is the average laser energy. As the laser energy increases, the amount of material per pulse ablated increases. This gives an estimate of the degradation rate of the target, in addition to the amount of material created per pulse, which can also be used to estimate the initial plasma density [70].

4.5 Initial Voltage Test for Gas Studies

Prior to running the laser ablation system in the gas cell, the HV chamber was used to determine the approximate attainable voltages on the rings and target during the laser ablation process. As demonstrated in Section 4.3.4, the applied voltages did not affect the ablation process except at the extremes in vacuum. Under helium conditions, however, the voltage holding capabilities of insulators is degraded. In addition, the process of laser ablation in gas affects the electric field. Therefore, a preliminary test was done in the HV chamber with air and helium to determine the approximate voltages needed. In an ambient air background, with a laser fluence of 18.8 J/cm^2, the maximum voltage on the first ring was 2400 V before a discharge was created. At an intermediate pressure of air at 29 Torr, the maximum voltage attained on the first ring was only 420 V. The chamber was then filled with 760 Torr of helium (not ultra-pure), and the maximum attainable voltage on the first ring at 18.8 J/cm^2 was only 600 V, implying that the voltages in the gas cell should not exceed 600 V during the laser ablation tests.

4.6 Data Summary

Although the experimental conditions in the high-vacuum laser ablation test chamber and the gas cell are not the same, the experimental results from the ablation data in the test chamber were important to establish reliable operation prior to the ablation studies done in gas. For instance, the measure of the threshold laser fluence was found to be similar to published work. In addition, the effect of the laser fluence on the plasma, and the subsequent saturation was observed, implying that higher laser fluences do not produce more ions. The potential gradient slightly affected the detected ion intensity, yet the target voltage and target position did not affect the detected ion intensity. The detected ion intensity also was compared to various properties of the targets and the results were found to be consistent with some of the bulk

properties of the materials. In addition, the isotopic abundances and mass loss as a function of energy were also determined and showed the level of sensitivity of the system. Finally, the maximum attainable voltage in helium conditions during laser operation and the stability of the laser ablation process under the HV conditions were determined, which was applicable to the laser ablation in the gas cell. Overall, the experiments done in the HV system provided an understanding of the laser ablation system and the parameters affecting the laser ablation process and ion transport.

Chapter 5

The Gas Cell Laser Ablation System

5.1 Experimental Details

The details of the laser ablation apparatus placed in the gas cell are very similar to the details of the apparatus placed in the HV ablation chamber. This section will discuss the additional details of the gas cell laser ablation system, in addition to giving an overview of the LEBIT experimental system used to detect the ions created in the buffer gas.

5.1.1 The Gas Cell

The gas stopping station is the first component in LEBIT, as shown in the LEBIT overview in Figure 5.1. The gas stopping cell at the NSCL is designed to stop nuclear projectiles traveling at relativistic velocities produced by fragmentation reactions in gas, and has been studied extensively recently [10–12], particularly in the dissertation work by P. Lofy [9]. Glass degraders, a wedge, a beryllium window, and approximately 1 bar of helium gas are used to stop the fragments. The glass degraders consist of polished glass plates of precisely known thicknesses. The glass plates are mounted on

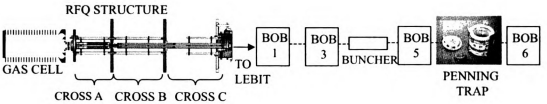

Figure 5.1: Simplified schematic view of LEBIT. Note that this is not drawn to scale, and does not show all of the LEBIT apparatus.

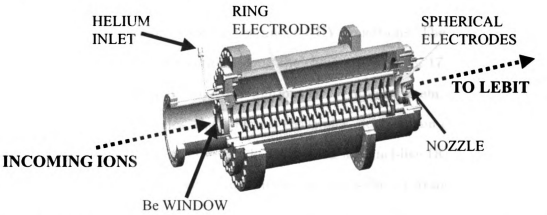

Figure 5.2: The LEBIT gas cell. The radioactive ions from the A1900 enter the cell through the Be window, become thermalized in the gas, drift and exit the cell due to a combination of the ring and spherical electrodes and the nozzle. The ions are then transported to LEBIT.

a motorized drive so the angle between them can be changed to increase the thickness encountered by the incoming ions. There are six positions on each stack of glass plates to select the desired thickness. Since the fast ions have varying momenta, a wedge-shaped degrader is necessary. A magnetic dipole disperses the ions onto the degrader, causing the ions with a higher momentum to travel through the thicker part, thus slowing them down more than ions with lower momentum that travel through the thinner section. Using the wedge, the beam can also be made nearly monoenergetic; this technique is known as range bunching [95]. A beryllium window is positioned at the gas cell entrance, further degrading the beam's energy.

The beam is finally stopped, or thermalized, in the helium-filled cell, shown in Figure 5.2. The distribution of stopped ions is called the range distribution. Once the

ions are thermalized in the gas cell, they are drifted through the chamber with a series of ring electrodes that create a DC gradient; the rings are very similar to the ring electrodes described in Section 4.1.1, which were the initial prototype for the gas cell. The outside edges of the 21 rings are triangular in shape, unlike the quasi-cylindrically shaped HV ring electrodes. The edges are smooth, in order to minimize sharp edges which cause electrical discharges. In addition, the ring electrodes are connected by 1 MΩ glass resistors, fabricated by Ohmite Manufacturing Company, Japan, that have a very low outgassing rate for use under UHV conditions. The ring electrodes are biased at five different locations along the chain (Rings 1, 3, 17, 18, and 21) to facilitate applying various voltage distributions to the whole system.

Another set of electrodes, the spherical electrodes, downstream of the ring electrodes, focus the ions towards the nozzle by creating a funnel-like DC field. A bias is also applied to the nozzle itself, which further enhances the ion transport. Once the ions are within a few mm of the nozzle, gas flow dominates, forcing the ions through the nozzle to a chamber held at a lower pressure (Cross A). A large roots blower pump removes the bulk of the helium gas from Cross A.

The gas cell is a difficult and constrained environment in which to study the thermalization and transport of fast ions (and ion formation in the case of the laser ablation system). The pressure can be varied in the gas cell, but most often, the pressure is kept at one bar. The gas cell does not have a fixed, static volume of gas, but rather, the gas flows through the cell, being removed by the large roots blower pump attached to Cross A. The constant gas flow is necessary for the ion extraction.

The gas is provided by a Gas Handling System, which constantly maintains the flow of gas at a selected pressure. Helium gas was chosen due to the fact that it has the highest first ionization potential. In addition, the purity of the gas can be brought to 99.999%. The purity of the gas is important for minimizing the contaminant molecular ions. Contaminants in the system either due to the hardware and chamber walls or the gas can undergo charge-exchange reactions with the ionized helium, thus in-

terfering and masking the ions transported from the cell. The gas also runs through a purification system before entering the manifold system. The gas is further purified by a series of devices, including a cold trap at liquid nitrogen temperature (77 K), a high temperature getter (445^o C), and an organometallic sieve. In addition, the manifold system is generally heated to temperatures greater than 120^o C when the system is not in use to ensure that no water or other contaminants are bound to the walls.

5.1.2 Transport and LEBIT Instrumentation

The LEBIT instrumentation has been developed over the course of a few years; for details, see [13,14,96-98]. After the ions are extracted from the gas cell, they are sent through a radiofrequency quadrupole (RFQ), shown in Figure 5.1. The RFQ uses a combination of DC and RF fields to guide the ions, in addition to acting as a mass filter. The beam can be monitored at a series of Beam-Observation Boxes (BOBs) in LEBIT. The ions are also cooled and bunched into packets in the Buncher/ Cooler section of LEBIT, which, similar to the gas cell, uses a buffer gas to cool the ions. The pulsed ion beam can then be sent to the Penning trap.

The Penning Trap

Currently, the end of the LEBIT beamline is the Penning trap, as shown in Figure 5.3, which is used to make precision mass measurements [99]. The Penning trap is enclosed in the bore of a 9.4 T superconducting magnet. A Penning trap uses the superposition of a constant magnetic field and varying electric fields to confine an ion. In a magnetic field, an ion spirals around the magnetic field lines, at a frequency called the cyclotron frequency, ω_c. An electric field axially confines the moving ion, and a radiofrequency source is used to drive radial motion. When an RF field matches the cyclotron frequency of the ion, the ion's kinetic energy increases. The time of flight of the ion after it exits the trap drops and the resonance frequency can be detected,

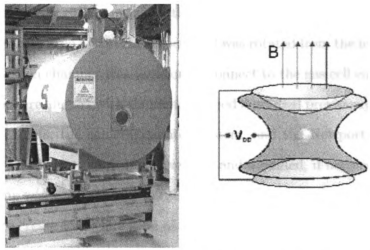

Figure 5.3: (Left) Photograph of the 9.4T Penning trap superconducting magnet. (Right) A schematic of the applied magnetic and electric fields on the hyperbolic Penning trap, from [99]

from which the mass, m, of an ion with charge q can be calculated, according to Equation 5.1:

$$\omega_c = \frac{q}{m}B, \tag{5.1}$$

where B is the magnetic field strength. The value for B must be precisely known in order to make a high-precision mass measurement. LEBIT's stable noble gas ion source is used to calibrate the magnetic field strength. The laser ablation ion source has not been used for this application, but is another possible source of ions for such calibrations.

5.2 Laser Ablation in the Gas Cell

The laser target holder and optics were moved to the gas cell for ablation tests to produce ions for the LEBIT system. The same conflat flange, including laser optics, and the same safety interlock system (Appendix C) that were used in the HV ablation chamber were used for the gas cell ablation tests. The beryllium window on the gas cell was removed and replaced by the laser ablation flange for the laser ablation studies. The main modification to the laser system was lengthening the tube between the

lower and upper box that contained the laser light and connecting the Euchner safety interlock system. The box at the upper level was rotated from the initial connection to the HV ablation chamber to a position to connect to the gas cell entrance flange. The laser optics were aligned with the same method described previously incorporating the cross-hair targets, the camera/monitor system, and the Newport motion-controlled actuators. The laser alignment was verified and modified, if necessary, after the roots blower pump was started. Prior to operating the laser, a discharge or spark-gap source was used to create ions. The time of flight spectrum from the discharge was used as a reference from day-to-day to ensure that the ion transport was constant.

5.2.1 Ablation Targets and Holders

Material Motivation

For the studies in the gas cell, iron, copper, and Sigradur^{TM} were used. The metals, iron and copper, were chosen based on their intermediate mass range. When these studies were done, the RFQ after the gas cell was set to a mass range approximately 30 to 100 amu. (The iron and copper isotopes are well-within this range.) The ablation of an iron target in the gas cell was performed prior to radioactive beam studies with LEBIT [100]. The second time that the laser ablation system was used in the gas cell, approximately six months later, copper and Sigradur^{TM} were used. The copper was interesting in that it has only two naturally occurring isotopes (compared to the four stable isotopes of iron). In addition, the copper mass spectrum in the HV system was well-resolved, as was shown in Section 4.3.

Sigradur^{TM} was selected since carbon is an excellent mass-reference [5], as its mass is exactly known. In addition, it has been shown that Sigradur^{TM} produces clusters when ablated [37, 81]. The mass of carbon is lower than the optimal mass range of the RFQ, but the clusters it can produce fit within the range. No carbon clusters were detected in the present work under vacuum conditions, as discussed in

Section 4.3.6. However, clustering is common under buffer gas conditions [43]. Unlike the HV ablation results, carbon clusters were produced in the present work during the ablation of a Sigradur^{TM} target in the gas cell, which will be discussed later.

Targets and Holders

Both target holders, Holder A and B (Figure 4.13) were used for the laser ablation in the gas cell. The larger target Holder B was used for the first set of measurements for the ablation of iron and later for copper. The measurements were done prior to the simulations of the plume length discussed in Section 2.4.3. Both target holders were used when carbon was ablated in the gas cell since the simulations of the plume length illustrated the need for a smaller target holder in ablation in a buffer gas. Before changing target holders, a large slot was cut in Holder B to facilitate in the escape of the plume from the holder, but this did not have a large effect. In addition, as discussed in 4.1.5, a ceramic shield was added to capture some of the black, sooty fibers which were created when ablating a target in gas, see Figure 4.15.

5.3 The Laser Ablation of Metal Targets in the Gas Cell

The laser ablation of an iron target in the gas cell was performed prior to the completion of the entire LEBIT beamline. The second measurement with the copper and carbon targets was performed after the gas cell had been extensively cleaned and the LEBIT system was completed.

5.3.1 The Laser Ablation of Iron in the Gas Cell

Iron was used for the first simple tests of laser ablation in the gas cell and the laser ablation parameters are given in Table 5.1, including the average energy, total laser

Table 5.1: Ablation parameters during the ablation of an iron target.

Parameter	Value
Voltage Gradient on Rings	0.23 V/cm
V_T (Target)	300
He Pressure	590 Torr
Target Position	Ring 15
Average Laser Energy	5.1 mJ
Total Pulses	1543973
Mass Loss (Fe target)	0.0332 g

pulses and the mass loss (material ablated) of the iron target. The mass analysis components in the LEBIT system were not yet completely operational so a simple test was done to measure the ion current and electron current as a function of laser fluence, and the results are shown in Figure 5.4. The ion current was measured on the nozzle and the electron current was measured on Ring One, as shown in Figure 5.5. With increasing laser fluence, the number of ions detected in the gas cell increased, in addition to the number of free electrons, which follows the expected trend that increased laser fluence increases free electrons and ions. A comparison of the detected electron current during the ablation of iron in the gas cell to the data fit as a function of laser fluence for the ablation of an iron target under vacuum from Section 4.3.4 is shown in Figure 5.6. The SRICHARDS equation (Equation 4.8) was used to fit the results of the iron ablation under vacuum conditions and the same fit parameters were used. The electron current was multiplied by a factor of 4×10^{-6} for viewing. In general, the data matches well with the fit from the iron ablation in the HV chamber, showing a general increase until a saturation point was reached. The ablation of iron in the gas cell was a very preliminary test to determine whether the ablation system worked in the gas cell. Ions were detected in LEBIT and were only present with gas flow and when the laser was operating (as expected), yet no conclusions were made since the LEBIT system was not fully operational at this point.

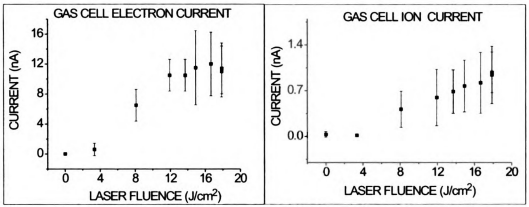

Figure 5.4: The electron and ion currents in the gas cell as a function of laser fluence.

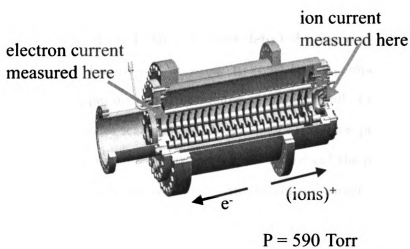

Figure 5.5: Schematic of the experimental set-up to measure the ion and electron currents in the gas cell as a function of laser fluence.

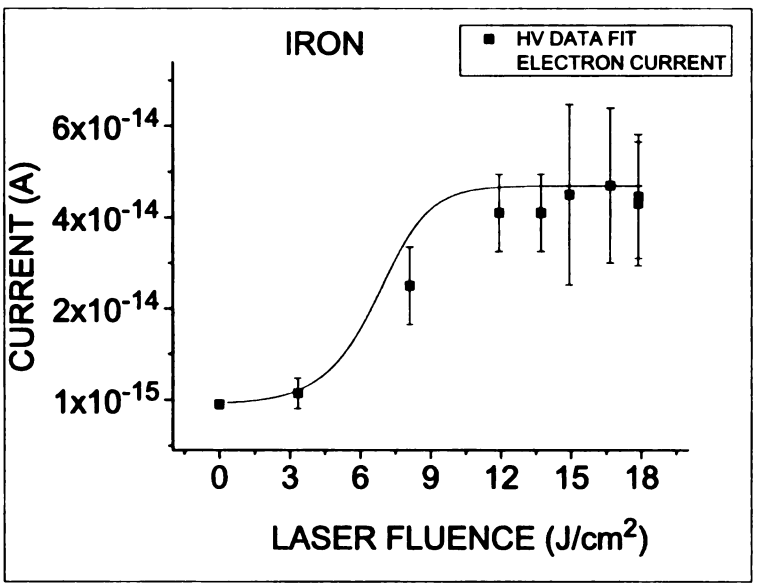

Figure 5.6: A comparison of the electron current in the gas cell as a function of laser fluence to the RICHARDS data fit from the ablation of an iron target in the HV system discussed in Section 4.3.4. The electron current is multiplied by a factor of 4×10^{-6} for viewing.

5.3.2 The Laser Ablation of Copper in the Gas Cell

During the subsequent ablation of a copper target in the gas cell, the effect of changing various parameters was studied. The ions were detected using a microchannel plate detector at BOB5 (see Figure 5.1). In order to consistently compare the results of the trials with differing parameters, the number of counts in all of the channels were normalized to the number of scans in the LEBIT data acquisition program EVA. The effect of changing parameters including the target voltage and the pressure of the gas cell was studied. The target voltage tests with the copper target were inconclusive due to an electrical discharge that obscured the results.

The pressure of the gas cell was varied for the laser ablation of copper, and some results are shown in Figure 5.7. As the pressure was increased, the detected ion intensity increased. Since the potential gradient was kept fixed for these tests, the only parameters affecting the drifting ions are the plume length and the gas flow.

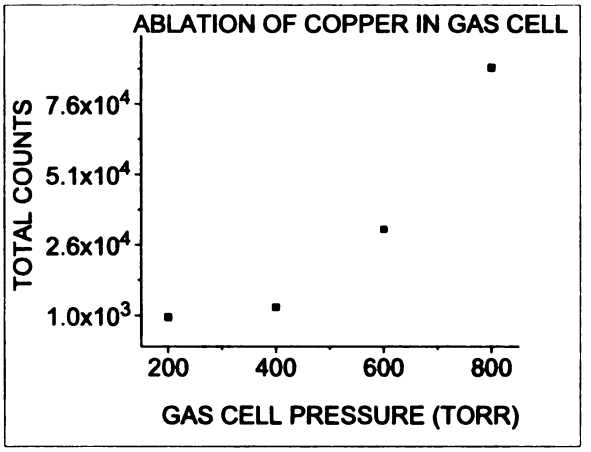

Figure 5.7: The effect of changing the pressure of the gas cell during the ablation of copper on the total counts detected at BOB5. The error bars are smaller than the data points.

The plume length and gas flow rate for the pressure range in this work are shown in Figure 5.8. Recall from Section 2.4.3 that the plume length is proportional to $P^{-0.2}$ for helium buffer gas and from the fit to the data in Figure 5.8, the gas flow rate is proportional to $0.0099 \times P$. In the range of 200 to 800 Torr, the plume length decreases by 24 %, while the gas flow rate increased by a factor of nine. Recall that the gas flow dominates the motion of the ions through the nozzle and out of the chamber. A pressure gradient exists between the gas cell and Cross A. As the pressure inside the cell increased, the pressure gradient also increased, forcing ions out of the cell at a faster rate. Therefore, one should expect the total counts to increase, since the changing gas flow rate as a function of pressure seems to contribute more to the yield than the slightly decreasing plume length as a function of pressure.

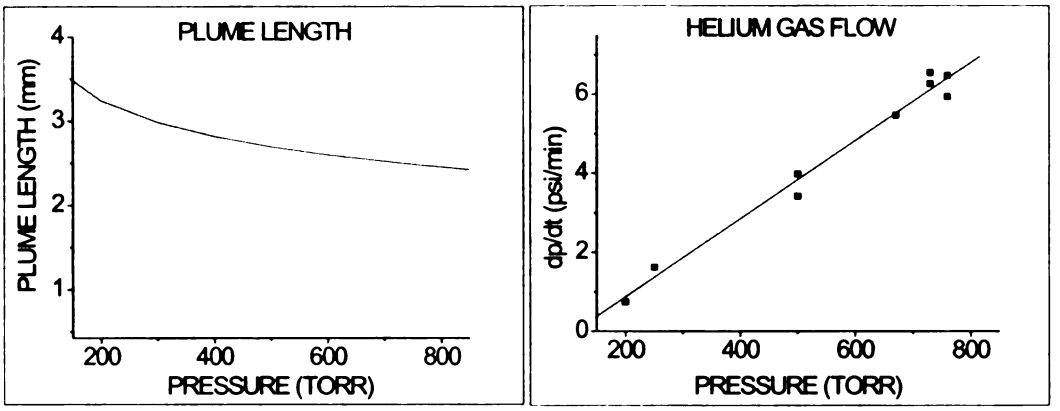

Figure 5.8: A comparison of the calculated plume length and the helium gas flow rate in the pressure range of 200-800 Torr. The gas flow rate changes more in this pressure range than the plume length.

5.4 The Laser Ablation of Sigradur^{TM} in the Gas Cell

During the laser ablation of Sigradur^{TM} (carbon) in the gas cell, the time-of-flight spectrum of ions after being collected in the LEBIT buncher was measured for various parameters, including the pressure of helium in the gas cell and the laser fluence. The large target holder, B, was used for these measurements. The ions were detected at BOB5 (see Figure 5.1). Another set of measurements were made with the small target holder, A, using the laser pulse to trigger the data acquisition system for time-of-flight measurements. The goal was to obtain information about the time distribution of ion collection from the gas cell and the ions were detected at BOB3 (before the buncher).

5.4.1 Parametric Studies

The effect of both the pressure and the laser fluence on the ion intensity was studied during the laser ablation of carbon in the gas cell.

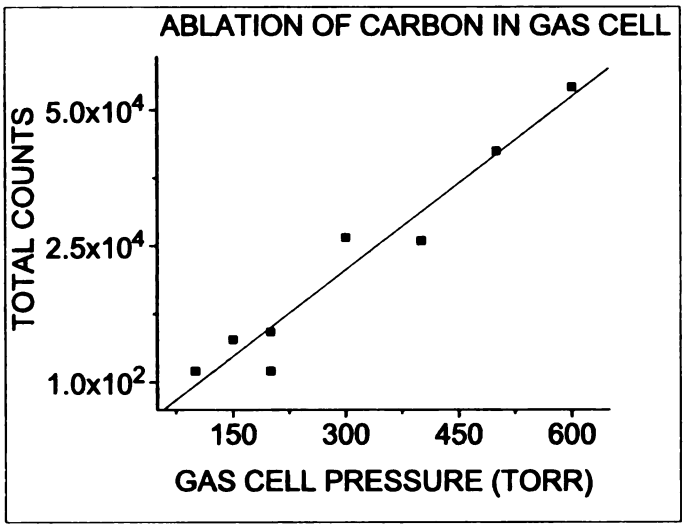

Figure 5.9: The effect of changing the pressure of the gas cell during the ablation of Sigradur^{TM} on the total counts detected at BOB5. The error bars are smaller than the data points.

Pressure Study

The effect of changing the buffer gas pressure in the gas cell during the laser ablation of carbon is shown in Figure 5.9. The laser fluence was 1.2 J/cm^2, the laser ablation target was located at Ring 15 (33 cm from the gas cell entrance, 17.0 cm from the exit nozzle) and the LEBIT settings were kept constant. The potential gradient on the ring electrodes was 5.6 V/cm. The ion intensity increased as a function of increasing pressure, similar to the results obtained with the copper target previously discussed, as shown in Figure 5.10. The results are again consistent with the increased pressure gradient causing an increase in the total number of ions leaving the cell.

Laser Fluence Studies

The laser fluence was also varied to study the effect on the ion intensity collected. The laser ablation parameters were kept fixed at the same values as the pressure studies, and the pressure was 200 Torr. The results are shown in Figure 5.11. In general, as the laser fluence was increased, the detected ion intensity also increased, which agrees

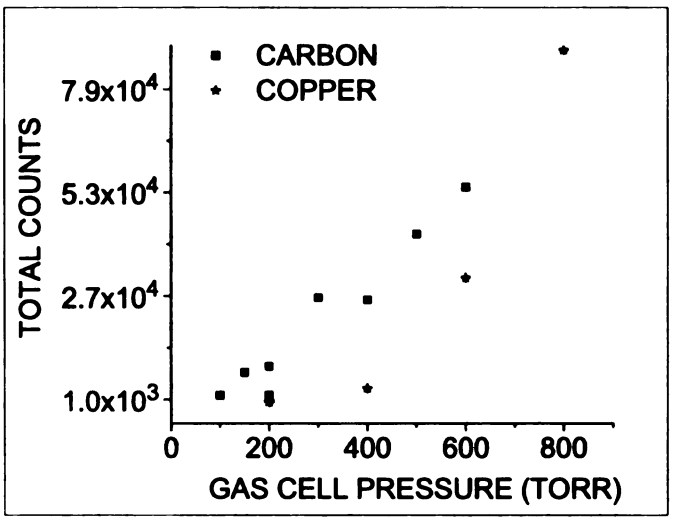

Figure 5.10: A comparison of the results from changing the pressure of the gas cell during the ablation of Sigradur^{TM} and copper. The ion intensity is detected at BOB5 and the error bars are smaller than the data points.

with the results from the HV system, discussed in Section 4.3.4, although the data are sparse.

5.4.2 Drift-time Studies

In the final set of measurements, the laser was used to trigger the time-of-flight system, which provided a direct measurement of the time the ions drifted after laser ablation. The number of ions was determined as a function of the ablation target position in the gas cell, the potential gradient, and the ablation target voltage. This allowed determination of the time for an ion to travel through the gas cell and ion mobility in the gas cell.

In these studies, the laser pulse was used to trigger a LEBIT digital oscilloscope. The laser repetition rate was decreased to allow enough time for the electronics to respond and process the data prior to the next laser pulse. The laser repetition rate in all of the other measurements was 20 Hz. Values of 5 Hz, 2 Hz, 0.2 Hz, and 0.5 Hz were tried and the optimum rate was found to be 0.5 Hz.

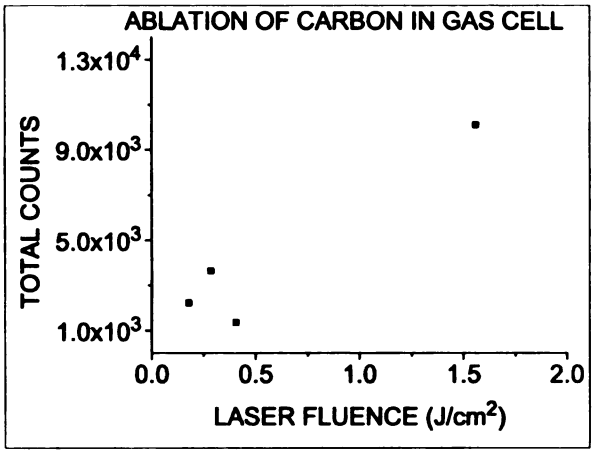

Figure 5.11: The effect of changing the laser fluence during the ablation of Sigradur^{TM}. The error bars are smaller than the data points and the data were taken at BOB5.

Ion Drift as a Function of Ring Electrode Potential Gradient

The effect of changing the potential gradient created by the rings on the ion collection was measured. The laser fluence was 1.4 J/cm^2, the lens position was kept fixed, and the target was kept at the same location in the gas cell at Ring 13, 20.7 cm from the nozzle. Four voltage files were used, as shown in Table 5.2, which produced slopes (V/cm) in the region of the ring electrodes (starting at 7 cm into the gas cell and ending at 44 cm) in the gas cell, as shown in Figure 5.12. The voltage distributions are labeled by their file names in the LEBIT database. The detected ion intensity as a function of potential gradient in the region of the rings (1-16) is given in Figure 5.13. Each data set was taken over ten data scans in EVA. The results of this measurement demonstrate that a steeper potential gradient forces more ions out of the gas cell, corresponding to more counts during a given data acquisition scan time.

Ion Drift as a Function of Target Position

The effect of changing the position of the ablation target within the gas cell was studied at a laser fluence of 1.4 J/cm^2. The potential gradient was kept constant; the voltage file was ...laser_50.set. The lens position and target voltage were adjusted

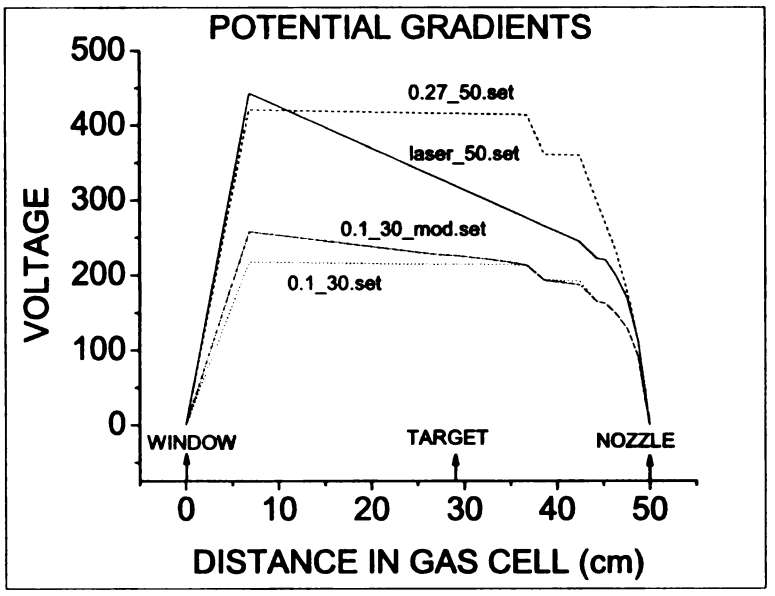

Figure 5.12: Various potential gradient distributions as a function of distance in the gas cell. The file names of these distributions are also shown.

Table 5.2: Voltage files for the potential gradient measurements. The voltage settings are labeled by their file names in the LEBIT database. The ring electrode gradient is given for Rings 1-16, where the slope is uniform. The total gradient includes the ring electrode gradient and the spherical electrode gradient. The spherical electrode gradient is almost identical for all of the distributions.

Voltage File	Ring Electrode Gradient (V/cm)	Total Gradient (V/cm)
...laser_50.set	5.6	10.3
...0.27_50.set	0.23	9.8
...0.1_30.set	0.14	5.1
...0.1_30.mod.set	1.4	6.0

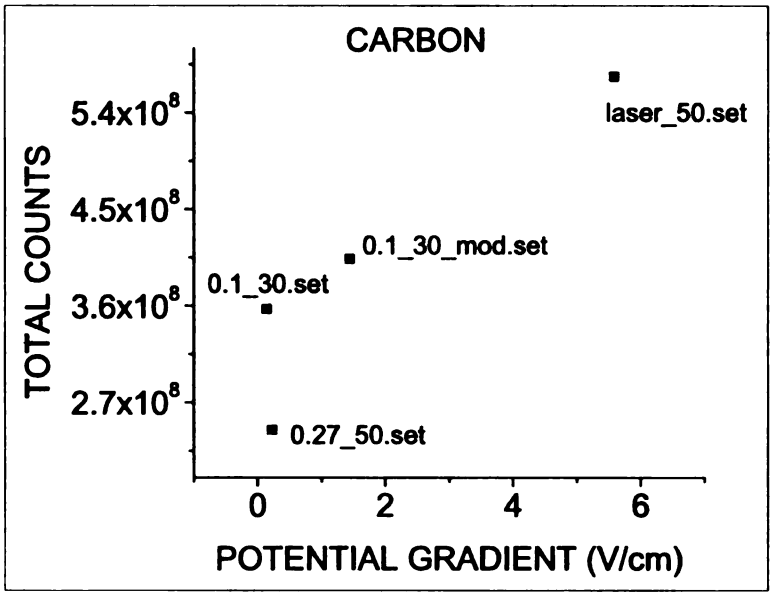

Figure 5.13: The detected ion intensity at BOB3 over 10 data acquisition scans as a function of the ring electrode potential gradient in the region of Ring 1-16. The error bars are smaller than the points

Table 5.3: Target voltage values during target location experiments.

Ring Number (Distance from the nozzle)	Target Voltage
10 (26.3 cm)	340
12 (22.6 cm)	348
13 (20.7 cm)	317
15 (17.0 cm)	293
16 (15.1 cm)	233
18 (11.3 cm)	265
20 (7.6 cm)	241

at each position to keep the distance from the lens to the ablation target and the electric field constant. The target voltage values are shown in Table 5.3 The data were normalized to the number of data acquisition scans.

The raw data are shown in Figure 5.14, with an offset applied to each spectrum for viewing. In each data set at each target position, peaks were detected corresponding to fast and slow ions, which demonstrate the existence of a temporally-split plume (a concept that was introduced in Section 2.4.4 and will be further discussed in Section 5.4.3). The data were rebinned and fit in ORIGIN's nonlinear least square

Table 5.4: Fit parameters for y_0 and y_e in Equation 5.2.

Ring	y_0	A	x_0	P	t_1	t_2
*R*10	$2.14 \cdot 10^5$	$4.26 \cdot 10^5$	$7.82 \cdot 10^2$	$4.87 \cdot 10^{-1}$	$7.11 \cdot 10^3$	$3.97 \cdot 10^4$
*R*12	$2.39 \cdot 10^5$	$4.54 \cdot 10^5$	$1.15 \cdot 10^3$	$7.58 \cdot 10^{-2}$	$3.81 \cdot 10^3$	$3.43 \cdot 10^4$
*R*13	$1.75 \cdot 10^5$	$6.68 \cdot 10^5$	$1.98 \cdot 10^3$	$4.86 \cdot 10^{-1}$	$1.12 \cdot 10^1$	$3.71 \cdot 10^4$
*R*15	$4.28 \cdot 10^4$	$3.18 \cdot 10^5$	$3.50 \cdot 10^2$	$8.97 \cdot 10^{-1}$	$1.73 \cdot 10^1$	$3.91 \cdot 10^3$
*R*16	$1.77 \cdot 10^5$	$9.34 \cdot 10^5$	$2.00 \cdot 10^2$	2.37	$4.79 \cdot 10^2$	$7.34 \cdot 10^3$
*R*18	$2.03 \cdot 10^5$	$2.33 \cdot 10^6$	$1.00 \cdot 10^2$	3.51	$4.59 \cdot 10^2$	$3.37 \cdot 10^3$
*R*20	$1.50 \cdot 10^5$	$3.79 \cdot 10^6$	$1.90 \cdot 10^2$	7.20	$1.62 \cdot 10^2$	$2.61 \cdot 10^3$

fitter using a custom, "user-defined" function:

$$y = y_0 + y_e + y_g, \tag{5.2}$$

where y_0 is a constant to account for the background, y_e is the fast or exponentially decaying peak, given by the expression

$$y_e = \left[A\left(1 - \exp\left[\frac{-x - x_0}{t_1}\right]\right)^P \times \left(\exp\left[\frac{-x - x_0}{t_2}\right]\right)\right], \tag{5.3}$$

where A is the peak amplitude, x_0 is the time offset, P is the power, and t_1 and t_2 are the peak widths. The thermal, or slow peak, was fitted to a Gaussian function, y_g, given by

$$y_g = \frac{B}{\omega\sqrt{\pi/2}} \exp\left(\frac{-2(x - x_c)^2}{\omega}\right), \tag{5.4}$$

where B is the peak amplitude, x_c is the centroid, ω is the peak width. The fit results are compared to data in Figures 5.15 and 5.16, and the fit parameters are provided in Tables 5.4 and 5.5.

The velocity of the fast peak was determined from the fit parameter x_0, which gave the time for the material in this peak to exit the gas cell, and the distance from BOB3 (see Figure 5.1). Both the velocity of the fast peak and the distance to the MCP detector at BOB3 are given in Table 5.6. The velocity of the fast peak as a function of target position is also shown in Figure 5.17. Similar to other results [101],

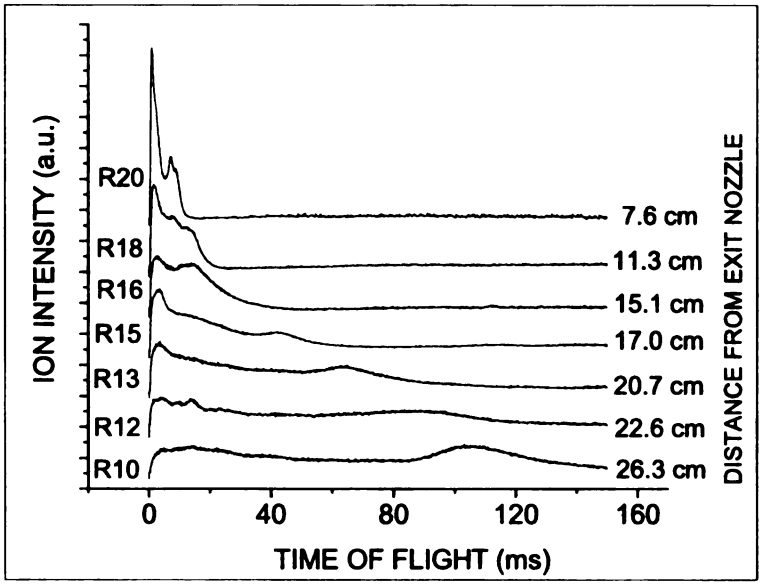

Figure 5.14: The time-of-flight data from the ion collection as a function of target position; the peaks are offset for viewing. The ring number corresponding to the target position is given on the left for reference.

Table 5.5: Fit parameters for y_g in Equation 5.2. The subscript "2" denotes a second thermal peak.

Ring	B_1	x_{c1}	ω_1	B_2	x_{c2}	ω_2
*R*10	$2.82 \cdot 10^5$	$1.07 \cdot 10^5$	$3.26 \cdot 10^8$	-	-	-
*R*12	$1.76 \cdot 10^5$	$8.57 \cdot 10^4$	$7.18 \cdot 10^8$	-	-	-
*R*13	$1.92 \cdot 10^5$	$6.49 \cdot 10^4$	$3.16 \cdot 10^8$	-	-	-
*R*15	$8.18 \cdot 10^4$	$1.51 \cdot 10^4$	$2.33 \cdot 10^8$	$3.63 \cdot 10^4$	$4.24 \cdot 10^4$	$1.02 \cdot 10^8$
*R*16	$5.11 \cdot 10^5$	$1.50 \cdot 10^4$	$1.15 \cdot 10^8$	-	-	-
*R*18	$5.15 \cdot 10^5$	$8.10 \cdot 10^3$	$1.40 \cdot 10^7$	$4.80 \cdot 10^5$	$1.39 \cdot 10^4$	$1.27 \cdot 10^7$
*R*20	$5.90 \cdot 10^5$	$7.01 \cdot 10^3$	$1.22 \cdot 10^6$	$5.51 \cdot 10^5$	$8.99 \cdot 10^3$	$1.91 \cdot 10^6$

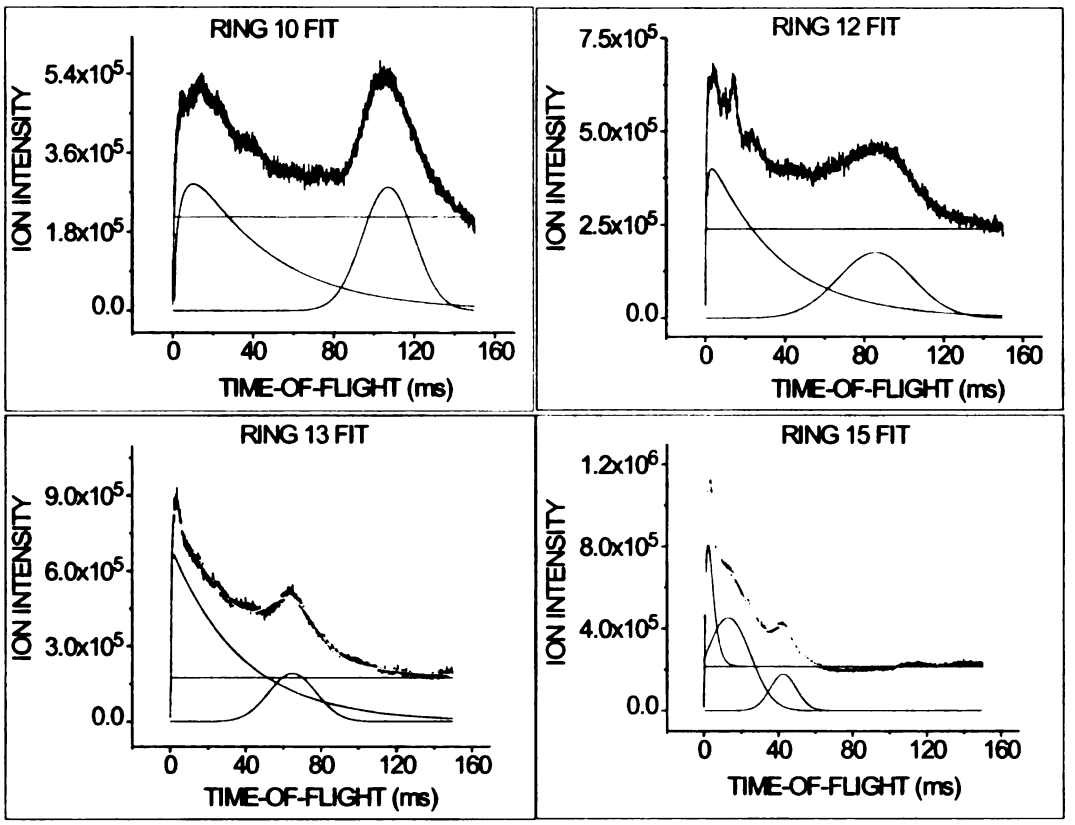

Figure 5.15: Part I- A comparison of the data and the fitted function that includes background, exponential, and Gaussian components.

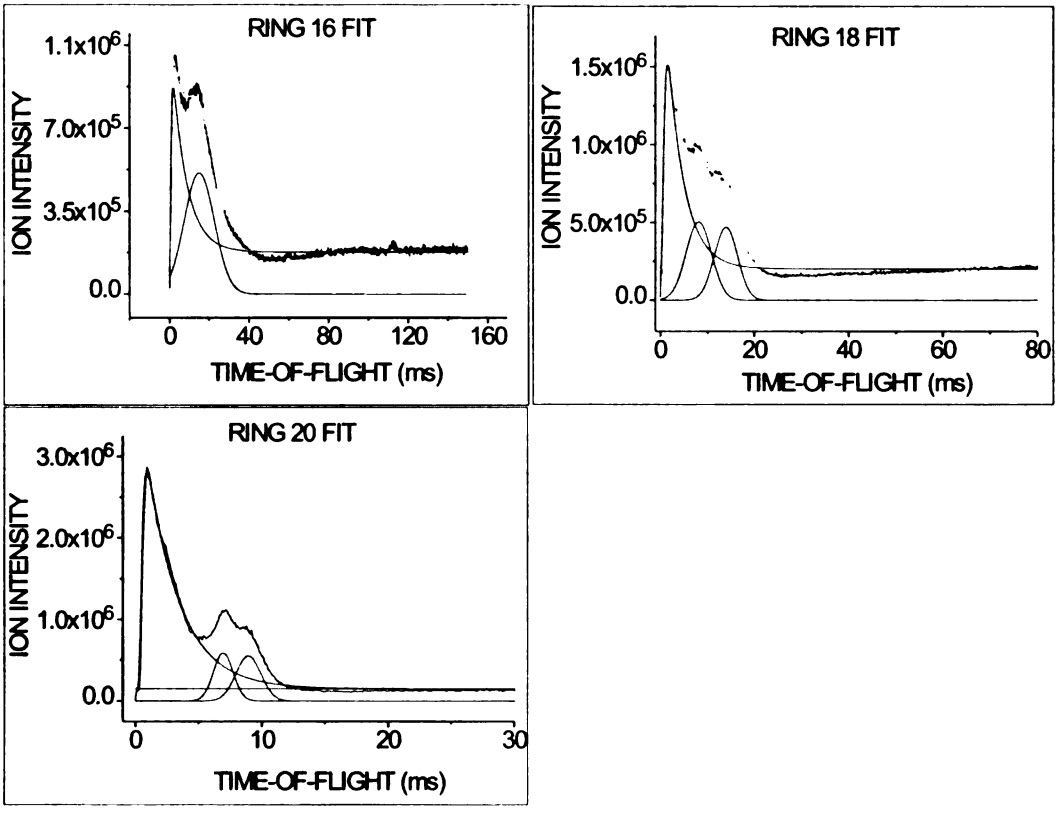

Figure 5.16: Part II- A comparison of the data and the fitted function. Note that the axes are not the same.

Table 5.6: The fast peak velocities obtained from the distance to BOB3 and the fit parameter $x_0(\mu s)$.

Ring Number	Distance to BOB3 (cm)	Velocity (cm/s)
10	580.9	$7.42 \cdot 10^5$
12	577.2	$5.01 \cdot 10^5$
13	575.3	$2.91 \cdot 10^5$
15	571.6	$1.63 \cdot 10^6$
16	569.7	$2.85 \cdot 10^6$
18	565.9	$5.66 \cdot 10^6$
20	562.2	$2.96 \cdot 10^6$

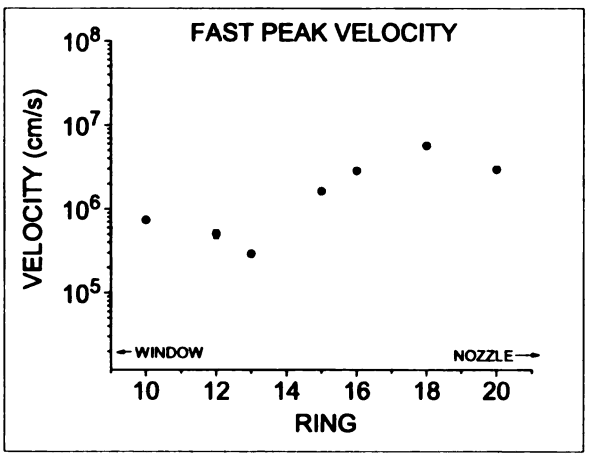

Figure 5.17: The velocity of the fast peak as a function of target position. The direction of the window and nozzle in the gas cell are also shown. The error bars are smaller than the data points.

the velocity of the fast component during laser ablation in gas is on the order of the velocity of expansion into vacuum. The mean velocity of the fast peaks at different target positions is $3.2 \times 10^6 \pm 4.0 \times 10^6$ cm/s, which is on the order of the calculated velocity for a carbon target in Section 2.4.2, which was 1.8×10^6 cm/s. The apparent velocity of the fast peak increases as the ablation target moves closer to the exit nozzle, as shown in Figure 5.17, which implies that there may be a slight interaction with the gas when the ions travel through more of the gas cell.

The exponential peak was subtracted from the data, as shown in Figure 5.18, leaving the slow, or thermal peak. A double thermal peak was observed when the

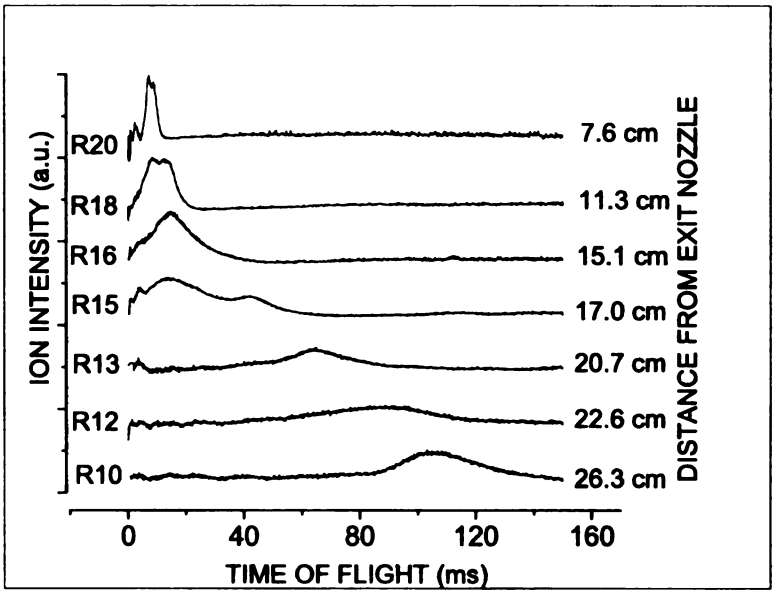

Figure 5.18: Time-of-flight spectra as a function of ablation target position in the gas cell normalized to the exponential peak. The ion intensity is arbitrary. Each spectrum is separated by a constant factor for viewing.

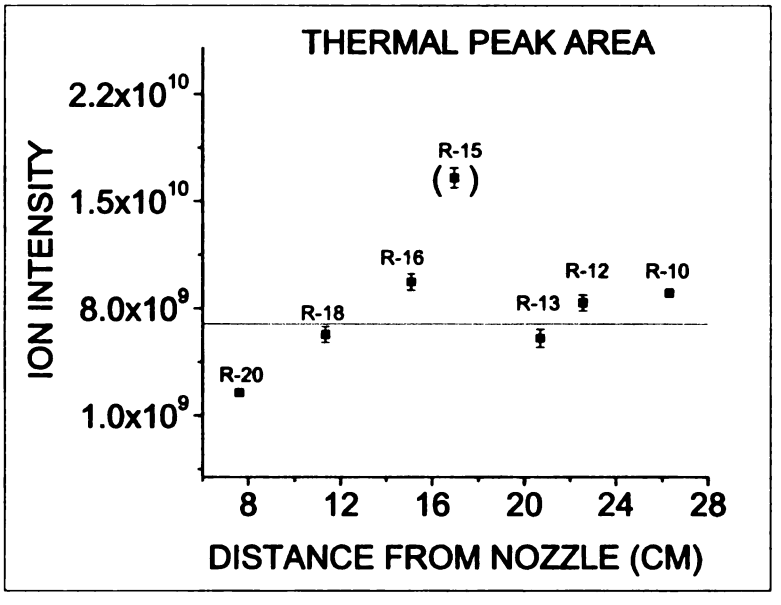

Figure 5.19: The integrated thermal area as a function of distance from the gas cell exit nozzle. The dashed line shows the average of the values without Ring 15.

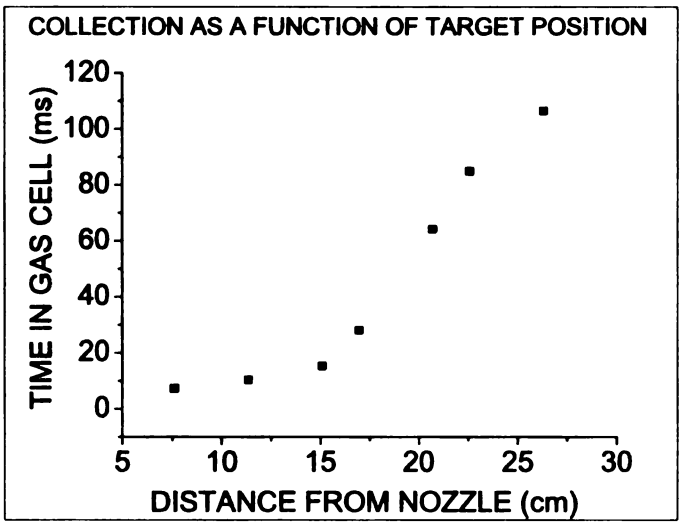

Figure 5.20: The Gaussian centroid from the fit of the thermal peak as a function of distance from the gas cell exit nozzle.

target was located at Ring 15 (17.0 cm from the nozzle) that is most likely the result of the ablation of additional material near Ring 15. During the ablation studies of carbon discussed earlier in Section 5.4.1, the target position was kept at Ring 15. The ablation of carbon in gas creates a large amount of fibrous material, so there was additional material in this region (which was clearly seen after removing the target assembly from the rings). The data at target positions Ring 18 and Ring 20 also demonstrated small double thermal peaks of very narrow widths. The integrated areas of the thermal Gaussian peaks can be compared in Figure 5.19. In general, the ion intensity contained in each thermal peak was approximately constant. Due to interactions with the fibrous material in the vicinity of Ring 15, which created a double peak, the ion intensity was larger when the ablation target was at Ring 15. The Gaussian centroid from the fits to the thermal peak date is shown as a function of distance in the gas cell in Figure 5.20. The centroid value was used to determine the time spent in the gas cell by the ions and the ion mobility, which will be discussed in Section 5.4.3.

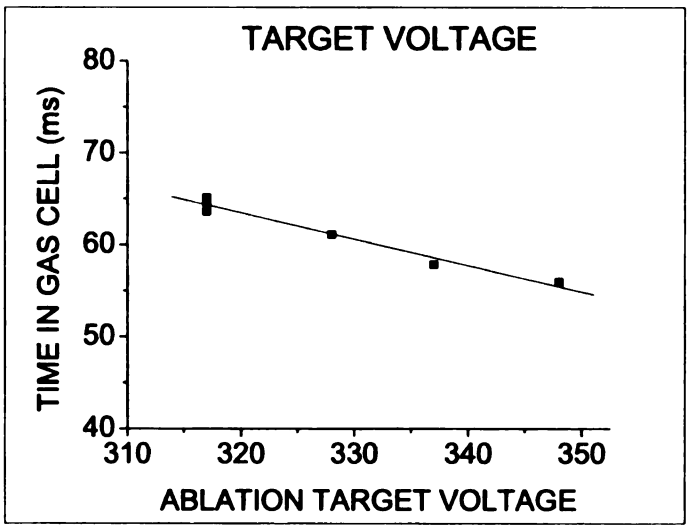

Figure 5.21: The centroids of the Gaussian distributions as a function of target voltage showing the amount of time in the gas cell. As the target voltage increases, the ions leave the gas cell faster.

Ion Drift as a Function of Target Voltage

The target voltage was varied within a constant applied electric field. The voltage file used was ...laser_50.set. The target was positioned at ring 13 and the laser fluence was 1.4 J/cm^2. The voltage at Ring 13 is + 318 V in this potential gradient. The data from varying the target voltage were fit with Equation 5.2 using the same method described earlier and the exponential peak was subtracted from the data. The centroids of the Gaussian peak fit are shown as a function of target voltage in Figure 5.21. The larger the target voltage, the faster the ions were found to exit the gas cell. In addition, the integrated Gaussian areas are shown in Figure 5.22, which shows that the ion intensity as a function of target voltage is fairly constant. The results differed from the SIMION calculations discussed in Section 3.1.2, where the ion transport was predicted to be very sensitive to the target voltage. Since SIMION does not take plasma effects into account, which are greatest in the target region, the discrepancy is not surprising. The result of this measurement demonstrates that the ion transport is not as sensitive as predicted to the target voltage. However, an increase in the target voltage does cause

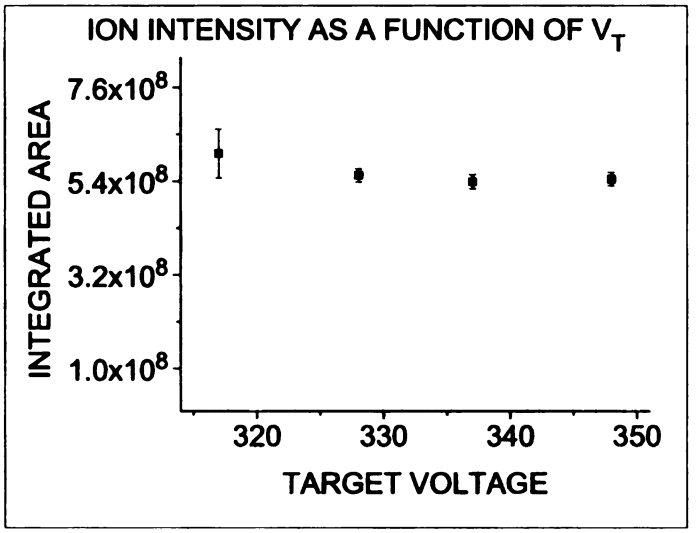

Figure 5.22: The integrated area of the Gaussian fit, corresponding to the total ion intensity, as a function of target voltage. The ion intensity as a function of target voltage is fairly constant.

ions to leave the gas cell more quickly.

5.4.3 Discussion and Significance of Collection Studies

Plume Splitting

During the collection studies of the ions created with the laser ablation system, a temporally split plume was observed, an effect that is common during laser ablation in gas [61,65,101-103]. Plume splitting in the presence of a gas is not well-understood [104], but there are a few possible explanations for the observed phenomenon. When the nanosecond laser pulse interacts with the carbon target, a layer of high-pressure partially-ionized material is formed. The layer of plasma has a higher pressure than the ambient pressure of 200 Torr. The pressure gradient forces the fast ions to leave the target holder at velocities near that for propagation in vacuum, as shown in Figure 5.17. The leading edge of the plume contains fast electrons and ions and can scatter the background gas [105] and in addition, can produce ambient plasma [106]. Another contribution to the fast component is the interaction of the stray

and reflected laser light with the chamber surfaces. The stray light can release ions from surfaces throughout the chamber and is not localized in the target region. Both factors contribute to the exponential distribution, to which the remaining data were normalized, as previously mentioned. The trapped parts of the plume, or the inner-plume layers, behind the leading edge become thermalized by the buffer gas [103]. The slower component then drifts through the helium forming the distance-dependent peak distribution.

5.4.4 Drift Time Measurements in the Gas Cell

The amount of time for the ions (in the thermal peak) to travel through the gas cell to the LEBIT microchannel plate (MCP) detector at BOB 3 was determined from the ion collection studies in the gas cell. The ions in this thermal peak originating from the laser ablation of a carbon target in the gas cell were carbon clusters. Unlike the ablation studies of carbon in the HV chamber discussed previously, carbon clusters were detected from the gas cell laser ablation studies. The carbon cluster ions will be discussed further in Section 5.4.6. The distance from the exit nozzle of the gas cell to the MCP at BOB3 was 648 cm (see Figure 5.1). This distance can be divided into three regions: the gas cell, Cross A through C, and the transport section. The gas cell is a region of ion drift with gas flow and a background pressure of 200 Torr (for these tests). Cross A is the region where the large roots-blower pump removes the helium gas and ions exit the nozzle and enter the RFQ structure. Finally, the transport region, from Cross C to BOB 3 is under vacuum conditions, and the ions have been accelerated to a kinetic energy of approximately 5 keV. The total time to travel from production in the target in the gas cell to BOB3 was measured by observing the time the ions arrived relative to the laser pulse. The drift in the gas cell dominates the total time.

The time for the ions to travel from the exit nozzle to 0.8 m into the RFQ system was calculated in a simulation code including collisions by S. Schwarz for 1000 ions of

Table 5.7: Time for ions to travel through the gas cell.

Ring Number	Distance from Nozzle (cm)	Time to exit cell (ms)
10	26.3	106.6
12	22.6	85.0
13	20.7	64.2
15	17.0	28.1
16	15.1	15.3
18	11.3	10.3
20	7.6	7.3

mass 41 amu and a background pressure of 0.1 mbar [107]. The mass of the ions was chosen to be 41 amu, which was a large peak in the time-of-flight spectrum (discussed below). The weighted average of the distribution gave 623 μs. The time to travel from 0.8 m in the RFQ (this is the Cross C region) to BOB 3 was calculated to be only 37 μs for an ion of mass 41 amu and a beam energy of 5 keV. Thus the estimated total time after the nozzle was 660 μs, while the measured transport time was at least an order of magnitude higher. The 660 μs was subtracted from the measured total time to obtain the time for the ions to travel through the gas cell starting at various positions, and is shown in Table 5.7. The measured time to exit the gas cell is longer than the SIMION calculations, which are shown in Table 5.8. For example, when the target is located at Ring 18, the measured time to exit the gas cell is 10.3 ms, while the calculated time from SIMION is 5.1 ms. The calculated value is shorter, most likely due to the smaller masses of the ions in SIMION, which were 38 amu. A mass of 38 amu was used for the SIMION simulations since this corresponds to a possible hydrocarbon cluster during the ablation of carbon (the hydrocarbon clusters will be discussed below). The mass distribution of the ablated material in the thermal, or slow peak ranged from approximately 40 to 60 amu (which will also be discussed below), which would account for the longer time for these ions to travel through the gas cell compared to the SIMION calculations.

Table 5.8: Time for ions to travel through the gas cell calculated using SIMION.

Ring Number	Distance from Nozzle (cm)	Time to exit cell (ms)
17	13.2	7.9
18	11.3	5.1
19	9.5	2.4
20	7.6	0.7
21	5.7	0.2

5.4.5 Ion Mobility Measurements in the Gas Cell

Another interesting parameter determined in the ion collection measurements is the ion mobility. The ion mobility, K, is a measure of the velocity of gas-phase ions traveling through a gas-filled drift cell with an applied electric field. As mentioned in Section 3.2, the ions are accelerated by the electric field, yet are slowed by collisions with the buffer gas. The ion mobility is also useful to determine the appropriate electric field gradient in order to force the ions out of the gas cell in a certain amount of time. The value of the ion mobility in the gas cell for carbon clusters created during the laser ablation of a carbon target in 200 Torr helium is shown in Table 5.9. In addition, the values of K for a variety of ion species in 200 Torr helium are shown for comparison. The value of K is dependent on the collision cross-section, which is dependent on the molecular structure [71]. The ion mobility value for the carbon clusters in this work fit within the range of values for the ion mobility of other species in helium gas.

5.4.6 Species Detected from Ablation

During the ablation of a Sigradur^{TM} target in 200 Torr helium at a laser fluence of 0.28 J/cm^2, a variety of masses were seen as shown in the time-of-flight spectrum as shown in Figure 5.23. The time-of-flight spectrum is a low-resolution mass spectrum and only the mass number can be determined, but not the actual identity of the species. The calibration for the time-of-flight spectra was done using the LEBIT ion source, with argon or krypton ions. A number of time-of-flight spectra were obtained,

Table 5.9: Ion mobility comparison of ions in 200 Torr He gas. The carbon clusters are measured from the present work and the other ions are literature values.

Ion	Mass (amu)	K(cm^2/Vs)
C clusters	50-100	28.2 ± 3.9
He^+ [73]	4	43
N_2^+ [73]	28	79
O_2^+ [73]	32	87
Rb^+ [73]	85	84
U^+ [73]	238	67
C_{82}^+ [108]	984	15

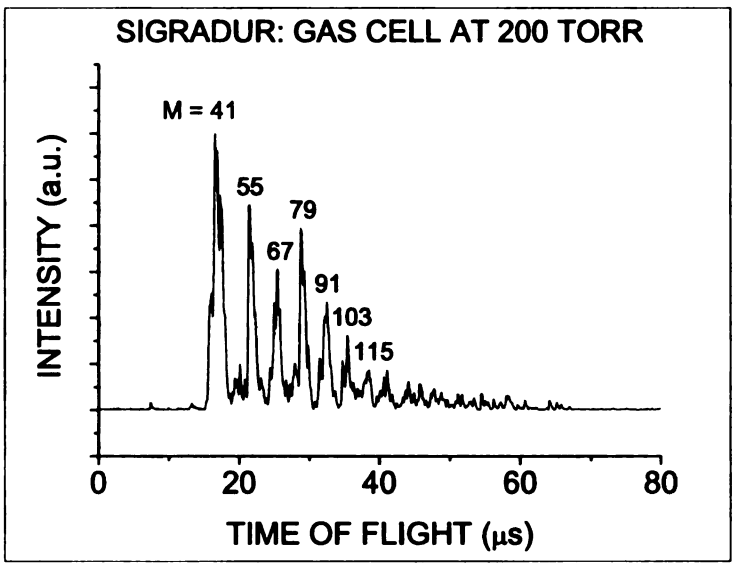

Figure 5.23: A typical time-of-flight spectrum during the ablation of Sigradur^{TM} in the gas cell, taken at BOB5 is shown. The low-resolution spectrum only provides the mass number.

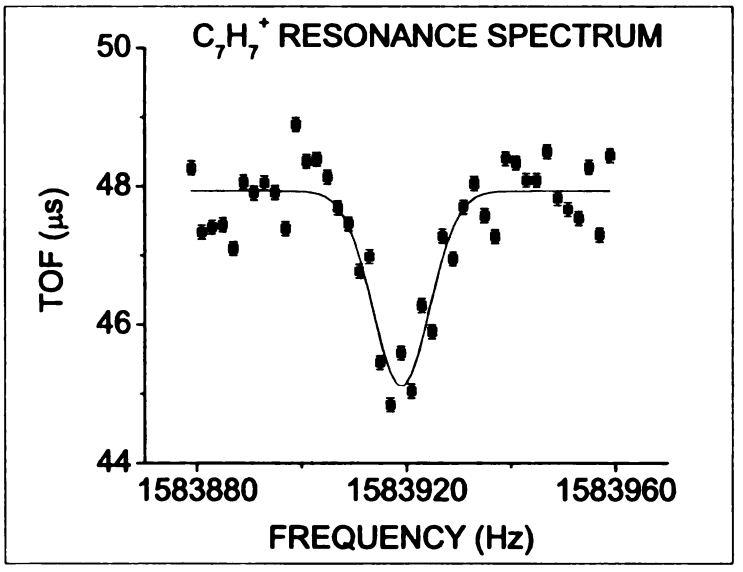

Figure 5.24: A Penning tap resonance spectrum for $C_7H_7^+$

all of which contained peaks that were generally separated by 12 amu. In order to exactly identify the constituent ions in the spectra, the Penning trap was used. The Penning trap provides a high-resolution mass spectrum. The detected ions were carbon clusters, which were not seen under vacuum conditions, as discussed previously. One such resonance spectrum is shown in Figure 5.24 from the $C_7H_7^+$ (m/z = 91) cluster. The clusters identified using the Penning trap are listed in Table 5.10. The strongest ions were generally hydrocarbons ($C_nH_{n+x}^+$) but were not lone carbon clusters. The carbon clusters seen by the ISOLTRAP collaboration for the ablation of Sigradur^{TM} under vacuum conditions were lone carbon clusters [37].

As mentioned, hydrocarbon clusters are often seen during the ablation of a carbon target. The advantage of carbon clusters over the single carbon ions detected in the HV test chamber was that the mass of the clusters spanned a large mass range, as seen in Table 5.10. The mechanism for the formation of these hydrocarbon clusters is proton transfer. In an ionized helium environment, the dominant mechanism for the formation of positive ions is proton attachment [72]. Since helium has a very high ionization potential, any helium ions created by the laser ablation-created plasma

Table 5.10: Clusters identified by resonance studies in the Penning trap.

Species	Mass
$C_3H_5^+$	41
ArH^+	41
$C_4H_7^+$	55
$C_4H_9^+$	57
$C_5H_7^+$	67
$C_6H_7^+$	79
$C_7H_7^+$	91
$C_7H_9^+$	93
$C_8H_9^+$	105

will transfer their charge to any species, including H_2, in the background. In addition, any metastable helium can ionize most species in the system, including the hydrogen and/or water present in any vacuum system, particularly a vacuum system recently exposed to air. Therefore, the hydrocarbon clusters identified in Table 5.10 are most likely due to charge exchange, and protons from the hydrogen and/or water are attached to the carbon clusters.

5.4.7 Species Present as a Function of Pressure

The ion intensity as a function of pressure during the ablation of a carbon target was discussed in Section 5.4.1. An increase in pressure resulted in an increase in the detected ion intensity. The species detected during the measurements did not change, as shown in the time-of-flight spectrum in Figure 5.25. The relative intensity of the thermal peak components did change slightly, as shown in Figure 5.26. Similar to results in the literature [106], the peaks in the time-of-flight spectrum broaden slightly with an increase in pressure. However, the identity of the species present in the time-of-flight spectrum does not change with pressure.

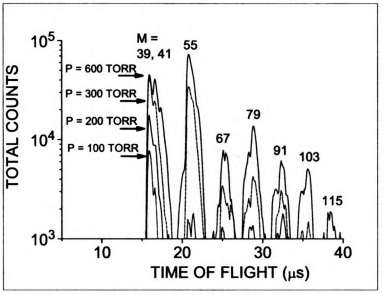

Figure 5.25: The time-of-flight distribution for different pressures during the ablation of a carbon target.

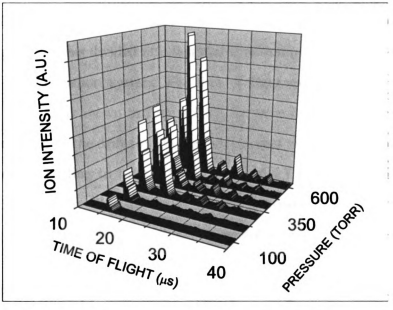

Figure 5.26: The species distribution for the ion intensity as a function of pressure.

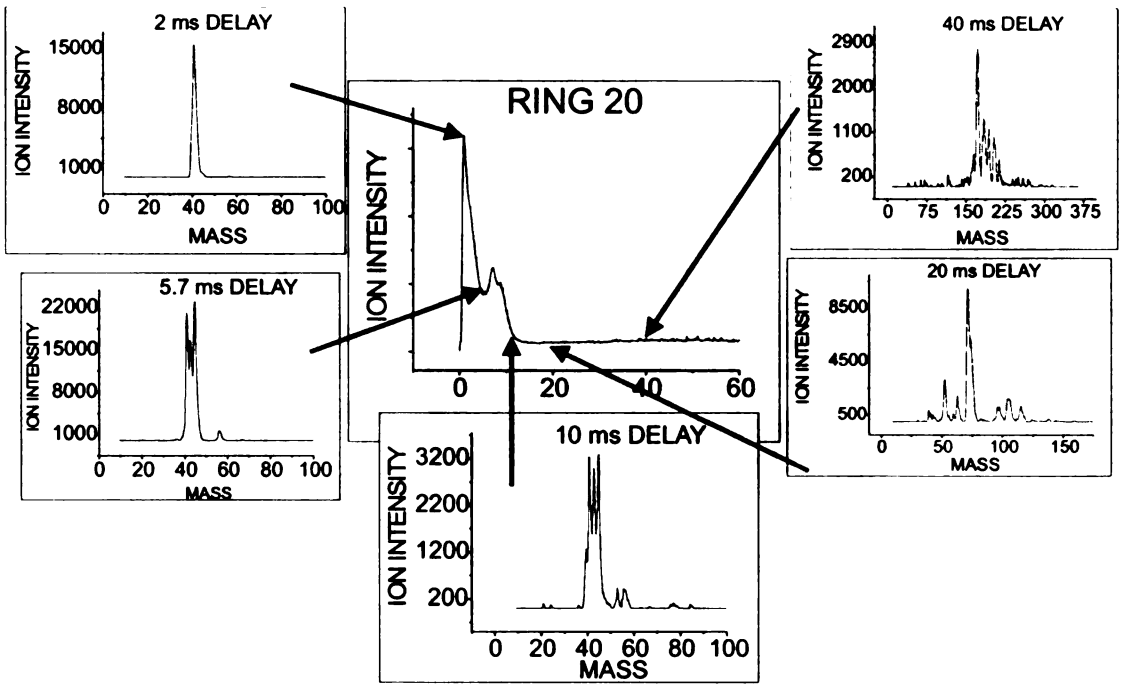

Figure 5.27: The different components of the plume separated by mass in the time of flight spectra. Note that the axes are different.

5.4.8 Species Present in the Fast and Thermal Plume Components

For the ion collection studies in the gas cell when the split plume was observed, the time of flight spectrum was divided into fast and slow components using a time gate in the LEBIT beam transport system. The time of flight spectrum when the target was located at Ring 20 is shown in Figure 5.27, for several time slices. Figure 5.28 illustrates a mass shift as the drift time increased. In other words, the fast component of the plume, corresponding to time cuts at 2 ms and 5.7 ms, contains lower mass species from approximately 40 to 50 amu, while the thermal component, corresponding to time cuts at 10 ms, 20 ms, and 40 ms, contains higher mass species, 39 to 216 amu. The dominant peak in the fast component was identified by the Penning trap as ArH^+ [109]. As mentioned, the leading edge of the plume contained fast electrons and ions, which most likely ionized argon gas, which is a trace contaminant of the helium in the gas cell. The thermal component contained the carbon clusters

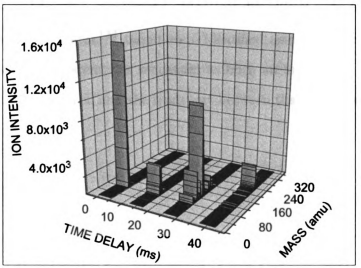

Figure 5.28: The mass distribution as a function of time cut for the ion collection at Ring 20.

identified by the Penning trap in Table 5.10.

5.5 Summary

The laser ablation system was used in the gas cell to produce a variety of ions for LEBIT using iron, copper, and Sigradur^{TM} targets. During these studies, it was found that increasing pressure in the gas cell results in increased ion production. An increase in laser fluence also increased the detected ion intensity. A series of ion collection measurements were done with a Sigradur^{TM} target using the laser as the start-signal for time-of-flight measurements. The effects of the potential gradient, the voltage applied to the target, and the position of the ablation target were also determined. By changing the position of the ablation target in the gas cell, the ion mobility of ions traveling through the gas cell and the time for ions to leave the gas cell were determined. These values were compared to the predicted behavior of the

gas cell. The comparisons were generally good although the transport of ions was not as sensitive to voltage changes as predicted in SIMION. Finally, the clusters created during the ablation of a Sigradur^{TM} target were identified using the Penning trap. The gas cell laser ablation system was successful as both an ion source for LEBIT and for characterizing the gas cell and the transport between the gas cell and LEBIT system.

Chapter 6

Summary

A laser ablation system was developed, characterized and implemented into LEBIT. Although other laser ablation systems exist at other radioactive beam facilities, this system is unique in that it involves laser ablation in a buffer gas and has a very different geometry. The laser ablation was not the primary ion source for LEBIT calibrations. As mentioned, a stable noble gas ion source close to the Penning trap was useful for frequent calibrations, particularly of the magnetic field of the Penning trap. However, the laser ablation system provided a broad mass range source of ions originating at the gas cell. This system was used as an ion source to characterize the gas cell and the transport to LEBIT.

A HV laser ablation system was built and utilized to study the laser ablation process. The target assembly was portable to allow the system to be implemented into virtually any chamber with a 114 mm conflat port. In the laser ablation studies in vacuum, seven different target materials (carbon, aluminum, iron, copper, silver, gold, and zinc) were detected and the isotopic abundance and mass loss of this collection of targets were determined, demonstrating the utility and sensitivity of the system. The effect of various parameters including the potential gradient and laser fluence on the ablation yield was also determined. The ion intensity increased as a function of laser fluence until a saturation point was reached, further confirming literature results. In

addition, the laser ablation system under vacuum conditions was also found to be stable. Calculations were performed to approximate various aspects of the system such as the expected heat conduction into the target and the approximate velocity and length of the plume. In addition, SIMION was used to model the ion trajectories as a function of various parameters including the potential gradient. In general, the simulations done in SIMION compared well to the experimental results, although the experimental results were not as sensitive to changes in the potential gradient and target voltage as the simulations in SIMION.

The laser ablation system was installed in the gas cell to be used as an ion source for LEBIT. Iron, copper, and Sigradur^{TM} targets were ablated, and the effects of the laser power and the gas cell pressure on the ablation yield were determined. In addition, the laser was used for a series of time-of-flight measurements in LEBIT, which were used to determine the time for ions to travel through the gas cell and for determining the ion mobility of the ions traveling through a buffer gas. The laser ablation of a Sigradur^{TM} target in helium buffer gas in the gas cell resulted in carbon clusters, unlike the ablation studies in the HV system during which only single carbon ions were detected. The advantage of the carbon clusters was the broad mass range of the clusters, compared to lone carbon ions. Overall, the laser ablation system was successful as a LEBIT ion source and for characterizing the gas cell, and in addition, can be used in future applications.

6.1 Future Considerations

The laser ablation system is fairly easy to implement and could be used as an ion source for various studies. One of the future experiments in LEBIT is a laser spectroscopy station, which would be used to study the structure of exotic nuclei. The laser ablation system could be used as an ion source for creating stable ions for spectroscopic measurements and calibrations when the rare isotope beam is not available.

Another possible application of the laser ablation system is an ion source for the future gas cell, which would work using the principles of a rf-carpet [110]. The design of this gas cell could incorporate a permanent location for a laser target that would not require the vacuum to be opened (in general, except for a possible target change). Targets could even be on a movable revolving target holder so the targets could easily be changed without opening the system. Implementing the laser ablation system in the new gas cell would provide a good diagnosis of the system, but it is not necessary that it be located on the beamline. Instead, the ions from the laser ablation source could be created in the same proposed area as a fission source (see [110]), with the advantage of a start signal for timing measurements.

A laser ablation ion source can also be used to evaporate materials into a ECR ion source plasma [27] rather than using an externally heated oven. This has various advantages including fairly high efficiency regarding the usage of the material and relative simplicity. These are a few future possibilities for this laser ablation ion source, which can be incorporated into almost any system needing a variety of test ions.

Appendix A

Data Tables

Data tables of compiled values from the literature that were used in various calculations in the present work are provided. The data are separated into three different tables, Tables A.1, A.2 and A.3, and the main source of data is the CRC Handbook [111], except where noted. Selected physical and chemical bulk properties are given in Tables A.1 and A.2, while the optical properties of the target materials are given in Table A.3.

Table A.1: Target data properties. All values were obtained from [111], except where noted. The unknown data for Sigradur-G is substituted with known graphite data, and denoted by ^{*g}.

Target	$\rho(g/cm^3)$	$T_{fus}(K)$	$T_{vap}(K)$	$c_p(J/gK)$
Al	2.70	933	2792	0.897
Au	19.3	1337	2835	0.129
Fe	7.87	1808	3129	0.449
Ag	10.5	1234	1180	0.235
Zn	7.14	693	2435	0.388
Cu	8.96	1356	3134	0.385
Sigradur-G	1.42 [112]	3800^{*g}	4300^{*g}	0.709^{*g}

Table A.2: Target data properties. The coefficient of linear expansion α, the thermal conductivity κ, the first ionization energy IE and the electron work function Φ are provided. All values were obtained from [111], except where noted. The unknown data for Sigradur^{TM}-G is substituted with known graphite data, and denoted by ^{*g}.

Target	$\alpha(\times 10^6 K^{-1})$	$\kappa(W/cmK)$	$IE(eV)$	$\Phi(eV)$
Al	23.1	2.37	5.99	4.2
Au	14.2	3.17	9.23	5.5
Fe	11.8	0.80	7.90	4.7
Ag	18.9	4.29	7.58	4.6
Zn	30.2	1.16	9.39	3.6
Cu	16.5	4.01	7.73	5.1
Sigradur-G	2.7 [112]	0.063 [112]	11.26 ^{*g}	-

Table A.3: Target Optical Data at 2.3 eV photon energy. The index of refraction n, the extinction coefficient k, and the normal incidence reflection R as a function of a photon energy of 2.3eV (532 nm) are provided. All values were obtained from [111], except where noted. The unknown data for Sigradur^{TM}-G is substituted with either known graphite data, denoted by ^{*g}, or amorphous carbon, denoted by ^{*a}.

Target	n	k	R
Al	0.92	6.57	0.92
Au	0.37	2.20	0.76
Fe	2.65	3.34	0.57
Ag	0.24	3.09	0.91
Zn	0.77	3.91	0.83
Cu	1.04	2.59	0.62
Sigradur-G	2.34 ^{*a} [113]	0.85 ^{*a} [113]	0.28 ^{*g} [114]

Appendix B

Optical Emission Spectrometry (OES) Measurements

B.1 Introduction to OES

Optical Emission Spectroscopy (OES) involves the measurement/ detection of optical radiation emitted from excited atoms/ ions. For plasma diagnostics, including plasmas created in helium gas (helicon plasmas), OES provides an excellent method to obtain information such as the electron temperature and electron density [115]. The electron temperature of the helicon plasma, T_e can be determined by the relative line intensities and tabulated values [116]:

$$\frac{I}{I'} = \left(\frac{\lambda'}{\lambda}\right)^3 \frac{g_n}{g_u} . \frac{f_{mn}}{f_{vu}} \exp\left(-\frac{E_m - E_v}{kT_e}\right), \tag{B.1}$$

where the upper and lower levels of the first line are labeled m and n, while the upper and lower levels of the second line are labeled v and u, respectively. In Equation B.1, I and I' are the measured line intensities, λ and λ' are the wavelengths of the lines, g_n and g_u are the statistical weights or degeneracies of the lower energy levels, f_{mn} and f_{vu} are the absorption oscillator strengths of the transitions, and E_m and E_v are

Table B.1: Helium OES parameters

Line	$g \times f$ [119]	E(upper) (eV) [120]	Transition [120]
728	0.145	22.92	$3^1S \rightarrow 2^1P$
706	0.625	22.72	$3^3S \rightarrow 2^3P$

the energies of the upper levels.

B.2 OES Gas Cell Measurements

An Ocean Optics USB-2000 spectrometer was used to characterize the discharge in the gas cell. However, after the background was subtracted from the obtained spectra, no peaks were present. Most likely, the line intensity was too low to detect. The spectrometer was also used to study the plasma created in Cross A at low helium pressures (see Figure 5.1 for an overview of LEBIT). A spectrum was obtained and the background was subtracted, as shown in Figure B.1. The helium lines were used to determine T_e using Equation B.1. The helium line ratio 728/706 was used to approximate the electron temperature, since this ratio is dependent on T_e [115, 117, 118]. The 728 nm is due to the $3^1S \rightarrow 2^1P$ transition and the 706 nm line is due to the $3^3S \rightarrow 2^3P$ transition. The literature values are summarized in Table B.1. From this ratio, T_e in Cross A during the discharge was determined to be $1.3{\times}10^3$ K or 0.11 eV.

The OES measurements could also be used when the fast ion beam produced at the NSCL is thermalized in the gas cell. If the intensity of the transitions of both the radioactive ions and the helium ions are large enough to detect with a simple spectrometer, OES could be used as a method to determine which species are in the plasma, in addition to the temperature and density of this plasma, following the method discussed here. An optical set-up to focus the emission intensity could be achieved by coupling a spherical lens, iris and fiber optic to a window on the gas cell. An additional consideration would be to mount the spectrometer on the gas cell and

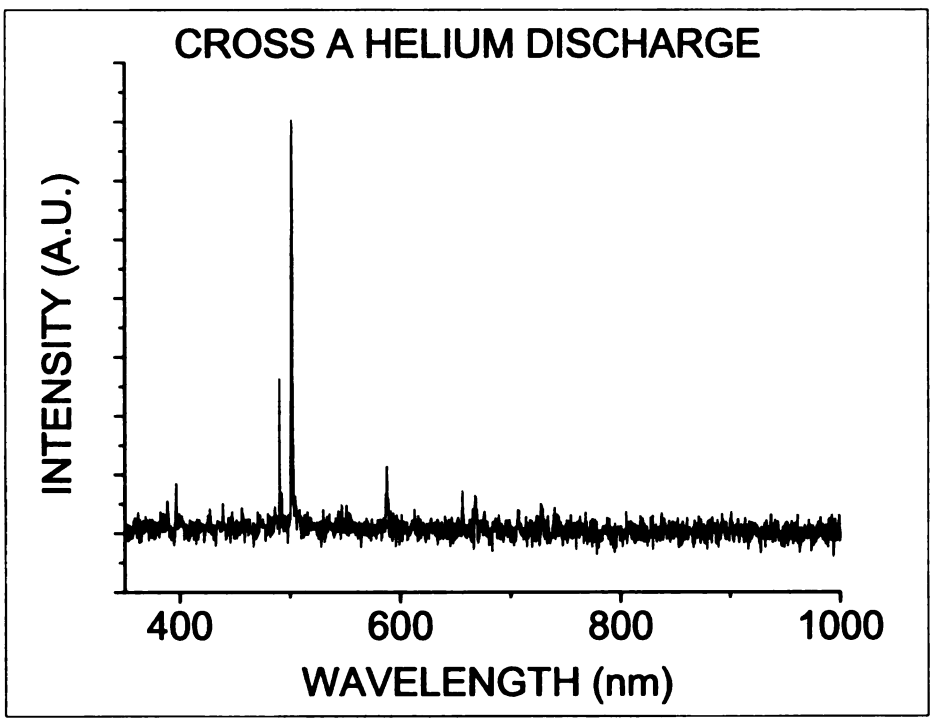

Figure B.1: The Cross A discharge data obtained by the spectrometer.

to be able to set-up the OES data acquisition outside of the vault area.

B.3 OES Applications

This method of plasma diagnostics is also applicable for the laser ablation system [47, 48] . As discussed in Chapter 2, a plasma is created during laser ablation in a vacuum or gas. The current HV system set-up does not include a window that could be used for OES. On the other hand, the gas cell does have a window that could be used for OES. In order to use OES during laser ablation, a method is needed to filter the 532 nm light to prevent it from saturating the spectrometer by gating out the 532 nm region in the data acquisition, or starting data acquisition at the end of the pulse. These are some future applications, which would provide a useful diagnostic of the gas cell and the laser ablation system.

Appendix C

Additional Laser Considerations

C.1 Safety Considerations

Since the laser ablation system is operated in an environment in which multiple people are present, a safety system housing the laser was necessary. The safety system implemented in the N4 vault allowed the laser to run in the open vault, without the need for goggles. It consisted of three aluminum boxes, as shown in Figure C.1. All of the access doors to the boxes were interlocked with Euchner NM02VZA safety switches, connected in series. The largest box contained the laser and the optical table holding some optics, and the two smaller boxes connected with an aluminum tube housed the mirrors and lens. When changing between ablation in the HV system and the gas cell, the upper box was rotated and the tube between the lower and upper boxes was lengthened. In addition, the wires connecting the safety switches were lengthened. In general, the safety system was relatively easy to implement, making it possible to move the entire ablation system in the future, if necessary.

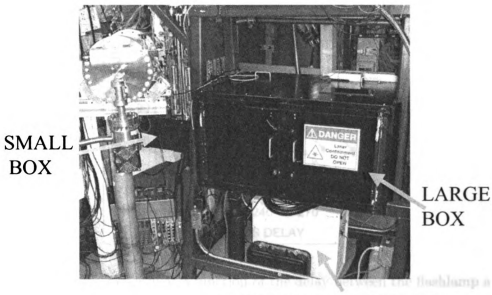

Figure C.1: Photograph of the laser ablation safety containment system. The large box housing the laser and optical table is shown, in addition to the small box containing the raster-scan mirror. The other small box containing a mirror and lens is not visible.

C.2 Laser-Induced System Modifications

Operating a high-power laser in an enclosed area resulted in a few problems. Part of the difficulty of this laser set-up was associated with the scanning laser beam position. The first problem encountered was the HV AR-coated BK7 quartz window was ablated by the laser. When the laser hit the window edge, most likely due to a back-reflection from the target surface, the vacuum was immediately lost, which was detrimental to the RGA. The RGA electronics sustained damage from this accident and multiple components on the circuit were replaced. In order to minimize the chance of a repeat incident, the laser alignment was confirmed often, including checking the alignment at the viewport with the raster-scan system running.

Another problem encountered was the degradation of the laser energy, as shown in Figure C.2. During the time period of May 2004 to October 2004, the laser energy degraded by a large amount and the beam profile on the burn paper became asymmetric with rough edges and a localized hotspot. After checking the cavity and SHG module

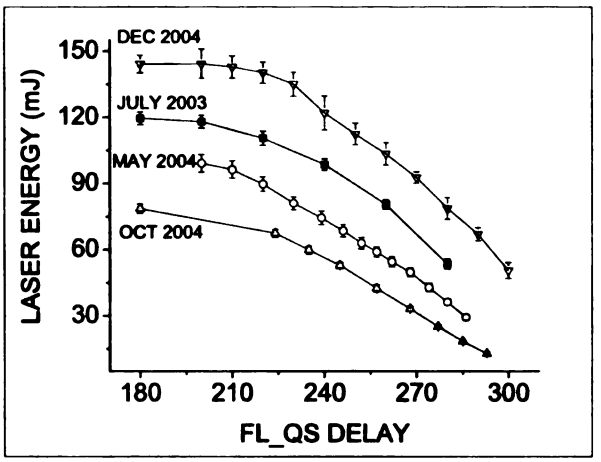

Figure C.2: The laser energy as a function of the delay between the flashlamp and q-switch. Data is given for four dates. The December data is after the laser was returned to Big Sky for repair.

for damage, the laser was returned to Big Sky (Montana) for repair. The Pockels Cell had been damaged severely by back-reflected light. It was replaced in December 2004 and the laser energy was stable and higher intensity again (see Figure C.2). The half waveplate (HWP) and optical isolator (OI) combination (Section 4.3.4) were then obtained to act as a one-way light valve to counteract this problem. The HWP and OI combination also provided a method to lower the laser energy without changing the beam profile.

C.3 Beamsplitter Calibrations

The calibration of the three beamsplitters is provided in this section. The 90% transmittance/ 10% reflectance and 80% transmittance/ 20% reflectance beamsplitters were ordered unpolarized. The calibration of the 90/10 beamsplitter is given in Figure C.3 and the calibration of the 80/20 beamsplitter is given in Figure C.4. The measured transmitted and reflected percentages for various beamsplitters are given in Table C.1. The 532 nm laser light is s-polarized (or vertical with respect to the baseplate). Therefore, the distribution of the reflected and transmitted light differed

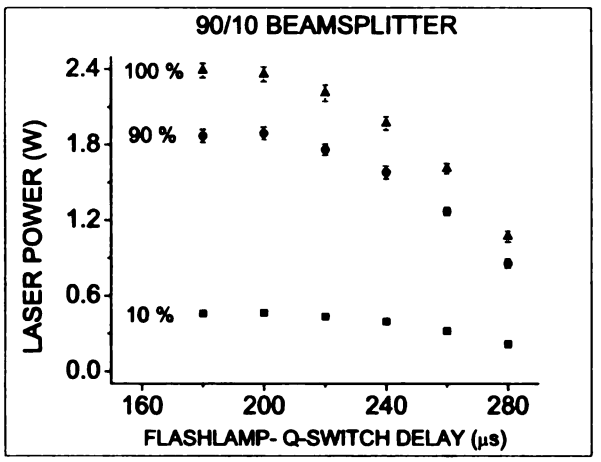

Figure C.3: Calibration of 90/10 beamsplitter.

Table C.1: Beamsplitter parameters.

BS (T/R)	Polarization	Cal. % Transmitted	Cal. % Reflected
90/10	UNP	79.5	19.7
80/20	UNP	66.6	31.3
2/98	S	1.1	98.9
80/20	UNP (OI and HWP)	77.0	18.3

from the specifications. Since s-polarized light demonstrates a higher reflectance than p-polarized light, the percent reflectance was greater, and the percent transmittance was less during the calibrations (since the correct polarization was not ordered). The s-polarized 2% transmittance/ 98% reflectance beamsplitter was ordered to greatly decrease the laser energy for the ablation of Sigradur^{TM}-G (Section 4.3.6). The calibration is shown in Figure C.5 and the measured transmittance/reflectance is shown in Table C.1. Finally, once the HWP/OI combination was obtained, the polarization was changed from s to p (after the HWP) and then from p to circular (after the OI), and the new calibration for the 80/20 beamsplitter is shown in Figure C.6. The transmittance/reflectance ratio is 77:18, which is closer to the expected value of 80:20. The beamsplitters were used to divert some laser energy to the power meter. These calibrations provide the ratios of the transmittance/reflectance used to determine the amount of laser energy incident on the target.

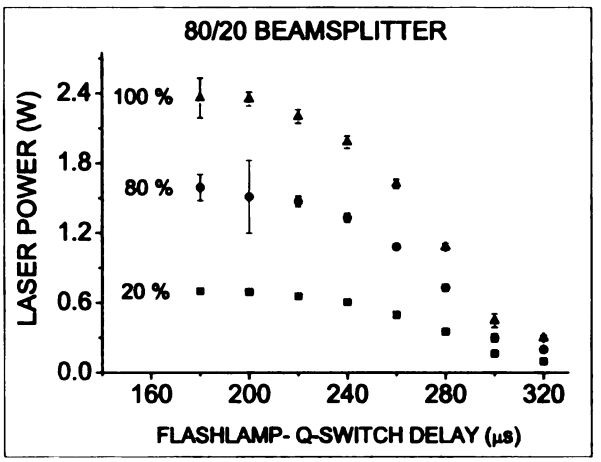

Figure C.4: Calibration of 80/20 beamsplitter.

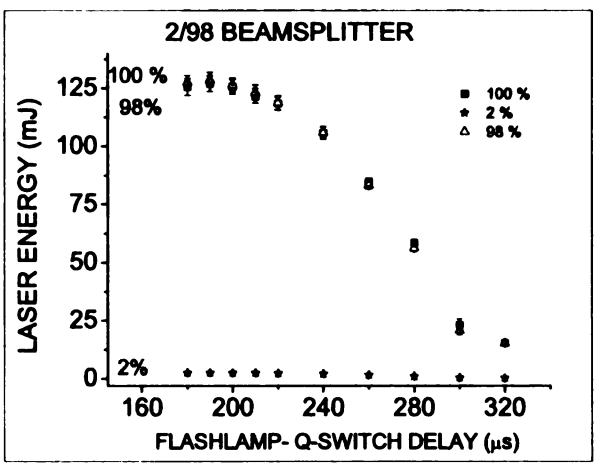

Figure C.5: Calibration of 2/98 beamsplitter.

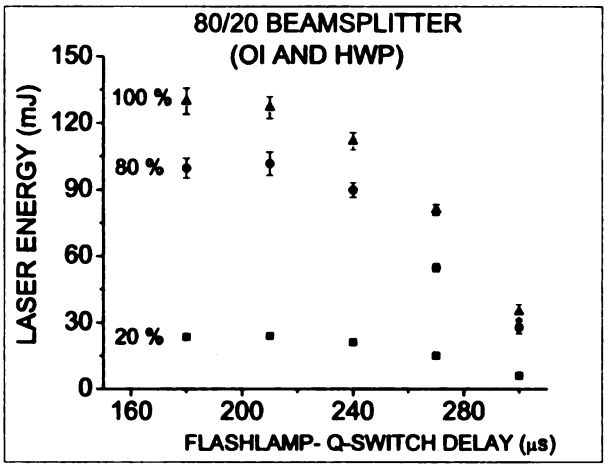

Figure C.6: Calibration of 80/20 beamsplitter after the installation of the HWP/OI.

Bibliography

[1] P. Miller, F. Marti, D. Poe, M. Steiner, J. Stetson, A. Stolz, and P. Zavodsky. Status of the Coupled Cyclotron Facility at NSCL. In *Proceedings of the 17th Conference on Cyclotrons and Their Applications*, 2005.

[2] D. Lunney, J. M. Pearson, and C. Thibault. *Reviews of Modern Physics*, **75**:1021, 2003.

[3] G. Bollen. *Nucl. Phys. A*, **626**:297, 1997.

[4] G. Bollen, S. Becker, H.-J. Kluge, M. König, R. B. Moore, T. Otto, H. Raimbault-Hartmann, G. Savard, L. Schweikhard, and H. Stolzenberg. *Nucl. Instr. and Meth. A*, **368**:675, 1996.

[5] K. Blaum, G. Bollen, F. Herfurth, A. Kellerbauer, H.-J. Kluge, M. Kuckein, E. Sauvan, C. Scheidenberger, and L. Schweikhard. *Eur. Phys. J. A*, **15**:245, 2002.

[6] R. Ringle, P. Schury, T. Sun, G. Bollen, D. Davies, J. Huikari, E. Kwan, D. J. Morrissey, A. Prinke, J. Savory, S. Schwarz, and C. Sumithrarachchi. *Int. J. Mass Spectrosc.*, in press, 2006.

[7] D. Lunney and G. Bollen. *Hyperfine Int*, **129**:249, 2000.

[8] D. J. Morrissey, B. M. Sherrill, M. Steiner, A. Stolz, and I. Wiedenhoever. *Nucl. Instr. and Meth. B*, **204**:90, 2003.

[9] P. A. Lofy. *Development of a High-pressure Gas-filled Ion Source for a Radioactive Beam Facility.* PhD thesis, Michigan State University, 2003.

[10] L. Weissman, D. J. Morrissey, G. Bollen, D. A. Davies, E. Kwan, P. A. Lofy, P. Schury, S. Schwarz, C. Sumithrarachchi, T. Sun, and R. Ringle. *Nucl. Instr. and Meth. A*, **540**:245, 2005.

[11] L. Weissman, P. A. Lofy, D. A. Davies, D. J. Morrissey, P. Schury, S. Schwarz, T. Sun, and G. Bollen. *Nuclear Physics A*, **746**:655, 2004.

[12] L. Weissman, D. A. Davies, P. A. Lofy, and D. J. Morrissey. *Nucl. Instr. and Meth. A*, **531**:416, 2004.

[13] G. Bollen, S. Schwarz, D. Davies, P. Lofy, D. J. Morrissey, R. Ringle, P. Schury, T. Sun, and L. Weissman. *Nuclear Physics A*, **746**:597, 2004.

[14] S. Schwarz, G. Bollen, D. Davies, D. Lawton, P. Lofy, D. J. Morrissey, J. Ottarson, R. Ringle, P. Schury, T. Sun, D. Vanwasshenova, T. Sun, L. Weissman, and D. Wiggins. LEBIT - a low-energy beam and ion trap facility at NSCL/MSU. In *AIP Conf. Proc. 680: Application of Accelerators in Research and Industry*, page 1051, August 2003.

[15] J. P. Blewett and E. J. Jones. *Physical Review*, **50**:464, 1936.

[16] HeatWave Labs, Inc., Watsonville, CA, www.cathode.com.

[17] S. Amoruso, R. Bruzzese, N. Spinelli, and R. Velotta. *J. Phys. B: At. Mol. Phys.*, **32**:131, 1999.

[18] F. Breech and L. Cross. *Appl. Spectrosc.*, **16**:59, 1962.

[19] J.T. Cheung. *Pulsed Laser Deposition of Thin Films*, page 1. (John Wiley & Sons, Inc.), 1994. edited by D. B. Chrisey and G. K. Hubler.

[20] M. F. Yanik, H. N Cinar, A. Cinar, A. D. Chisholm, Y. Jin, and A. Ben-Yakar. *Nature*, **432**:822, 2004.

[21] E. N. Glezer, M. Milosavljevic, L. Huang, R. J. Finlay, T.-H. Her, J. P. Callan, and E. Mazur. *Optics Letters*, **21**:2023, 1996.

[22] M. I. Cooper, D. C. Emmony, and J. H. Larson. *Optics and Laser Technology*, **1**:69, 1995.

[23] A. J. Fernandes and D. M. Kane. *App. Phys. A*, **79**:735, 2004.

[24] A. Tsukazaki, A. Ohtomo, S. Yoshida, M. Kawasaki, C. H. Chia, T. Makino, Y. Segawa, T. Koida, S. F. Chichibu, and H. Koinuma. *App. Phys. Lett.*, **83**:2784, 2003.

[25] V. K. Kayastha, Y. K. Yap, Z. Pan, I. N. Ivanov, A. A. Puretzky, and D. B. Geohegan. *App. Phys. Lett.*, **86**:3105, 2005.

[26] H. W. Kroto, J. R. Heath, S. C. Obrien, R. F. Curl, and R. E. Smalley. *Nature*, **318**:162, 1985.

[27] R. Harkewicz, J. Stacy, J. Greene, and R. C. Pardo. *Rev. Sci. Instrum.*, **65**:1104, 1994.

[28] S. Rencheng, X. Sida, Z. Wei, Y. Rong, Z. Shuming, Y. Zipiao, Z. Zhizheng, and L. Yixiao. *Rev. Sci. Instrum.*, **68**:3027, 1997.

[29] S. Gammino, L. Torrisi, L. Andò, G. Ciavola, L. Celona, L. Láska, J. Krasa, M. Pfeifer, K. Rohlena, E. Woryna, J. Wolowski, P. Parys, and G. D. Shirkov. *Rev. Sci. Instrum.*, **73**:650, 2002.

[30] S. Gammino, L. Torrisi, G. Ciavola, L. Andò, J. Wolowski, L. Láska, J. Krasa, and A. Picciotto. *Nucl. Instr. and Meth. B*, **73**:345, 2003.

[31] R. F. Haglund, Jr. *Laser Ablation and Desorption*, page 15. (Academic Press), 1998. edited by J. C. Miller and R. F. Haglund, Jr.

[32] J. A. Carroll and R. C. Beavis. *Laser Ablation and Desorption*, page 413. (Academic Press), 1998. edited by J. C. Miller and R. F. Haglund, Jr.

[33] W. O. Schall. *Journal of Spacecraft and Rockets*, **39**:81, 2002.

[34] W. R. Plaß, A. F. Dodonov, S. A. Elisseev, H. Geissel, G. Münzenberg, Yu. Novikov, C. Sheidenberger, and Z. Wang. The time-of-flight mass spectrometer at the shiptrap facility. Gsi scientific report 2002, Gesellschaft für Schwerionenforschung, 2003.

[35] H. L. Ravn. *Nucl. Instr. and Meth. B*, **26**:72, 1987.

[36] C. Scheidenberger, G. Bollen, F. Herfurth, A. Kellerbauer, H.-J. Kluge, M. Koizumi, S. Schwarz, and L. Schweikhard. *Nuclear Physics A*, **701**:574, 2002.

[37] K. Blaum, A. Herlert, G. Huber, H.-J. Kluge, J. Maul, and L. Schweikhard. *Anal Bioanal Chem*, **377**:1133, 2003.

[38] SHIPTRAP collaboration, J. Schonfelder, D. Ackermann, H. Backe, G. Bollen, J. Dilling, A. Dretzke, O. Engels, J. Estermann, D. Habs, S. Hofmann, F. P. Hessberger, H.-J. Kluge, W. Lauth, W. Ludolphs, M. Maier, G. Marx, R. B. Moore, W. Quint, D. Rodriguez, M. Sewtz, G. Sikler, C. Toader, and C. Weber. *Nucl. Phys. A*, **701**:579, 2002.

[39] D. Dahl. *Int. J. Mass Spectrosc.*, **200**:3, 2000.

[40] S. I. Anisimov and B. S. Luk'yanchuk. *Uspekhi Fizicheskikh Nauk*, **45**:293, 2002.

[41] A. V. Bulgakov and N. M. Bulgakova. *J. Phys. D: Appl. Phys.*, **28**:1710, 1995.

[42] R. K. Singh and J. Narayan. *Phys. Rev. B*, **41**:8843, 1990.

[43] M. S. Tillack, D. W. Blair, and S. S. Harilal. *Nanotechnology*, **15**:390, 2004.

[44] R. Kelly and A. Miotello. *Pulsed Laser Deposition of Thin Films*, page 55. (John Wiley & Sons, Inc.), 1994. edited by D. B. Chrisey and G. K. Hubler.

[45] R. Kelly, A. Miotello, B. Braren, A. Gupta, and K. Casey. *Nucl. Instr. and Meth. B*, **65**:187, 1992.

[46] S. M. Park, H. Chae, S. Wee, and I. Lee. *J. Chem. Phys.*, **109**:928, 1998.

[47] D. B. Geohegan. *Pulsed Laser Deposition of Thin Films*, page 115. (John Wiley & Sons, Inc.), 1994. edited by D. B. Chrisey and G. K. Hubler.

[48] S. S. Harilal, R. C. Issac, C. V. Bindhu, V. P. N. Nampoori, and C. P. G. Vallabhan. *J. Appl. Phys.*, **81**:3637, 1997.

[49] T. Götz, M. Bergt, W. Hoheisel, F. Träger, and M. Stucke. *App. Surf. Sci.*, **96-98**:280, 1995.

[50] A. Miotello and R. Kelly. *App. Phys. A*, **69**:67, 1999.

[51] C. P. Grigoropoulos. *Laser Ablation and Desorption*, page 173. (Academic Press), 1998. edited by J. C. Miller and R. F. Haglund, Jr.

[52] R. E. Russo and X. Mao. *Laser Ablation and Desorption*, page 375. (Academic Press), 1998. edited by J. C. Miller and R. F. Haglund, Jr.

[53] J. Steinbeck, G. Braunstein, M. S. Dresselhaus, T. Venkatesan, and D. C. Jacobson. *J. Appl. Phys.*, 58:4374, 1985.

[54] L. Moenke-Blankenburg. *Lasers in Analytical Atomic Spectroscopy*, page 125. (VCH Publishers, Inc.), 1997. edited by J. Sneddon, T. L. Thiem, and Y.-I. Lee.

[55] J. F. Ready. *J. Appl. Phys.*, **36**:462, 1965.

[56] L.-C. Chen. *Pulsed Laser Deposition of Thin Films*, page 167. (John Wiley & Sons, Inc.), 1994. edited by D. B. Chrisey and G. K. Hubler.

[57] N. Bloembergen. Laser-material interactions; fundamentals and applications. In *AIP Conference Proceedings 288; Laser Ablation: Mechanisms and Applications- II.* American Institute of Physics, 1993.

[58] S. Amoruso, V. Berardi, R. Bruzzese, R. Capobianco, R. Velotta, and M. Armenante. *App. Phys. A*, **62**:533, 1996.

[59] J. J. Chang and B. E. Warner. *App. Phys. Lett.*, **69**:473, 1996.

[60] S. Amoruso, M. Armenante, V. Berardi, R. Bruzzese, and N. Spinelli. *App. Phys. A*, **65**:265, 1997.

[61] R. C. Issac, G. K. Varier, P. Gopinath, S. S. Harilal, V. P. N. Nampoori, and C. P. G. Vallabhan. *App. Phys. A*, **67**:557, 1998.

[62] G. Padmaja, A. V. R. Kumar, P. Radhakrishnan, V. P. N. Nampoori, and C. P. G. Vallabhan. *J. Phys. D: Appl. Phys.*, **26**:35, 1993.

[63] J. R. Ho, C. P. Grigoropoulos, and J. A. C. Humphrey. *J. Appl. Phys.*, **79**:7205, 1996.

[64] H. Hora. *Laser Plasmas and Nuclear Energy.* Plenum Press, New York, 1975.

[65] S. S. Harilal, P. Radhakrishnan, V. P. N. Nampoori, and C. P. G. Vallabhan. *App. Phys. Lett.*, **64**:3377, 1994.

[66] P. E. Dyer, A. Issa, and P. H. Key. *App. Phys. Lett.*, **57**:186, 1990.

[67] S. S. Harilal, C. V. Bindhu, M. S. Tillack, F. Najmabadi, and A. C. Gaeris. *J. Appl. Phys.*, **93**:2380, 2003.

[68] J. F. Ziegler, J. P. Biersack, and U. Littmark. *The Stopping and Range of Ions in Solids.* Pergamon Press, New York, 1985.

[69] S. S. Harilal, 2006. Private communication.

[70] N. M. Bulgakova, A. V. Bulgakov, and O. F. Bobrenok. *Phys. Rev. E*, **62**:5624, 2000.

[71] D. E. Clemmer and M. F. Jarrold. *J. Mass Spectrosc.*, **32**:577, 1997.

[72] R. B. Cody, J. A. Laramee, and H. Dupont Durst. *Anal. Chem.*, **77**:2297, 2005.

[73] E. W. McDaniel and E. A. Mason. *The Mobility and Diffusion of Ions in Gases.* John Wiley & Sons, Inc., New York, 1973.

[74] I. G. Lebo, Y. A. Mikhailov, V. F. Tishkin, and V. D. Zvorykin. *Laser Particle Beams*, **17**:753, 1999.

[75] D. Egorov, J. D. Weinstein, D. Patterson, B. Friedrich, and J. M. Doyle. *Phys. Rev. A*, **63**:030501, 2001.

[76] S. M. Green, A. Piqué, K. S. Harshavardhan, and J. S. Bernstein. *Pulsed Laser Deposition of Thin Films*, page 23. (John Wiley & Sons, Inc.), 1994. edited by D. B. Chrisey and G. K. Hubler.

[77] B. O'Shay, 2005. Private communication.

[78] B. Farkas and Zs. Geretovsky. On determining the spot size for laser fluence measurements. In *Proceedings of symposium J of the E-MRS Spring Meeting 2005.* European Materials Research Society, 2005. To be published.

[79] T. Lippert, 2005. Private communication.

[80] A. E. Siegman. *Lasers.* University Science Books, Mill Valley, California, 1986.

[81] K. Blaum, G. Huber, H.-J. Kluge, and L. Schweikhard. *Eur. Phys. J. D*, **24**:145, 2003.

[82] J. J. Gaumet, A. Wakisaka, Y. Shimizu, and Y. Tamori. *J. Chem. Soc. Faraday Trans.*, **89**:1667, 1993.

[83] V. Henč-Bartolić, E. Kovačević, T. Atwee, H.-J. Kunze, and M. Stubicar. *Fizika A*, **10**:215, 2001.

[84] G.M. Jenkins and K. Kawamura. *Polymeric carbons- carbon fibre, glass and char.* Cambridge University Press, New York, 1976.

[85] B. O'Malley, I. Snook, and D. McCulloch. *Phys. Rev. B*, **57**:14148, 1998.

[86] G. K. Nicolussi, A. M. Davis, M. J. Pellin, R. S. Lewis, R. N. Clayton, and S. Amari. *Science*, **277**:1281, 1997.

[87] Energy, pulse duration and stability versus q-switch delay. Technical Note TN-020801, Quantel, Les Ulis, France, 2002.

[88] J. M. Vadillo, C. C. García, and J. J. Alcántara, J. F.and Laserna. *Spectrochimica Acta B*, **60**:1027, 2005.

[89] S. Hunsche, T. Starczewski, A. L'Huillier, A. Persson, C.-G. Wahlström, H. B. van Linden van den Heuvell, and S. Svanberg. *Phys. Rev. Lett.*, **77**:1966, 1996.

[90] P. Agostini and E. Mevel. *Laser Interactions with Atoms, Solids, and Plasmas*, page 11. (Plenum Press), 1994. edited by R. M. More.

[91] S. M. Park and J. Y. Moon. *J. Chem. Phys.*, **109**:8124, 1998.

[92] A. V. Rode, S. T. Hyde, E. G. Gamaly, R. G. Elliman, D. R. McKenzie, and S. Bulcock. *App. Phys. A*, **69**:755, 1999.

[93] F. Dahmani and T. Kerdja. *Phys. Rev. A*, **44**:2649, 1991.

[94] L. Torrisi, S. Gammino, L. Andò, V. Nassisi, D. Doria, and A. Pedone. *App. Surf. Sci.*, **210**:262, 2003.

[95] H. Weick, H. Geissel, C. Scheidenberger, F. Attallah, T. Baumann, D. Cortina, M. Hausmann, B. Lommel, G. Münzenberg, N. Nankov, F. Nickel, T. Radon, H. Schatz, K. Schmidt, J. Stadlmann, K. Sümmerer, M. Winkler, and H. Wollnik. *Nucl. Instr. and Meth. B*, **164**:168, 2000.

[96] G. Bollen, S. Schwarz, D. Davies, P. Lofy, D. Morrissey, R. Ringle, P. Schury, T. Sun, and L. Weissman. *Nucl. Instr. and Meth. A*, **532**:203, 2004.

[97] G. Bollen. Ion traps –Precision measurements and more. In *Exotic Nuclei and Atomic Masses*, page 411, 2003.

[98] S. Schwarz, G. Bollen, D. Lawton, P. Lofy, D. J. Morrissey, J. Ottarson, R. Ringle, P. Schury, T. Sun, V. Varentsov, and L. Weissman. *Nucl. Instr. and Meth. B*, **204**:507, 2003.

[99] G. Bollen and S. Schwarz. *Nucl. Instr. and Meth. B*, **204**:466, 2003.

[100] G. Bollen, D. Davies, M. Facina, J. Huikari, E. Kwan, P. A. Lofy, D. J. Morrissey, A. Prinke, R. Ringle, J. Savory, P. Schury, S. Schwarz, C. Sumithrarachchi, T. Sun, and L. Weissman. *Phys. Rev. Lett.*, in press, 2006.

[101] S. S. Harilal, C. V. Bindhu, M. S. Tillack, F. Najmabadi, and A. C. Gaeris. *J. Phys. D: Appl. Phys.*, **35**:2935, 2002.

[102] T. N. Hansen, J. Schou, and J. G. Lunney. *App. Surf. Sci.*, **138-139**:184, 1999.

[103] S. Amoruso, B. Toftmann, and J. Schou. *Phys. Rev. E*, **69**:056403–1, 2004.

[104] R. F. Wood, J. N. Leboeuf, D. B. Geohegan, A. A. Puretzky, and K. R. Chen. *Phys. Rev. B*, **58**:1533, 1998.

[105] S. S. Harilal, B. O' Shay, and M. S. Tillack. Prompt electron emission during nanosecond laser ablation of tin. In *Proceedings of the 8th International Conference on Laser Ablation.* Institute of Physics, 2006. To be published.

[106] S. S. Harilal, B. O'Shay, Y. Tao, and M. S. Tillack. *J. Appl. Phys.*, **99**:in press, 2006.

[107] S. Schwarz, 2005. Private communication.

[108] P. Dugourd, R. R. Hudgins, D. E. Clemmer, and M. F. Jarrold. *Rev. Sci. Instrum.*, **68**:1122, 1997.

[109] C. J. H. Schutte. *Chem. Phys. Lett.*, **353**:389, 2002.

[110] G. Bollen, D. J. Morrissey, and S. Schwarz. *Nucl. Instr. and Meth. A*, **550**:27, 2005.

[111] D.R. Lide, editor. *Handbook of Chemistry and Physics, 83rd Edition.* CRC Press, New York, 2002.

[112] HTW Hochtemperatur-Werkstoffe GmbH, 2000. Sigradur Data Sheet.

[113] E. T. Arakawa, M. W. Williams, and T. Inagaki. *J. Appl. Phys.*, **48**:3176, 1977.

[114] W. N. Reynolds. *Physical Properties of Graphite.* Elsevier Publishing Co. LTD., New York, 1968.

[115] R. F. Boivin, J. L. Kline, and E. E. Scime. *Physics of Plasmas*, **8**:5303, 2001.

[116] D. E. Evans. *Plasma Physics*, page 145. (The Institute of Physics), 1974. edited by B. E. Keen.

[117] Y. Andrew and M. G. O'Mullane. *Plasma Physics and Controlled Fusion*, **42**:301, 2000.

[118] P. McCarthy, R. Armstrong, and C. O'Neill. The use of multiple helium line ratios as a plasma diagnostic tool. *APS Meeting Abstracts*, 2004.

[119] J. Reader, C.H. Corliss, W. L. Wiese, and G.A. Martin. *Wavelengths and Transition Probabilities for Atoms and Atomic Ions.* U.S. Government Printing Office, Washington, D.C., 1980.

[120] A. R. Striganov and N.S. Sventitskii. *Tables of Spectral Lines of Neutral and Ionized Atoms.* IFI/ Plenum, New York, 1968.

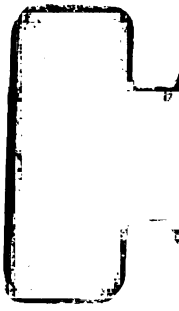

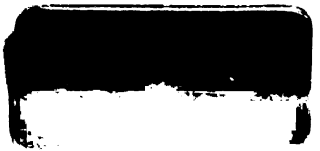

MICHIGAN STATE UNIVERSITY LIBRARIES
3 1293 02845 3276